seit 1558

FRIEDRICH-SCHLLER-UNIVERSITÄT JENA
Physikalisch-Astronomische Fakultät

Experimental Mid-Infrared Spectroscopic Extinction Measurements of Agglomerate Dust Grains in Aerosol

Dissertation
zur Erlangung des akademischen Grades
doctor rerum naturalium (Dr. rer. nat.)

vorgelegt dem Rat der Physikalischen-Astronomischen Fakultät
der Friedrich-Schiller-Universität Jena

von Master of Science Akemi Tamanai

geboren am 26.01.1968 in Hitachi, Japan

Gutachter

1. Prof. Dr. Ralph Neuhäuser
2. Prof. Dr. Jürgen Blum
3. Prof. Dr. Chiyoe Koike

Tag der letzten Rigorosumspruefung: 20. April 2007

Tag der oeffentlichen Verteidigung: 08. Mai 2007

Zusammenfassung

Staub spielt eine wichtige Rolle nicht nur bei der Temperaturbilanz astrophysikalischer Systeme wie protoplanetare Akkretionsscheiben, Molekülwolken, dem interstellaren Medium und den Atmosphären von Sternen und Planeten, sondern auch bei astrophysikalischen Prozessen wie der Bildung von Sternen und Planeten. Unterschiede in Größe, Zusammensetzung und Kristallstruktur der Staubteilchen lassen Rückschlüsse ziehen auf dynamische Prozesse (z.B. in Akkretionsscheiben) und spielen eine Schlüsselrolle für das Verständnis insbesondere der Frühphasen der Bildung (erdähnlicher) Planeten in der Umgebung junger Sterne. Die wichtigste Methode, um Staubpopulationen in verschiedenen Objekten (heutzutage sogar in verschiedenen Bereichen ein und desselben Objektes) zu untersuchen, ist Infrarotspektroskopie. Eine zentrale Rolle spielt dabei die 10 μm Si-O Streckschwingungs-Bande des Silikatstaubs, weil Silikat die Hauptkomponente des Staubes im Weltraum ist. Diese Bande kann vom Erdboden aus beobachtet werden. Staubteilchen im interstellaren Medium bestehen hauptsächlich aus amorphem Silikatstaub, während das Vorkommen von kristallinen Silikaten aus Beobachtungen im mittleren Infrarot bei zirkumstellaren Scheiben um junge Herbig Ae/Be Sterne (z.B. Malfait et al 1998; Meeus et al 2001), bei entwickelten Sternen (Molster et al. 2002), bei TTauri Sternen (TTSs; Meeus et al. 2003, Honda et al. 2003) und bei den Wega-ähnlichen Sternen HD 145263 und β Pic (z.B. Honda et al. 2004; Okamoto et al. 2004) bekannt ist. Die Analyse der infraroten Emissionsbanden - insbesondere des Bandenprofils bei 10 μm - erlaubt, Rückschlüsse zu ziehen über Staubwachstum und Kristallisation, die in den Frühphasen junger zirkumstellarer Scheiben bei der Entwicklung zu Planetensystemen auftreten. Dennoch ist die Analyse beobachteter Infrarotspektren sehr komplex, da nicht nur die mineralogischen Eigenschaften wie Kristallstruktur und chemische Zusammensetzung die Form und Intensität des einzelnen spektralen Merkmals bestimmen, sondern auch Größe, Form und die Agglomeration der Teilchen einen Einfluss ausüben. Daher sind umfangreiche Laboranalysen derartiger Einflüsse notwendig, um die Spektren interpretieren zu können. Staub mit hoher Kondensationstemperatur kann als Kondensationskeim für Partikel mit niedrigerer Kondensationstemperatur - wie Silikate - während der weiteren Abkühlung aufgrund von Ausdehnung dienen. Daher müssen Staubteilchen in sauerstoffreichen AGB-Sternen, die die Hauptquelle von kosmischem Staub sind, Spezies mit hoher Kondensationstemperatur einschließen. Tatsächlich zeigen AGB-Sterne sehr starke Emissionslinien bei 13 und 19μm, die von Korund, Spinell und Rutil stammen. Um das Verständnis vom Vorhandensein einer ersten Spezies zu einer ganzen Kondensationssequenz von Staubteilchen zu erweitern, ist es notwendig, auch Arten mit hoher Kondensationstemperatur zu berücksichtigen. Desweiteren ist die Bildung von Silikaten nicht vollständig verstanden - obwohl sowohl kristalline als auch amorphe Silikate in vielen astrophysikalischen Objekten entdeckt worden sind. Daher ist die Entwicklung von Spezies mit hoher Kondensationstemperatur wichtig zur Untersuchung der Bildung von Silikatstaubteilchen. Heutzutage sind die Bandenprofile, die zum Vergleich mit optischen Spektren benutzt werden, meist aus Modellrechnungen entnommen, wobei meist einfache Modelle - wie sphärische oder ellipsoidale Formen der Staubteilchen - zugrunde gelegt werden. Derartige Rechnungen sind ungenau, weil die wirklichen Formen der Staubteilchen irregulär sind. Zur Zeit sind Labormessungen an realen Staubteilchenzusammensetzungen nicht in der Lage, exakte Bandenprofile für einen direkten Vergleich zu liefern, weil die Proben von einem Medium (KBr) umgeben sind, welches Einfluss nimmt auf die elektromagnetische Polarisation (Fabian et al. 2001).

Ich habe im Rahmen dieser Arbeit eine neue Methode entwickelt, mit der Extinktionsspektren ohne den elektromagnetischen Einfluss umgebender Medien gemessen werden können. Mit Hilfe der Aerosoltechnik (Hinds 1999) habe ich Extinktionsspektren von amorphen wie kristallinen Silikaten, Quarz und Spezies mit hoher Kondensationstemperatur im mittleren Infrarot aufgenommen, die direkt mit beobachteten Spektren verglichen werden können. Ich untersuchte die Unterschiede zu den mit der KBr-Methode aufgenommen Daten, indem ich die Lage der Maxima der Bandenprofile bestimmte und verglich. Desweiteren habe ich die Staubkörner elektronenmikroskopisch untersucht, um morphologische Einflüsse (Größe, Form, Agglomeration) auf das gemessene Profil zu untersuchen.

Contents

List of Tables

List of Figures

Chapter 1

Introduction

Dust grains are not only crucial players for controlling the thermal balance in astrophysical environments such as protoplanetary accretion disks, molecular clouds, the interstellar medium, and atmospheres of stars and planets, but also in astrophysical processes such as star and planet formation. Changes in size, composition, and crystallinity of the dust grains indicate dynamical processes (e.g. in accretion disks) and hold a key to understanding specifically the early formation of terrestrial (Earth-like) planets in the environments of young stars. The most important technique, which makes it possible to obtain information about the dust populations in different objects (and nowadays even at different regions within one object), is infrared spectroscopy. One of the most important roles is played by the 10 μm Si-O stretching band of silicate dust because silicates are the major dust component in most dusty media in space, and this band can be observed from the ground.

In fact, solid particles in the interstellar medium consist mainly of amorphous silicate dust grains (see review by Whittet 1992), whereas the presence of crystalline silicates has been confirmed via mid-infrared observations in circumstellar disks around the relatively bright young Herbig Ae/Be (HAEBE) stars (e.g., Malfait et al. 1998; Meeus et al. 2001), for evolved stars (Molster et al. 2002), the T Tauri stars (TTSs; Meeus et al. 2003), the TTS Hen 3-600 (Honda et al. 2003), and the Vega-type stars HD 145263 and β-Pic (e.g., Honda et al. 2004; Okamoto et al. 2004). Analysis of the infrared emission bands and especially the 10 μm band profile of such silicate grains has allowed one to find indications of grain growth and crystallization that trace the early evolution of young circumstellar disks toward planetary systems (van Boekel et al. 2005). However, the analysis of observational infrared spectra is very complex for an accurate interpretation, since not only mineralogical properties such as crystallinity and chemical composition determine the shape and intensity of the distinctive spectral features, but also size, shape, and agglomeration of the grains exert an influence. Thus, exhaustive laboratory studies of these influences on the silicate dust bands are essential for an appropriate interpretation of the observed spectra.

High condensation temperature species can serve as seeds for lower condensation temperature ones such as silicates during further cooling due to expansion (Dorschner, private communication). Thus, dust grains in oxygen-rich asymptotic giant branch (AGB) stars, which are main dust production sources, must be composed of high condensation temperature species. In fact, oxygen-rich AGB stars show very strong 13 and 19 μm emission features which are conceived of high condensation temperature species such as Al_2O_3 (corundum), $MgAl_2O_4$ (spinel), and TiO_2 (rutile). Moreover, high temperature condensates are important because they contribute significant opacity when no other grains are present, even though they are not as abundant as the silicate or iron grains. If they are not included, the opacity may be as much as two orders of magnitude too low. Once the more abundant grains begin to condense, these low abundance grains lose their significance. But when they are the only grains present, they can be quite important. Early calculations of grain opacity did not include these species, so it was quite surprising to see the changes when they were included. They are significant only over a narrow range of temperatures, but it is an important transition region between the molecular regime to the dust regime (Alexander, private communication). In order to deepen the understanding from a first condensed species out of gas to a whole condensation sequence of dust grains, it is necessary to take the investigation of high condensation temperature species into account. In addition, although both crystalline and amorphous silicates have been detected in many astrophysical environments, the formation of silicates is not perfectly understood. The evolution of high condensation temperature species ought to hold a key to clarify the formation of silicate dust grains as well.

Currently, band profiles that are used for comparison with observed spectra are mostly calculated, assuming simple geometrical models such as spherical or ellipsoidal grain shapes. Predictions based on these calculations are uncertain because in reality the grain shape might be irregular. So far, laboratory measurements on real particle ensembles have not been able to provide exact band profiles for a direct comparison due to the use of an embedding medium (KBr) in the sample preparation, which changes the band profile substantially by the influence of its electromagnetic polarization (Fabian et al. 2001). I adopt a new method for laboratory measurements of extinction spectra avoiding the influence of electromagnetic interaction with solid embedding media. Applying the aerosol technique (Hinds 1999), I obtain extinction spectra in the mid-infrared region of both amorphous and crystalline silicates, silica, and the high condensation temperature species which are directly comparable to observed spectra. I investigate the differences to KBr-measured band profiles by deriving peak positions from the band profiles measured with both methods. Furthermore, I use electron-microscopic investigation of the grains to associate morphological (size, shape, agglomeration) influences on the measured profile.

Experimentally measured extinction spectra of free-flying particles relevant to astrophysical materials in the infrared region with attention to the morphological influences are dealt with in this thesis. The next chapter will describe the characteristics of astrophysical dust grains including a discussion of the interaction of light with these dust grains. For this purpose, the four theoretical approaches (Mie, Rayleigh-Gans, continuous distribution of ellipsoids (CDE), and discrete dipole approximation (DDA)) are addressed together with the explanation of optical constants requisite for theoretical calculations since the optical properties of dust grains can be described by frequency-dependent optical constants. In chapter 3, I summarize the fundamental chemical structure and behavior of silicates (olivine and pyroxene), silica, spinel, corundum, and rutile which are directly responsible for the band profiles. In chapter 4, I present a crucial difference between the aerosol and KBr pellet techniques including a discussion of advantages and disadvantages of them. The experimental set up of the devices are detailed with a part by a part description. Moreover, all the samples, which are actually used in both the aerosol and KBr pellet measurements, are listed along with respective transmission electron microscope (TEM) images and the explanations of the sample preparation methods. In chapter 5, I demonstrate the morphological effects through both the aerosol and KBr pellet technique experiments. Seven grain species with 18 different dust samples are examined. The measured profiles are compared with calculations for some cluster shapes applying the different theoretical approaches. The observed emission spectra of various astronomical objects such as a comet, HAEBE, T Tauri, Vega-type, and AGB stars are analyzed with the experimentally measured spectra in chapter 6. Finally, conclusion and future perspectives of dust investigations are discussed in chapter 7.

Chapter 2

An Essential Role of Astrophysical Dust Grains

2.1 What is the main source of dust grains in the universe?

The evolutionary history of stars can be expressed in two crucial relationships which are luminosity with effective temperature (or spectral types) and luminosity with mass in Hertzsprung-Russell diagram (HR diagram) as shown in Fig. 2.1. For instance, our Sun is now located on the main sequence where approximately 90 % of stars lie as well (Note: about 10 % of the stars are white dwarfs). The age of the Sun is considered to be about 5×10^9 years from geologists' view points. After the Sun has remained on the main sequence for 10 billion years, it will evolve to a red giant that is much more luminous and cool in temperature (Morrison & Wolff 1990; Smith 1995). It has been thought that dust formation mainly takes place in the outflow of red giants, which less than 1 % of the stars (Gehrz 1989).

The main energy production of stars is nuclear fusion in the central stellar core to burn hydrogen into helium, helium into carbon, carbon into heavier elements. Hydrogen fusion occurs in the center of stars while they are on the main sequence. In other words, nearly all stars continuously convert hydrogen to helium for about 90 % of their total lifetimes. When all the hydrogen in the core has been exhausted, hydrogen fusion must be ended. Although the hottest place is still the stellar center, heat energy leaks out consecutively. Then, the temperature would decrease if the core does not collapse. As a result of that, the gas pressure cannot sustain the weight of the core layer that is situated the exterior core as shown in Fig. 2.2. Gravity holds a dominant position in this circumstance instead of the pressure for a while as all of the stellar evolution is controlled by the relation between pressure and gravity. When the core layer upsets the balance, the core will be shrunk by force which induces a thermal rising. Due to both the heat via the shrinkage of the core and the leakage from the core, the temperature of its surrounding region rises. In consequence, the temperature becomes high enough to be able to start hydrogen fusion in a shell around the core. The energy released from the helium core shrinkage is absorbed by the surrounding materials which causes the central core region to heat up and gives rise to the expansion of a star. Since the expansion results in cooling down the surface layer, the star becomes red. Simultaneously, the gravitational collapse heats up the hydrogen which encloses the shrinking core; therefore, hydrogen fusion takes place there energetically and maintains higher temperatures to increase in total luminosity. Stars with high luminosity and cool surface temperatures are so-called *red giants* (Morrison & Wolff 1990).

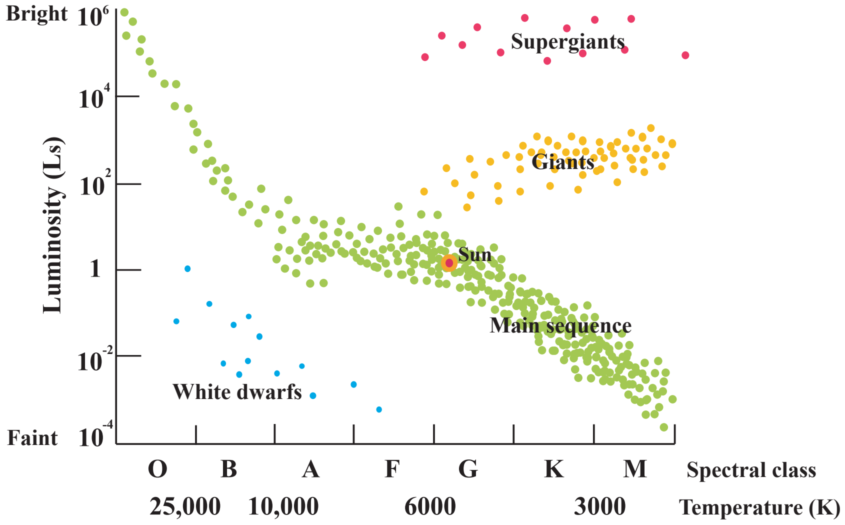

Figure 2.1: Schematic H-R diagram from Smith (1995) and Morrison & Wolff (1990). Our Sun is on the Main sequence.

Approximately 10 % of the star's hydrogen must be converted to helium before the star leaves the main sequence (Note: the position of a star along the main sequence is determined by mass). This conversion rapidly occurs in stars with higher luminosity and more mass. Since the total rate of energy generation in a star must be equal to its luminosity, the hydrogen of the core is used up rapidly in very luminous stars (see more details in Morrison & Wolff 1990).

The most important condition for dust formation is low temperature combined with high density in order to produce condensates stable against evaporation. Regions with low temperature usually occur only at a significant distance above the photosphere with densities that are orders of magnitude lower than in the photosphere of stars (Habing and Olofsson 2004).

Since red giants and supergiants (higher luminosity than the red giants) belong to the asymptotic giant branch (AGB), they are also called the AGB stars that can be divided into 3 types depending on the carbon/oxygen (C/O) ratio in their atmosphere: the oxygen-rich M-type stars (C/O <1), the carbon-rich C-type stars (C/O >1), the S-type stars (C/O ≈1). Only the oxygen-rich stars are considered in this study.

Particularly, these AGB stars undergo almost 90 % of total stellar mass loss. As a result, the largest amount of dust grains are contributed into the interstellar medium (ISM). During the last stages of stellar evolution, the AGB stars are surrounded by an optically thick dust shell in which small solid particles are condensed out of the cooling gas phase as above. Also, supernovae and nova explosions expell dust grains which are produced in outflows from them (Sedlmayr 1994; Gail & Sedlmayr 1999).

2.2 Dust grain formation

It has been suggested that simple metal oxide condensation species (e.g. MgO, SiO, FeO etc...) play an important role in grain formation for oxygen-rich stars. A reduction in monoatomic species is seen as both the gas temperature and the mass density of the species decrease due to a recombination of the plasma. As the distance from the envelope of a star increases, much more complex molecules are formed. When the temperature is below 1500 K, some certain atoms and molecules react on the surfaces of dust grains because they are never able to react in the gas (Gould & Salpeter 1963). In initial condensation process, appropriate molecules are

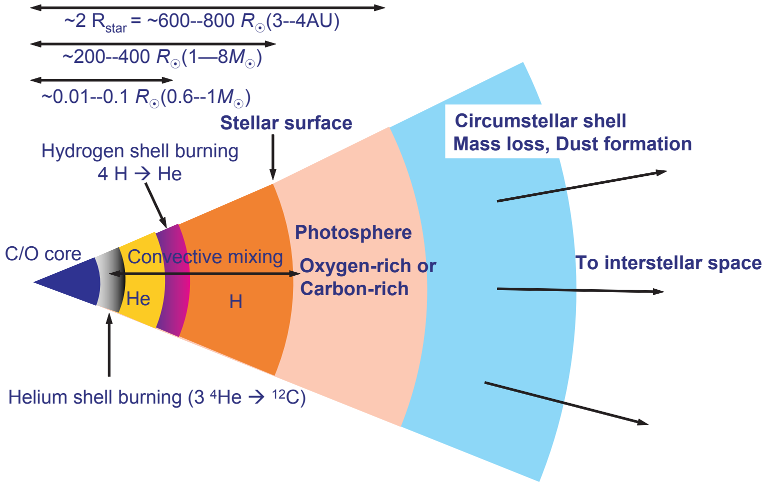

Figure 2.2: A cross section diagram of a AGB star interior from Ohnaka (2006).

combined to form small clusters as nucleation seeds which may have further chemical reactions (e.g. adding proper molecules) to increase in size to micron. At the same time, a chain of the chemical reactions is the cause of the formation of complicated chemical compounds.

The critical cluster is the first thermodynamically stable element to be formed in a supersaturated condition via the molecule-grain transition (Feder et al. 1966). If all clusters are smaller than N_* ($N<N_*$)[1], they are thermally unstable and have a tendency to evaporate. Conversely, if all clusters are larger than N_* ($N>N_*$), they are thermally stable and will grow. The critical cluster growth is a thermodynamical process with taking growth timescale into account. In addition, a variety of dust grain structures is influenced by the local chemistry and the thermodynamical conditions (Sedlmayr 1994).

2.3 Potential dust grain structures

Fig. 2.3 represents a diagram for the different sorts of possible grain structures which may form under various astrophysical conditions.

2.3.1 Homogeneous grains

The formation of crystalline structures (e.g. monocrystalline, polycrystalline, amorphous) has been determined to occur in the homogeneous grain condensation process with different timescales (see more details of the crystallization in Chap. 3).

2.3.2 Heterogeneous grains: Dirty grains

Dominik et al. (1993) discussed dirty particles which are formed with a non-stoichiometric composition under conditions in which the supersaturation ratio (S) of various atomic and

---

[1] N is the number of monomer particle; N_* is the critical cluster size which maximizes value of the enthalpy of formation ΔH_f° for a given temperature and density. The enthalpy of formation (ΔH_f°) denotes the internal energy change via releasing and absorbing energy associated with the formation of a compound from its constituent elements (Bejan et al. 1996). The subscripted "f" signifies formation and "∘" means standard conditions.

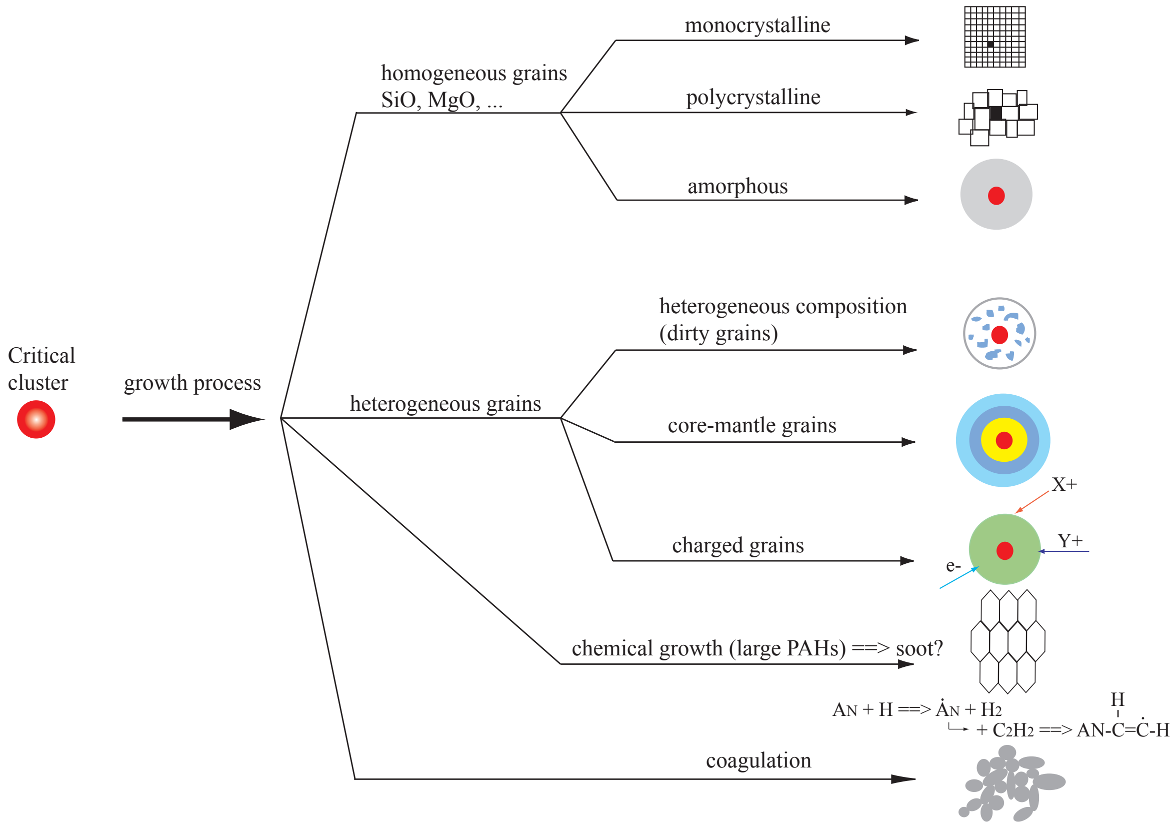

Figure 2.3: A diagram of potential grain structures via the grain growth process based on Sedlmayr (1994).

molecular condensation species are larger than unity, and then these species are sedimented on the surface of a critical cluster to form the heterogeneous ones. Although the critical cluster formation needs to have high supersaturation ratio (S≫1), grain growth will proceed if the supersaturation ratio is greater than unity (S>1) with respect to each species (Jeong et al. 1999).

2.3.3 Heterogeneous grains: Core-mantle grains

Another possible heterogeneous grain structure is the so-called ”core-mantle” grains. As the distance from the surface of a star increases, the chemical conditions vary because the local temperature and density change as well. Consequently, different proportions and varieties of condensed dust grains form in different regions. When a condensed dust grain in a stellar wind moves outward, the grain is surrounded by other sorts of chemically dominant species; as a result, an onion-shell type of dust grain structure is formed. In fact, this onion-shell structure has been seen in the carbonaceous chondrites (Greshake et al. 1996; 1998). Furthermore, it is conceivable that a typical interstellar grain is composed of a small solid grain (e.g. silicate) core surrounded by an icy mantle (e.g. H_2O, CH_4, NH_3) as shown in Fig. 2.4(a). The grains in the interstellar clouds (e.g. molecular clouds) continue to grow by accreting additional molecules for the outermost (Morrison & Wolff 1990).

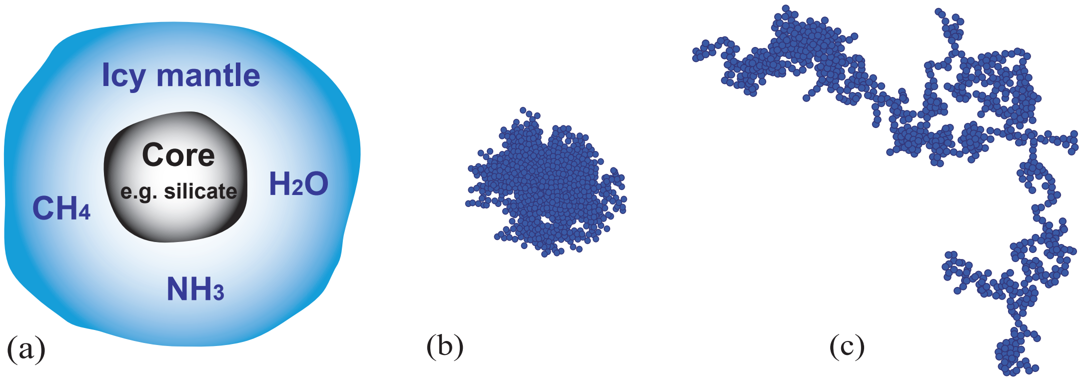

Figure 2.4: (a) Cross-sectional diagram of a core-mantle grain in interstellar clouds from Morrison & Wolf (1990). Illustrations for the two types of aggregates from Kozasa et al. (1992): (b) The BPCA (close-packed structure) with N=1024 particles (c) The BCCA (fluffy structure) with N=1024 particles.

2.3.4 Heterogeneous grains: Ionized grains

If there ionizing UV-photons are present, some of the molecules and atoms will be ionized to generate free electrons. The affected dust grains will become negatively charged which increases the constructive collision rate for grain growth.

The universe consists of 99 % plasma (e.g. Graps 2006) and dust grains in astrophysical environments are actually charged by collisions with electrons and ions and by photoelectric emissions via interaction of incident UV radiation in general. The charging process of UV radiation and collisions with charged dust particles control the sign and the magnitude of the net particle charge (Abbas et al. 2004). Particularly, the collision process of the charged particles is closely related with grain coagulation which accelerates due to the Coulomb attraction between the oppositely charged particles (a detailed explanation of the coagulation process will be in Sec. 2.3.5). Horanyi et al. (1990) stated that the coagulating particles gather electrostatic charges in plasma environment, and Simpson et al. (1979) demonstrated a reduction of the grain coagulation rate via the electrically same sign of nonzero charged grains. Hence, the charge of a dust grain strongly influences the physical properties of dusty plasmas.

2.3.5 Heterogeneous grains: Coagulation of grains

Whereas grain coagulation processes do not play a crucial role in stellar winds because the timescales are too short (Dominik et al. 1989), these processes are the most important processing during the early stages of planet formation. Dust coagulation means that dust particles collide and adhere mutually to form larger aggregates.

This fundamental process of planet formation starts with collision of micron-sized dust particles through mainly the action of the van der Waals forces to adhere the particles to each other (Weidenschilling & Cuzzi 1993). In consequence, the micron-sized particles grow to form planetesimals with a diameter of a few kilometers to a few tens of kilometers. There is observational evidence of some dust grain coagulation in young circumstellar disks (e.g. Throop et al. 2001; van Boekel et al. 2003).

Fig. 2.4(b) and (c) show typical models of dust aggregates (Kozasa et al. 1992). The structure of the aggregate in Fig. 2.4(b) is called "the Ballistic Particle-Cluster Aggregates

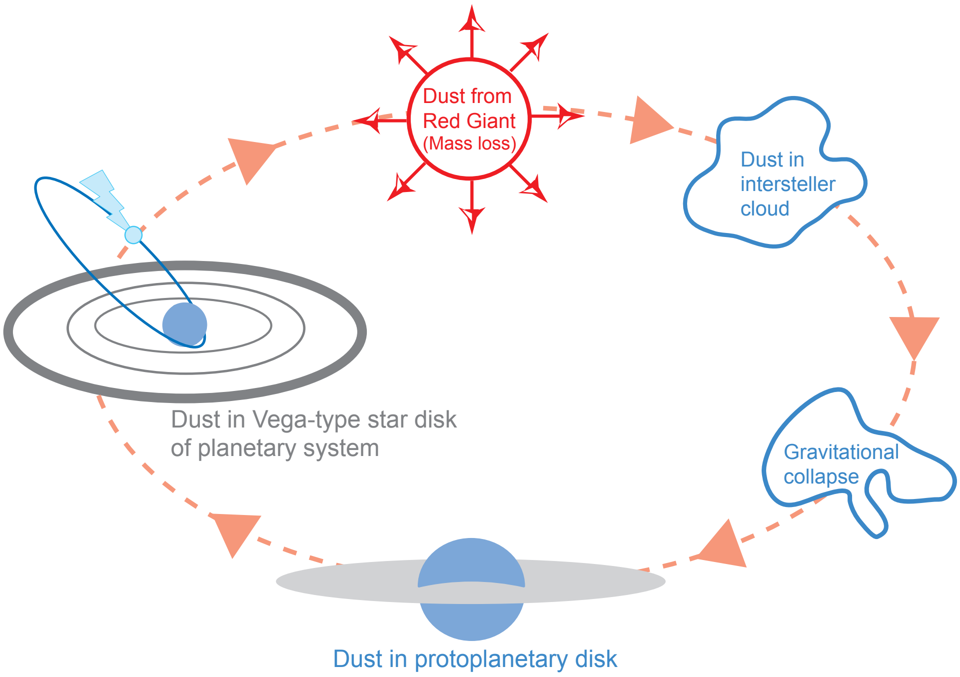

Figure 2.5: A diagram of dust grain cycle based on drawing from Dominik (2000).

(BPCA)," which grow by sticking of one particle by one particle to form compact (close-packed) aggregates. Conversely, "the Ballistic Cluster-Cluster Aggregates (BCCA)" in Fig. 2.4(c) are formed by attaching dust aggregate with the same mass at a time. Thus, the BCCA is a porous type of structure which contains significant proportion of vacuum along with solid dust particles. These fluffy or porous aggregates can produce higher extinction per unit mass than the compact aggregates (Iati et al. 2001) which signifies that fluffy grains are able to increase dust opacities especially at long wavelengths (Ossenkopf 1991). It is important for the understanding of the far-infrared and the sub-mm emissivity (λ>100μm) of very cold dust grains existing in the ISM, especially in molecular cloud cores.

The optical properties of dust particles with irregular structures like porous aggregates have simulated by the use of different theoretical approaches (e.g. Purcell and Pennypacker 1973; Mishchenko 1990; Min et al. 2003) (see more details in Sec. 2.7). Since the dust particles which exist in astrophysical environments, are more likely irregular structures rather than spherical shapes and inhomogeneous, such particles influence the physical and chemical properties (see Sedlmayr 1994). Accurate theoretical approaches are needed to determine their properties of grains (This section is based on Sedlmayr 1994).

2.4 Evolution cycle of dust grains

After the dust grains are formed in the outflow of the AGB stars, they will be ejected into the ISM (The mechanisms of dust grain formation in AGB stars are discussed in Sec. 2.1.). Simple metal oxides are formed in M-stars with low mass loss rates ($\dot{M}$<10^{-7} $M_\odot$/yr) as the main dust sources (Posch et al. 2002). Moreover, although the process of silicate crystallization and the formation of silicates from the simple metal oxides in the winds of AGB stars is not well understood, crystalline silicates in the outflows of AGB stars with high mass loss rate have been detected by the Infrared Space Observatory (ISO) (e.g. Waters et al. 1996; Molster et al. 2002). In most cases, the crystalline silicates are not dominant, but account for only 10 to 15 % of the dust compared with the amorphous silicates (Molster & Waters 2003).

After the largest amount of dust grains is expelled into the ISM, they undergo destruction and/or modification. The size of the dust grains is approximately 0.01 to 0.1 μm in the ISM. Dust grains expose themselves to danger due to evaporation if they accrete icy mantles. Unless sputtering occurs, refractory materials (e.g. silicates, graphite, SiC, hydrocarbon) are exceedingly durable. When an incident atom moves with an adequate speed ($V>50$ km/h), it moves one of the atoms in the lattice out of place. This process is called sputtering and gives rise to the destruction of the grains. A supernova with an energy 5×10^{43} J may be able to achieve the shock velocity to destroy all dust grains in a mass of gas of about 300 $M_\odot$ (e.g. masses of dense core regions in molecular clouds are about 100 to 1000 $M_\odot$ (Illingworth 1994)) (Dyson & Williams 1997).

The most important role of dust grains in the ISM is to retain the thermal balance and reduce the UV radiation that leads to molecular dissociations to support the formation of the most abundant interstellar molecule, H_2 (Mathis 1990). The ISM is fundamentally composed of two regions. HI regions, which include diffuse clouds, contain neutral hydrogen. These regions are surrounded by tenuous hot hydrogen gas (1000-10000 K) whereas the temperature of the regions themselves is approximately 70 K. HII regions are the other component of the ISM, which are basically comprised of ionized hydrogen (Illingworth 1994). Molecular clouds are primarily composed of molecular hydrogen (H_2). In giant molecular clouds (GMCs), particle densities are the order of 10 to 100 cm^{-3} (Spitzer 1982) and temperatures are approximately 80 K. The center of GMCs are exceedingly dense and lower in temperature about 10K. These dense cores contain HII regions. It has been considered that most star formation takes place in H_2 molecule-rich GMCs which are the most massive objects in the Galaxy (Morrison & Wolff 1990; Cowley 1995). Both molecular and diffuse clouds contain dust grains.

Another point in the ISM is that though crystalline silicates are formed in the outflow of the AGB stars and ejected into the ISM, only amorphous silicates have been identified there so far. It is difficult to consider that there is an active annealing process to form crystalline silicates since the temperature of the dust grains in the ISM is about 10 to 100 K which is too far from the annealing temperature for crystallization of silicates. Molster & Waters (2003) suggested that crystalline silicates may be completely destroyed in the ISM or may be amorphized in the ISM.

In star and planet formation scenarios, again crystalline silicates have been detected via mid-infrared observations of circumstellar disks around relatively bright young Herbig Ae/Be (HAEBE) stars (e.g. Malfait et al. 1998; Meeus et al. 2001), the T-Tauri stars (TTSs; Meeus et al. 2003), and the TTS Hen 3-600 (Honda et al. 2003), which is an indication of either active annealing processes to transform the amorphous phase to the crystalline one or of gas-phase condensation (Bradley et al. 1983). Both amorphous and crystalline micron-sized dust grains take part in planet formation. Especially, they become important players in terrestrial (Earth-like) planet formation in the environments of young stars due to their varying size, composition, and crystallinity.

After these small grains are consumed by planet formation, new dust grains will be mainly produced from AGB stars and supernovae again. This repeated process is in a cycle as shown in Fig. 2.5 (Dominik 2000) in which dust grains undergo continuous transformations such as crystalline to amorphous phase, size due to the coagulation or destruction, and shape due to the collisions.

2.5 Relation between light and matter: Basic concepts of extinction, absorption, and scattering

Dust grains scatter and absorb incident radiation. Thus, the grains do not only propagate the radiation in different directions, but also they transform it into thermal energy. Radiation interacts with matter via a number of mechanisms, including by radiative decay of collisionally or radiatively excited bound states of atoms and molecules, radiative recombination following a collisional ionization, and free-free emission in which a free electron in the neighborhood of an ion or an atom looses kinetic energy.

If the radiation interacts with an atom, the electron of the atom is excited and promoted from a low-energy level to a higher level (or levels) only when it absorbs a photon with exactly the right energy. Since the energy of a photon depends on its wavelength, only photons of certain wavelengths can be absorbed by an atom, which produces spectral absorption lines. However, almost instantly (within nanoseconds) the electron drops down to its original level because the excited atom is unstable and emits a new photon with the same wavelength as the one it absorbed that corresponds to the energy difference between the levels at the first and at the end of that movement[2]. Since atoms absorb the radiation, in consequence, they become excited and immediately de-excite themselves and re-emit the radiation as emission lines. As a result of the interaction with other particles, nuclei, atoms, or molecules, the atoms re-emit photons in random directions, which is called *scattering* process (Seeds 1995).

On the other hand, if the excited atom collides with another atom before re-emitting the photon, it may be a super-elastic collision in which the transformational energy of the actively moving atom is increased. When the electron drops from a higher energy level to lower energy level, it must give up the excess energy instead of emitting a photon and is converted into kinetic energy (heat energy) of the colliding atoms. At that time, the photon is destroyed in the process. This process is called *absorption* (Tatum 2006). Hence, the excess energy will be transformed into thermal energy if an atom is in a dense medium which mostly result in absorption lines. Conversely, emission lines are produced because an atom will re-emit a recently produced photon so as to release the excess energy if an atom is in a thin gas medium (at low density) where the atom is not able to go through many collisions. Respective atoms have their own distinctive electron orbits; therefore, there exists their own peculiar set of spectral lines which have been practically utilized to identify the characteristics of each atom.

Since solid materials are composed of aggregate with many atoms and molecules, the fundamental processes of the absorption and scattering have also occurred solid grains as mentioned above. Nevertheless, the characteristics of the solid materials have to be taken into consideration in regard to the absorption and scattering processes. Solids and liquids are optically dense, which is approximately 2-3 Å in the molecular separation, is much less than the wavelength of the incident light. Electric charges (electrons and protons) in the solid materials are induced oscillatory motion by the electric field of the incident wave when an electromagnetic radiation penetrates the material; therefore, absorption takes place over a range of frequencies, and excited atoms lose their energy by intermolecular collisions rather than emitting photons in dense solids. Once the incident radiation comes into the solid material, the incident wave will be entirely extinguished in the material. As soon as the incident wave reaches to the surface of the material, it is refracted with the propagation velocity c/n where c is the speed of light in vacuum and n is the refractive index (a real part; see more details in Sec. 2.7.1) due to

---

[2] The re-emitted photon will have the same energy only if the electron returns to the original state. If it makes a transition to one or more intermediate states, then the wavelength will be different and longer.

a change of medium. As a result, the secondary waves appear in the material. The refractive index n varies depending on the number of molecules per unit volume and the polarizability of a single molecule. Besides, the refractive index is a decisive factor of the scattering process. The optical properties of a dust grain are fully defined by frequency-dependent optical constants (see Sec. 2.7.1) (Bohren & Huffman 1983; Hecht 1987).

The attenuation of the incident electromagnetic radiation or *Extinction* is the summation of the absorption and the scattering (Extinction = Absorption + Scattering). Extinction, absorption, and scattering significantly depend on physical properties of dust grains; for example, the effects of conductivity, crystallinity, shape, chemical composition, and size (Bohren & Huffman 1983).

2.6 Absorption and emission lines in the IR region

Atomic absorption and emission lines frequently occur in the ultraviolet (UV) region, which has enough energy to induce electron transitions in the energy range from roughly 3.3 eV ($\simeq 0.38~\mu$m) to 140 eV ($\simeq 0.009~\mu$m). These energies have a crucial role in triggering many chemical reactions. Unlike the UV, the infrared (IR) radiation affects mostly molecules, whose vibrational and rotational frequencies lie in this range. The IR can be subdivided into mainly three regions: the near IR with the range from 0.78 μm to 2.5 μm, the mid IR from 2.5 μm to 50 μm, and the far IR from 50 μm to 1000 μm in wavelength. The vibrational spectra of the molecules are able to be detected in the near and mid IR region whereas the rotational spectra are predominantly detected in the far IR and microwave regions (Hecht, 1987).

For instance, diatomic molecules have an additional degree of freedom in comparison with an atom in order to transform the state of motion of their constituent atoms referring to their center of mass. Both vibrational and rotational motions take place simultaneously in the diatomic molecules and are quantized. Each vibrational state has a unique set of rotational levels. The molecules are able to absorb and emit energy because of the transition among these levels (Atkins 1994).

Incident electromagnetic radiation can stimulate the rotational frequencies for only polar molecules. Essentially, the radiation may be considered as an electromagnetic wave which consists of electric and magnetic fields orthogonal each other. When the radiation interacts with the molecules, the electric field of the incident wave exerts a torque on the electric dipole of the molecule, causing it to rotate around the direction of the electric field. In other words, only polar molecules can absorb a photon leading to a rotational transition. Though water molecules are a good example of a polar molecule which efficiently absorbs radiation and actively induces rotational transitions, non-polar molecules such as carbon, hydrogen, and methane do not possess permitted rotational transitions for the absorption of photons. The rotational energy levels for rigid molecules can be obtained by the Schrödinger equation (see more details in Anderson 1971). The spectrum from the rotational transitions usually lies in the far IR to the microwave regions (Hecht 1987).

The quantum energy of infrared photons is in the range between 0.001 eV ($\simeq 1240~\mu$m) and 1.7 eV ($\simeq 0.73~\mu$m) which fits the energy range of the quantum state separations of molecular vibrations. When the electromagnetic radiation interacts with the simple diatomic molecules and matches their vibrational frequency, the constituent atoms of the molecule can be excited by photons and start vibrating with one of three basic different modes: asymmetric stretching, bending, and symmetric stretching. The vibrational energy of the molecules are exposed in the vibrational levels that depend on the modes. In vibrational transitions, it is not necessary for the molecules to be polar. Even if the molecule is non-polar, it may result in an oscillating dipole which can interact with the electromagnetic field. Due to the IR absorption, the substances are heated up since the absorption process actively induces the molecular vibrational transition (Atkins 1994).

Many molecules undergo both vibrational and rotational resonances in the IR and become effective absorbers. Accordingly, the IR radiation is also called *heat* or *thermal* waves (Hecht 1987).

In solid materials, properties of solids (crystalline or amorphous) (Sec. 3.1 & 3.2), geometric structures in the crystalline state (Sec. 3.3), and their size have a close connection with absorption and emission lines. The absorption of crystalline materials is led to electronic transitions inside atoms and molecules at short wavelengths (UV region) whereas vibrations of the crystal lattice give rise to the absorption at long wavelengths (IR region; Sec. 2.7.1). Thus, the absorption line transitions strongly depend on the crystal structures.

2.7 Theoretical approaches

Laboratory measurements are compared with theoretical calculations which take into account particle shape and size. It has recently become possible to utilize particular methods for especially inhomogeneous structures and arbitrary shaped particles in order to calculate the extinction, absorption, and scattering by solid particles. First of all, the role of optical constants will be introduced so as to promote a better understanding of optical properties.

2.7.1 Optical constants

A solid particle obstructs the continuity of a light wave since the refractive index of the particle is different from that of the surrounding medium. The refractive index is the ratio of the index of one medium to that of another, and is an absolute value. When absorption is not significant, the refractive index can be expressed by a real number. Conversely, if absorption is significant, the refractive index of the material must be represented by a complex number. There are two sets of quantities that are often used to describe optical properties. They are the real and imaginary parts of the complex refractive index m

$$\mathrm{m} = \mathrm{n} + i\mathrm{k} \tag{2.1}$$

where n is the real part and k is the imaginary part. n and k are both non-negative. Whereas the real number n directly relates to refraction, the imaginary k relates to absorption. Moreover, the real part n determines the phase velocity v

$$v = \frac{\mathrm{c}}{\mathrm{n}} \tag{2.2}$$

where c is the speed of light. The imaginary part of the complex refractive index k determines the attenuation of the wave as it propagates through the medium; therefore, the imaginary part k is also called absorption index k of the material. Consequently, the refractive index is expressed by a real number if the imaginary part k is very small and can be ignored due to the insignificant absorption.

The complex refractive index m can be replaced by use of the complex dielectric function or relative permittivity

$$\varepsilon = \varepsilon^{'} + i\varepsilon^{''} \tag{2.3}$$

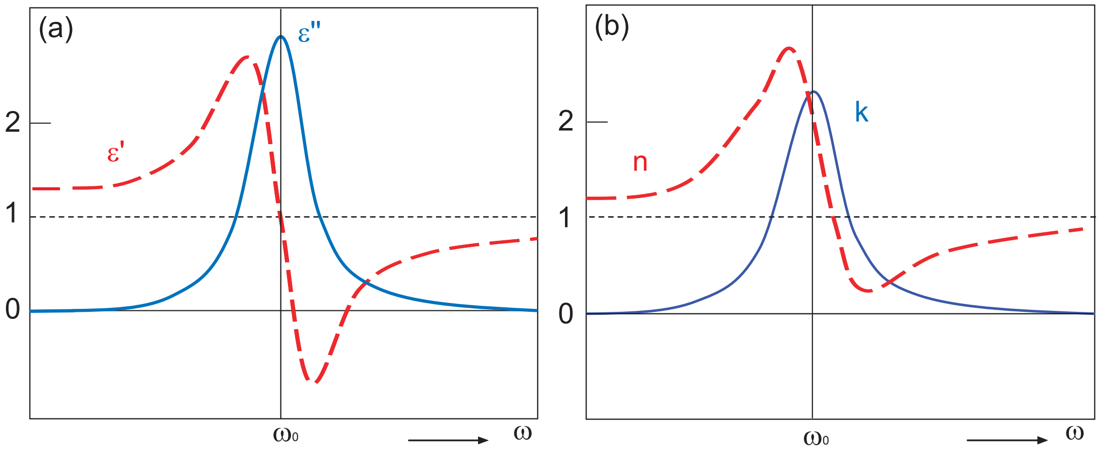

Figure 2.6: Schematic diagram of the Lorenz model with one-oscillator based on Bohren & Huffman (1983). (a) The dielectric function of $\varepsilon^{'}$ and $\varepsilon^{''}$. (b) The refractive index of n and k.

The relation between the two properties is

$$\varepsilon = \varepsilon^{'} + i\varepsilon^{''} = (\mathrm{n} + i\mathrm{k})^2 \tag{2.4}$$

$$\varepsilon^{'} = \mathrm{n}^2 - \mathrm{k}^2 \tag{2.5}$$

$$\varepsilon^{''} = 2\mathrm{nk} \tag{2.6}$$

The material is assumed to be non-magnetic (μ=μ_0). The pair of quantities (n, k) and ($\varepsilon^{'}$, $\varepsilon^{''}$) are referred to as the optical constants. As n and k are related to the phase velocity and attenuation of plane waves in matter, they are preferred to use in wave propagation. On the other hand, $\varepsilon^{'}$ and $\varepsilon^{''}$ are used in describing microscopic mechanisms (Bohren & Huffman 1983).

A determining factor of spectrum features is the close connection with surface modes of particles. Surface modes explain ”phenomena, which involve resonant propagation of electromagnetic waves and energy transport parallel to the surface” (Schubert 2004). Accordingly, the number and position of the peaks, intensity, and the bandwidth of the spectra are depending on shape, size, chemical properties, and dielectric function of particles (Bohren & Huffman 1983).

The absorption of crystalline materials at short wavelengths arises from electronic transitions within atoms and molecules. On the other hand, vibrations of the crystal lattice cause the absorption at long wavelengths. The lattice vibrations of crystals involve either acoustic (e.g. longitudinal or transverse (LA or TA)) phonons or optical (e.g. longitudinal or transverse (LO or TO)) phonons. (Note: a phonon is defined as a quantized mode of lattice vibration only in solid crystal.) The acoustic vibrations do not cause the polarization to vary and interaction with electromagnetic fields whereas the optical vibrations cause oscillatory displacements (van der Vorst et al. 2006). The absorption takes place when an electromagnetic wave (IR radiation) comes into a crystal lattice, and the TO phonon vibration will be induced (Saito et al. 2004).

Since the Lorentz model treats the electrons and ions of substances as simple harmonic oscillators, the dielectric function can be expressed as a function of frequency ω. Then, the dielectric function of simple harmonic oscillators is written as

$$\varepsilon = 1 + \chi = 1 + \frac{\omega_{\mathrm{p}}^2}{\omega_0^2 - \omega^2 - i\gamma\omega} \tag{2.7}$$

through the equation of the oscillator motion

$$m\ddot{\mathrm{x}} + D\dot{\mathrm{x}} + \mathrm{Kx} = \mathrm{eE}_{\mathrm{local}} \tag{2.8}$$

where χ is the electric susceptibility, ω_{p} is the plasma frequency (ω_{p}^2=$\Re\mathrm{e}^2/m\varepsilon_0$: $\Re$ is the number of oscillators per unit volume, e is the electron charge, m is the electron mass, and ε_0 is the vacuum permittivity), γ is a parameter which denotes the strength of anharmonic effects in producing damping of the electromagnetic excitation (γ=D/m; D is the damping constant), and ω_0 is a resonant frequency (ω_0=K/m; K is the spring constant), E_{local} is the local field at the position of a single oscillator. Fig. 2.6(a) shows the complex dielectric function ($\varepsilon^{'}$, $\varepsilon^{''}$) and the complex refractive index (n, k) is shown in Fig. 2.6(b) (Bohren & Huffman 1983). The absorption effectively occurs around ω_0. When ω<ω_0, the real part n of the refractive index gently increases. If the imaginary part k is much smaller than unity (k<<1), a substance becomes transparent. This is a normal dispersion region where the absorption does not take place effectively. Conversely, if ω>ω_0, the real part n becomes smaller than unity in a region of active absorption which is the so-called anomalous dispersion region (Saito et al. 2004). In anomalous dispersion range, the imaginary part $\varepsilon^{''}$ and k values are very high, and the real part $\varepsilon^{'}$ and n have a substantial difference at the peak positions as shown in Fig. 2.7(a). The maximum k is shifted to shorter wavelength with respect to the maximum $\varepsilon^{''}$ and the curve is asymmetric for a strong oscillator in general. The real part n becomes less than unity (n<1). In weak oscillator, on the other hand, the real part n is approximately constant and is always greater than unity (n>1) in Fig. 2.7(b). Then, there is no detectable maximum shift between k and $\varepsilon^{''}$. Unlike the case of strong oscillator, the resonance frequency of the oscillator can be determined by observation of the imaginary part k alone (Note: The resonance frequency ω_0=maximum of $\varepsilon^{''}$=the transverse optical mode (TO mode); see more details in Röseler 1990).

Temperature variation influence the index of refraction. Especially, transparency is improved by lowering temperature. Simultaneously, impurities and defects of solid materials produce an effect on the temperature and frequency dependence of the imaginary part of the refractive index in particular (see in Chap. 3 & Thomas 1991).

In the case of small spherical particles, the complex refractive index will be expressed as

$$\mathrm{m}^2 = -2 \tag{2.9}$$

Thus, if the spherical particle is in surrounding medium, the complex dielectric function becomes

$$\varepsilon = -2\varepsilon_{\mathrm{m}} \tag{2.10}$$

where ε_{m} is the dielectric function of the surrounding medium (assuming that it is nonabsorbing). The frequency condition at $\varepsilon^{'}$=-2ε_{m} and $\varepsilon^{''}$≈0 is called Fröhlich frequency ω_{F} which correlates with the normal mode (uniform polarization mode). The Fröhlich frequency is generally equivalent to the frequency at the maximum absorption (ω_{F}≈ω_0) only for small spherical grains (Rayleigh case). Moreover, the Fröhlich frequency shifts to longer wavelengths with an increase in particle size and with higher values of ε_{m}.

The dielectric function varies greatly depending on the wavelength region as shown in Fig. 2.8 (left panel). Debye relaxation influences occur in the microwave region whereas the electronic transitions cause the absorption spectra at the UV region, and the lattice vibration of the crystal induces the absorption in the IR. The numbers of resonances change with each vibration mode; therefore, the optical properties of a substance are reflected by a set of various resonances in Fig. 2.8 (right panel).

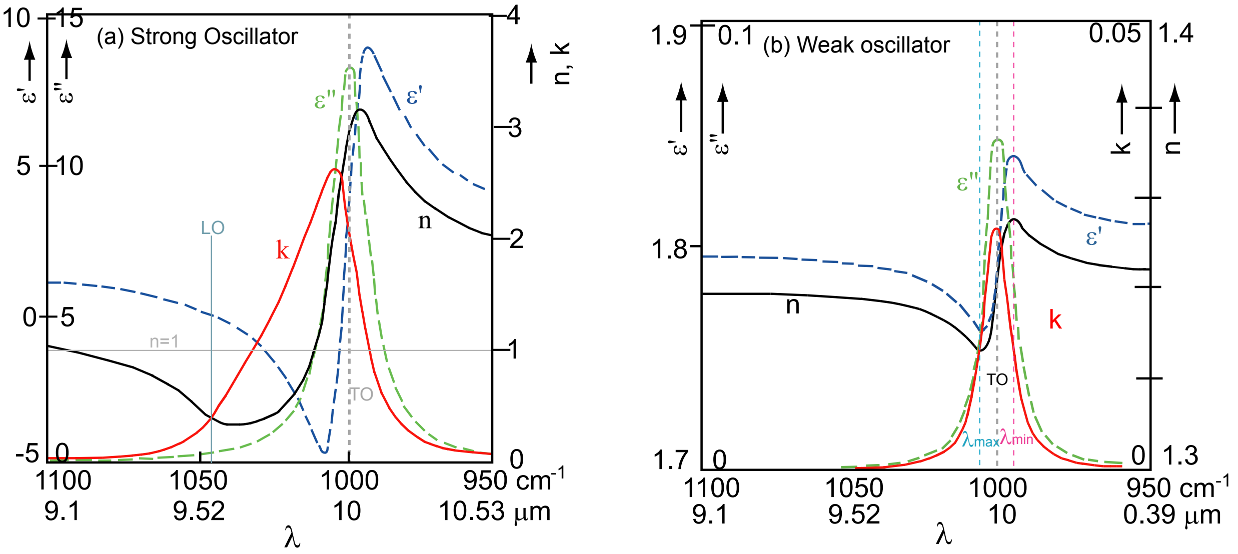

Figure 2.7: Schematic diagram of quartz glass optical constants based from Röseler (1990). (a) A case of strong oscillator (anomalous dispersion region), the gray dotted line denotes the resonance frequency (TO mode) and the blue line denotes the LO mode. (b) A case of weak oscillator, The gray doted lines denotes the TO mode, and the maximum (λ_{Max}) and minimum (λ_{Max}) peak positions for the real part of refractive index.

2.7.2 Mie and Rayleigh-Gans theories

The complex light scattering problem for uniform spheres was solved by Mie (1908) and Debye (1909). Mie theory is a complete solution for the interaction between a polarized plane wave and a dielectric sphere with a complex refractive index (Bohren & Huffman 1983). This is a wavelength dependent exact solution which does not have a specific criterion of the particle size to apply for the method; however, as the size of a particle increases (d>2 μm), accuracy of the calculation is gradually lost. On the one hand, Lord Rayleigh (1899) assumed that the particles were far smaller than the wavelength of light, and denser than the surrounding medium. Under these conditions, he proposed the Rayleigh-Gans theory which must satisfy the criterion that the electromagnetic field within the scatterers should be closely approximated by the undistributed incident field. The theory assumes only that the particles are spherical, isotropic, far smaller than the wavelength of an incident radiation, and denser than the surrounding medium. Then, the conditions for the Rayleigh-Gans theory are

$$|\mathrm{m}-1| \ll 1 \tag{2.11}$$

$$\mathrm{x}|\mathrm{m}-1| \ll 1 \tag{2.12}$$

where x is defined by x=$2\pi a/\lambda$ (a is a radius of a particle; λ denotes the wavelength) and m is the complex refractive index relative to the surrounding medium.

In addition, it is possible to calculate the optical properties of core-mantle dust grains by making use of an extended version of the Mie theory which is also called an "effective medium theory (EMT)" or "Maxwell-Garnett theory." A basic principle is to obtain the average dielectric function of the core and mantle materials to be applied in the Mie theory (Bohren & Huffman 1983).

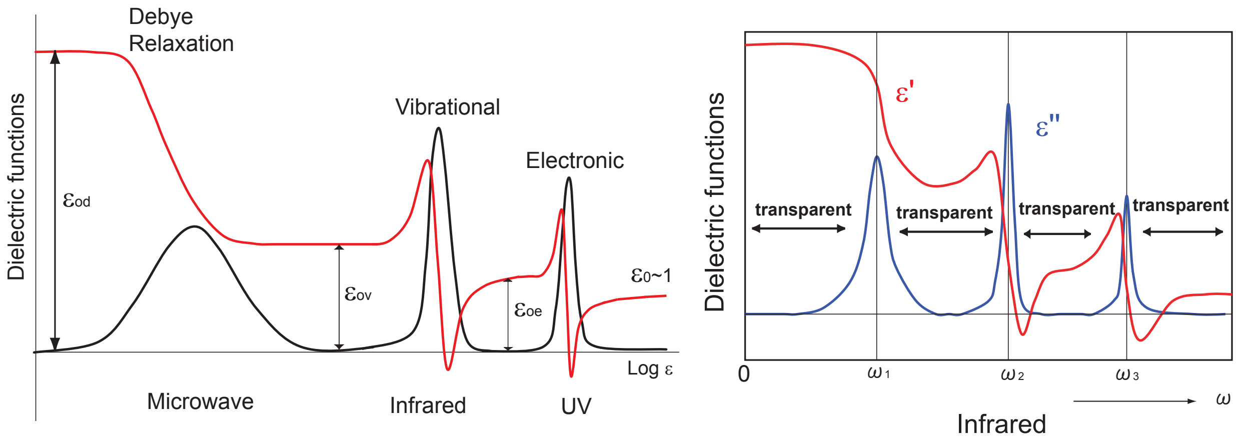

Figure 2.8: Left panel: Illustration of the dielectric function in various frequency regions (an ideal nonconductor) from Bohren & Huffman (1983). Right panel: Only the IR-region is focused for the dielectric function, ε' and ε''.

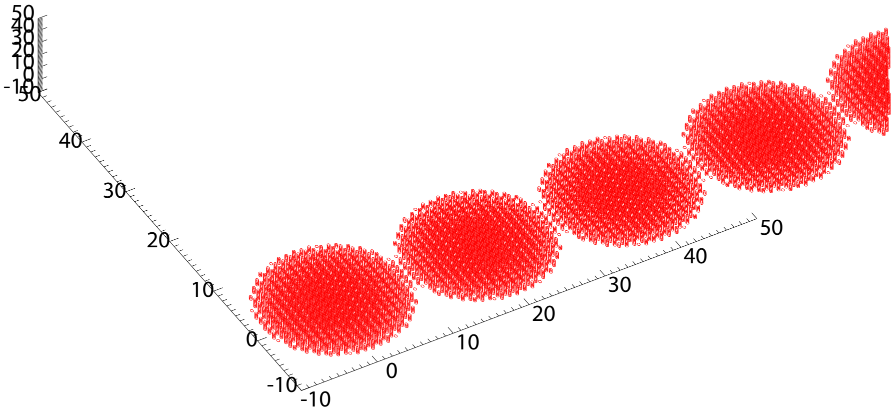

Figure 2.9: A diagram of the linear 5 clusters which are composed of numerous dipole arrays (from Mutschke, private communication).

2.7.3 Continuous distribution of ellipsoids (CDE)

In actual astrophysical environments, interstellar and circumstellar dust grains are not homogeneous spheres. It is necessary to take various particle shapes into account.

The continuous distributions of ellipsoids (CDE) method is an extended version of Rayleigh-Gans theory for randomly oriented ellipsoidal particles. Hence, the same limitations on particle size and absolute magnitude of the index of refraction are applied. Whereas a large spike of absorption can be produced from the Mie calculation when the particle size is much smaller than the wavelength, a broader absorption curve is produced via the CDE approach which is a much better approximation to the laboratory measurements (more details in Bohren & Huffman 1983).

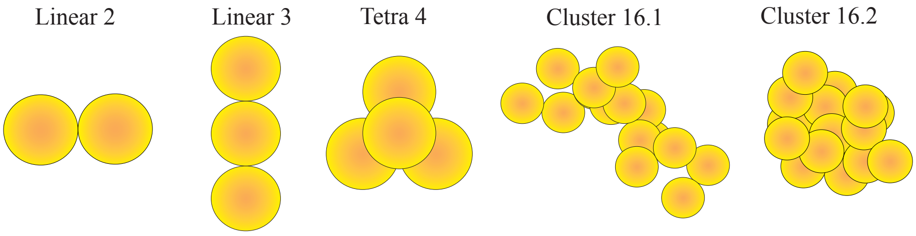

Figure 2.10: A diagram for five different geometrical shapes of clusters which are actually used in the DDA and T-matrix calculations.

2.7.4 Discrete dipole approximation (DDA)

The discrete dipole approximation (DDA) was first introduced by Purcell & Pennypacker (1973) to calculate the optical properties for arbitrary shapes and inhomogeneous structures. The fundamental concept of this method is that a solid particle is replaced by an array of N point dipoles in a lattice which has a spacing smaller than the wavelength of the incident radiation as shown in Fig. 2.9. Positions of all dipoles retain the original grain shape (see more details in e.g. Draine 1989, Draine & Goodman 1993, Draine & Flatau 1994).

The dipole numbers can be modified in the calculation. As the dipole numbers increase, the peak positions of a band shift and start stabilizing. It is necessary to utilize dipole numbers at least larger than 12000 to achieve sufficient accuracy of the calculations for the DDA (Note that the dipole numbers depend on the grain numbers and shapes, so sufficiently high numbers are needed).

The DDA (DDSCAT.6.1) code created by Draine & Flatau has been applied for comparison (info. in http://www.astro.princeton.edu/~Draine).

2.7.5 T-matrix

The T-matrix method can be used for calculating the optical properties of randomly oriented non-spherical particles (e.g. Waterman 1971, Mishchenko 1990, Mackowski 1996). The averaging, for instance, of the extinction cross-section (C_{ext}) over the uniformly oriented distribution of non-spherical particles is equivalent to the summation of diagonal elements of the T-matrix which are calculated for any single orientation of the particle with regard to the natural reference frame (Mishchenko 1990).

Basically, although it is possible to calculate the extinction efficiency for arbitrary shapes as in Fig. 2.10 with both the DDA and the T-matrix methods, the T-matrix method fails only if the particles overlap each other. In other words, the particles must stick on the surfaces mutually.

The T-matrix SCSMTM1 code developed by Mackowski (Mackowski et al. 1996) has been used for comparison with experimental results. High multipole orders should be used for increasing the accuracy of the calculations when using the T-matrix method in the same way as the DDA. At least, it is desirable to use more than 15 multiple orders.

Chapter 3

Solid State Chemistry for Astrophysical Materials

3.1 Amorphous materials

Solid materials can be divided into two categories: amorphous and crystalline solids.

First, I take amorphous solids into account. An amorphous solid is defined as ”having a considerable degree of short range order in its nearest-neighbor bonds, but not the long range order of a periodic atomic lattice” (Blakemore 1985). Precisely, long chainlike molecules are interwoven with each other in the liquid state as one of possibilities. When the temperature drops, the liquid state transforms into the solid state. At that time, as the temperature drops, the chainlike molecules do not move actively anymore; therefore, if the liquid is cooled rapidly, the molecules do not have enough time to disentangle and line up in specific orders to be crystallized. In consequence, an amorphous solid, which contains tangled and disordered molecules, is formed in the end (Brady & Holum 1988).

Typical amorphous materials are glasses (e.g. quartz glass), gels (e.g. silica gel), amorphous carbons (e.g. carbon blacks), amorphous semiconductors (e.g. amorphous silicon), ceramics, and polymers (e.g. polystyrene) (Muraishi 2004). Since I used glass materials that are produced by melting (Sec. 4.4.2) and sol-gel processing (Sec. 4.4.3) in my experiments, I only mention them in this section.

Many scientists refer to glass as a ”supercooled liquid” which signifies that the melted amorphous materials are impossible to solidify into highly structural ordered crystals since the molecules are not able to untangle themselves before they reach the glass transition point at a low temperature. Moreover, this is one of the characteristics of amorphous solids that there is no definite melting point unlike crystalline solids (Brady & Holum 1988). Because the viscosity of a glass increases as the temperature drops, it is not able to allow molecules to untangle and arrange in fixed geometric lattices (Blakemore 1985). As solid glass materials are not in thermodynamic equilibrium, it is feasible to produce different states of glass by controlling the cooling rate. For instance, a high density glass can be formed with very slow cooling (Muraishi 2004).

A sol can be defined ”a colloidal suspension of solid particles in a liquid.” When the sol is gelled to form a solid, that is a so-called ”gel”. Sol-gel processing produces amorphous materials by the use of the transformation phase from liquid into solid (I will discuss the sol-gel processing in Sec. 4.4.3) (Brinker & Scherer 1990). Differences between SiO_2 glass and silica

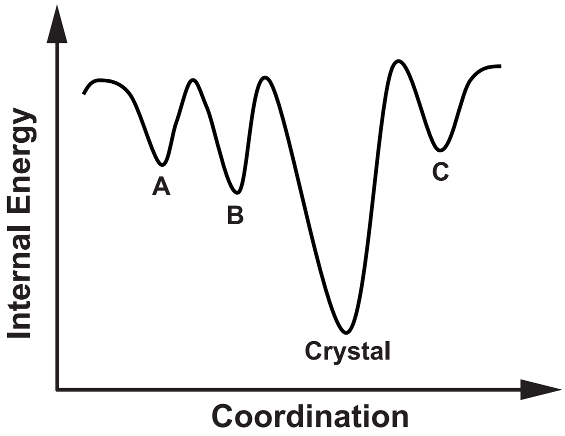

Figure 3.1: Coordinate system of atoms vs. internal energy from Saito et al. (2004).

gel (SiO_2), for example, can be identified by small angle X-ray scattering (SAXS) because X-rays reflect the electron density of material. As a result, the X-rays are scattered and then it is practicable to measure the scattering angles which allow to verify the difference in the materials (Muraishi 2004).

Since amorphous solids are composed of randomly oriented molecules, they are in unstable conditions (metastable phases) of which more than one exists depending on the coordination of the atoms. The internal energy of an amorphous material changes with the coordinate state. Then, the coordinate state of the lowest energy should be a crystalline solid which has a periodicity of the atomic coordinate system (Fig. 3.1). An amorphous solid is present at A, B, and C which is conditional on sample preparation, irradiation and heating processes, and preservational method of samples. In other words, the same amorphous materials may take different metastable states.

3.2 Crystalline materials

In contrast to amorphous solids, crystalline solids have a regular atomic arrangement in a fixed geometric pattern or lattice (Blakemore 1985). When a liquid phase of a material is cooled, there are mainly two processes that take place when crystallization occurs. The first case of crystallization occurs when a relatively low viscosity liquid reaches its freezing point at which point crystallization starts (see Fig. 3.2(a)). During this process, the temperature remains constant until the material is totally frozen. Thereafter, the temperature starts to drop again in the solid substance. Another case occurs when a liquid does not begin to crystallize even if it reaches the freezing point. In order to line up atoms in specific patterns, the temperature keeps dropping below the freezing point as shown in Fig. 3.2(b). In consequence, some part of the liquid starts to crystallize rapidly. The temperature increases and reaches the freezing point again. This time, it stays constant at the freezing point until it has frozen completely. Unlike amorphous solids, crystalline solids reveal a definite melting point (Brady & Holum 1988). Besides, it is feasible to stimulate a transition from glass to crystal by an annealing process (heating). When a glass material heats up to the glass transition point (T_g), atoms of the material start to be aligned and crystallized (Zallen 2004). Some materials used here have been formed by this process (more details in Sec. 4.4.2).

Physical properties such as hardness, conductivity, specific gravity, and melting points

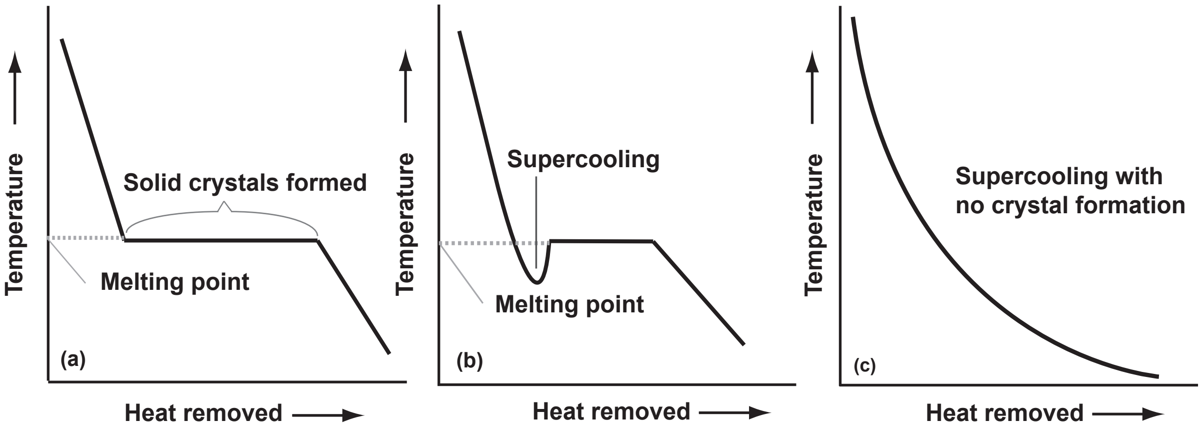

Figure 3.2: The crystallization and amorphous formation processes by temperature transitions from Brady & Holum (1988). (a) General crystallization system. (b) Supercooling crystallization. (c) Amorphous formation.

of the substances are determined by the nature and strengths of the attractive forces which sustain the atoms and/or ions to each other. Fundamentally, crystals can be classified into four types. Ionic crystals are composed of oppositely charged ions which attract each other to generate very strong ionic bonds. Due to the strong attractive force, the ions remain very tight bound; therefore, ionic crystals are very firm and tend to have high melting points. Another characteristic of ionic crystals is that they are generally brittle. When ions of opposite charge face each other, a crystal is in a stable condition. However, if the crystal experiences an external force which shifts a layer of ions, then ions of the same charge may face each other. Electrically, large repulsive forces occur and cause the crystalline solid to fracture.

Molecular crystals consist of atoms or molecules which are positioned in lattices. Unlike ionic crystals, the particles of the molecular crystals undergo rather weak intermolecular attractions (e.g. dipole-dipole forces, London forces, and hydrogen-bonding). Thus, they are soft and have low melting points. The most important forces to maintain the particles together are dipole-dipole attractions in these crystals.

Covalent crystals are formed with covalently bonded atoms which are tightly connected in lattice sites. These connections are stretched in all directions as a network for shaping a structured enormous molecule. Since the covalently bonded atoms have greatly strong attractive forces to tie them together, covalent crystals are hard and tend to have high melting points.

The final crystal pattern is metallic crystals in which positive ions constitute periodic arrangement and are embedded in an electron cloud. The electrons isolate these positive ions so they line-up properly. Because the electrons are not strictly controlled by the positive ions, they can freely move in the crystal structure which allows these materials to conduct electricity effectively. Likewise, due to the free movement of the electrons, they allow transport of kinetic energy through the crystalline solid; as a consequence, they conduct heat well. The melting point of the metallic crystals are conditional on the charge of the positive ions. For instance, since the Group IIA metals have a larger charge of the cations (Me^{2+}) in comparison to the Group IA metals (Me^{1+}), the attractive force in the electron cloud is very strong which indicates that the Group IIA metals have higher melting points than the Group IA ones (Brady & Holum 1988) (Note: Me denotes "Metal").

In a mineral structure, these bonding systems combine with each other and create different

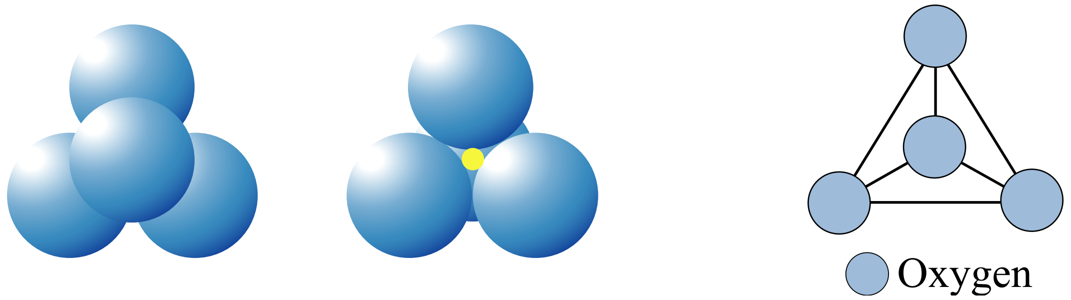

Figure 3.3: Illustrations of the $(SiO_4)^{4-}$ tetrahedron from Klein & Hurlbut (1993). Left panel: Close-packing SiO_4 tetrahedron models with different angles. Right panel: Independent tetrahedron with a unit composition $(SiO_4)^{4-}$.

types of bonding. For instance, the Si-O bond incorporates the covalent bond with ionic bond. (Wenk & Bulakh 2004). The physical properties of solid-state structures play an important role determining the response of the material to electromagnetic radiation. How are the astrophysically relevant materials structured? And how do these materials have influence on the astrophysical environments? I will look into the characteristics of the cosmic dust grains in the next section.

3.3 Physical properties of astrophysical dust grains

I focus on mainly five substances such as silica, silicates, corundum, rutile, and spinel which are considered to be condensed out from gas at relatively high temperature (T>1000K) (e.g. Grossman & Larimer 1974; Sharp & Huebner 1990). These dust grains exist in many different astrophysical environments. I describe them one by one in the next subsections.

3.3.1 Silicates (olivine, silica, pyroxene)

The presence of crystalline silicates in circumstellar disks has first been revealed by the Infrared Space Observatory (ISO) for the relatively bright young Herbig Ae/Be (HAEBE) stars (e.g. Malfait et al. 1998; Meeus et al. 2001) and for evolved stars (e.g. Molster et al. 2002) and later by Subaru/COMICS for the T Tauri star Hen 3-600 (Honda et al. 2003) and also for the well-known Vega-type star β-Pictoris (Okamoto et al. 2004). On the other hand, although crystalline silicates are lacking in the diffuse interstellar medium (ISM), it is known that 84.9 % of the amorphous grains are olivine-like and 15.1 % of them are pyroxene-like toward Sgr A* (Kemper et al. 2004). Silica has been also identified in the T Tauri stars in Chamealeon I (Meeus et al. 2003) and HD150193 in Herbig Ae/Be stars (Bouwman et al. 2001).

Silicates are defined as ”compounds containing silicon, oxygen, and one or more metals with or without hydrogen” (Lewis 1993). In other words, silicates are composed of metallic elements combined with either single or connected Si-O tetrahedra $(SiO^{-4})_4$ that form a basic unit of silicate structure (Pellant 1992). Silicates can be primarily divided into two mineral groups: olivine and pyroxene. The olivine structure is formed with isolated tetrahedra (Fig. 3.3), which are linked by chains of (Fe, Mg)O_6 octahedra (Pellant 1992). One isolated tetrahedron contains four oxygen ions (O^{2-}) at the vertices of the tetrahedron and a silicon ion (Si^{4+}) is positioned to the center of the four oxygen anions resulting in a Si:O ratio of 1:4, such as in forsterite (Mg_2SiO_4) (Wenk & Bulakh 2004). A silicon cation is sharing its total bonding

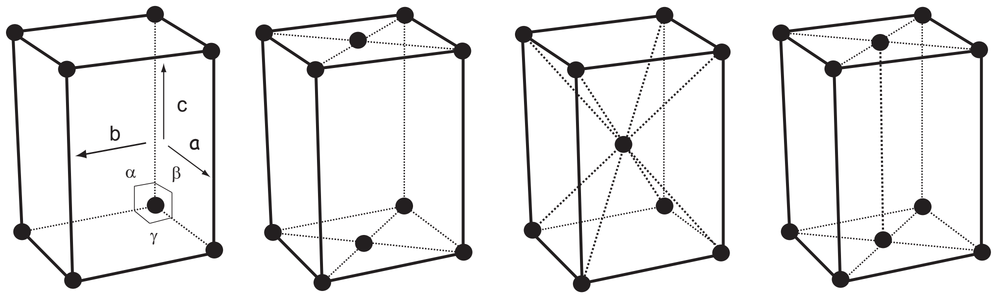

(a) Simple orthorhombic ($a \neq b \neq c$, $\alpha=\beta=\gamma=90^\circ$)
(b) base-centered orthorhombic ($a \neq b \neq c$, $\alpha=\beta=\gamma=90^\circ$)
(c) body-centered orthorhombic ($a \neq b \neq c$, $\alpha=\beta=\gamma=90^\circ$)
(d) face-centered orthorhombic ($a \neq b \neq c$, $\alpha=\beta=\gamma=90^\circ$)

Figure 3.4: Illustration of the orthorhombic crystal system which has four different sorts of Bravais lattice from Saito et al. (2004).

energy with the four oxygen anions even though there exists electron sharing in the Si-O bond. The single Si-O bond strength is equivalent to half of the total bonding energy in the oxygen anion since each oxygen anion might bond to a Si cation of another tetrahedron to share the oxygen anion. The potential number to bond the oxygen anion with the silicon cation differs (it may be one, two, three, or all four of the oxygen anions in the tetrahedron) that affect structural arrangements (Klein & Hurlbut 1993). Also, the general sum formula is a useful tool to describe the olivine group as $A^{2+}B^{2+}SiO_4$ (A and B are divalent cations) (Jäger et al. 1998). Particularly, Mg^{2+} and Fe^{2+} divalent cations are considered to be dominating to form silicate, and major refractory materials in astrophysical environments are forsterite and fayalite (Fe_2SiO_4). It is possible to substitute Mg^{2+} for Fe^{2+} and vise versa to form forsterite and fayalite, respectively (Jäger et al. 1998).

Olivine belongs to the orthorhombic crystal system. There are seven crystal systems which are described by a group of geometric symmetries with a fixed point to make a point group in a lattice. In an orthorhombic system, though all axes meet angles of 90° ($\alpha=\beta=\gamma$), the lengths of the cell are not equal ($a \neq$b$\neq$c) (Fig. 3.4; more details in e.g. Muraishi 2004, Blakemore 1985, Ibach & Lüth 1991, Wenk & Bulakh 2004).

The idealized structural view of crystalline forsterite is shown in Fig. 3.5. Fig. 3.5(a) presents two layers of hexagonal close-packing structure of oxygen in forsterite. Mg^{2+} ions are precisely arranged in octahedral interstices, and tetrahedral interstices are filled with Si^{4+} ions. Fig. 3.5(b) represents an octahedral coordination. The differences in the color denote the levels along the a-axis. Si^{4+} ions occupy the tetrahedral interstices. Only Mg^{2+} ions are ordered in the octahedral interstices together with tetrahedra in Fig. 3.5(c) (Wenk & Bulakh 2004).

In fact, distortions occur in the crystalline structure. There are two slightly different shapes of octahedra which are so-called M1 and M2. M1 is more distorted than M2 which are shown in Fig. 3.6 (left panel). As for the olivines, (Mg, Fe)$_2$SiO$_4$, Mg fills up the M1 site, and Fe^{2+} ions occupy the M2 site (Wenk & Bulakh 2004; Klein & Hurlbut 1993). A "ball and stick model" of crystal olivine structure is shown in Fig. 3.6 (right panel).

Furthermore, the magnesium to iron ratio of the olivine can be modified. The general formula of the olivine composition is expressed as $Mg_{2y}Fe_{2-2y}SiO_4$. The subscript y is in the range $0 \leq y \leq 1$. By dint of the subscript variation, iron-rich or magnesium-rich olivine materials could be prepared as samples. 8 to 20 mass percent of FeO is contained in the mineral olivine. The iron content of the olivine materials has an influence on band profiles (Jäger et al. 1998). For example, Koike et al. (2003) measured absorption spectra of crystalline olivines

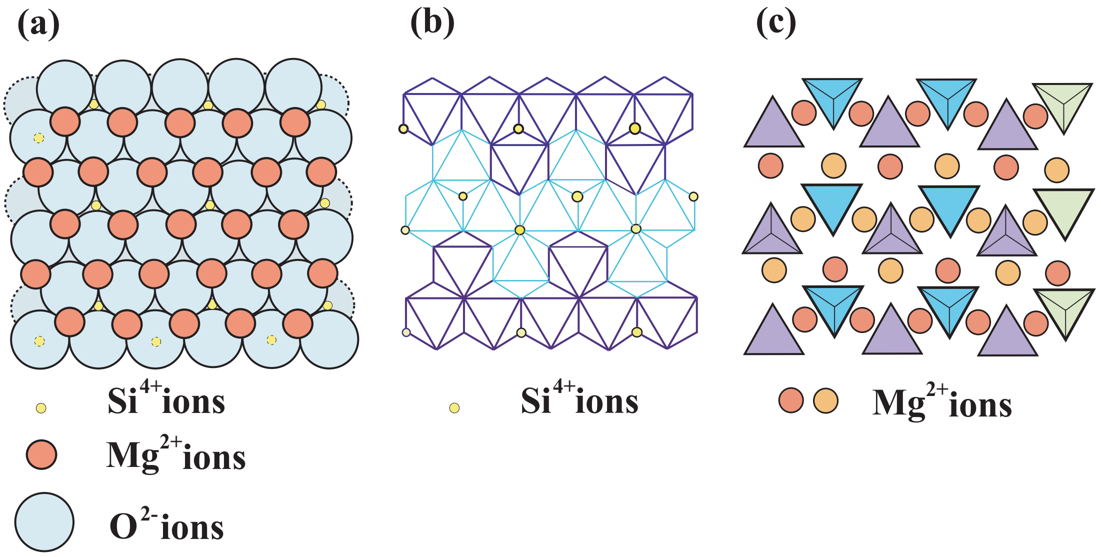

Figure 3.5: Different aspects of idealized crystalline forsterite structures from Wenk & Bulakh (2004). (a) Close-packed structure with two layers. (b) An illustration of the octahedral coordination with two layers. The lower layer is denoted by light blue color. The tetrahedral ions (Si^{4+}) (yellow circles) occupy the tetrahedral interstices. (c) Illustration of the tetrahedral coordination and the octahedral ions (Mg^{2+}).

with a range of Mg/(Mg+Fe) in a laboratory experiment. The peak positions of forsterite (the Mg-rich crystalline olivine (Mg_2SiO_4)) shift linearly to shorter wavelengths when the Fe-rich fayalite (Fe_2SiO_4) is reached. As the Fe content increases, metal oxygen distances in the crystal are stretched in the solid olivines which causes a broadening of the bands (Jäger et al. 1998).

Although silica (SiO_2) does not exactly correspond to the definition of silicate, at this point, I will describe it since SiO_2 plays a quite important role on silicate formation via chemical reaction. Unlike the silicates, silica belongs to the hexagonal crystal system the unit cell of which is a hexagonal based right prism (Fig. 3.7, left panel). The melting point of SiO_2 (quartz) is 1610°C (Lide 1990). SiO_2 is also composed of the basic unit of silicate minerals which is the tetrahedron $(SiO_4)^{4-}$. In the crystal structures of silica, all four oxygen ions of the tetrahedra are shared with neighboring ones in a three-dimensional framework (see Fig. 3.7 right panel). Thus, the Si:O ratio becomes 1:2 in this system ($O=4\times1/2$) (Wenk & Bulakh 2004).

In the presence of free SiO_2, forsterite is not stable and both forsterite and silica cause a chemical reaction. The reaction can be expressed in a chemical equation:

$$Mg_2SiO_4(\text{forsterite}) + SiO_2(\text{silica}) \longrightarrow 2MgSiO_3(\text{enstatite})$$

In consequence, enstatite is formed via this reaction (Klein & Hurlbut 1993).

A general formula of pyroxenes can be represented as XYZ_2O_6 where X signifies Fe^{2+}, Mg^{2+}, Ca^{2+}, Mn^{2+}, Na^{+}, and Li^{+} in the M2 crystallographic site. Y indicates Mn^{2+}, Fe^{2+}, Mg^{2+}, Fe^{3+}, Al^{3+}, Cr^{3+}, and Ti^{4+} in the M1 site. Z designates Si^{4+} and Al^{3+} in the tetrahedral sites of a single chain site. In general, the X cations are larger than the Y cations in size. The pyroxenes can be classified into several groups which are enstatite ($MgSiO_3$), wollastonite ($CaSiO_3$), and ferrosilite ($FeSiO_3$) (Klein & Hurlbut 1993). I focus only on enstatite here. The

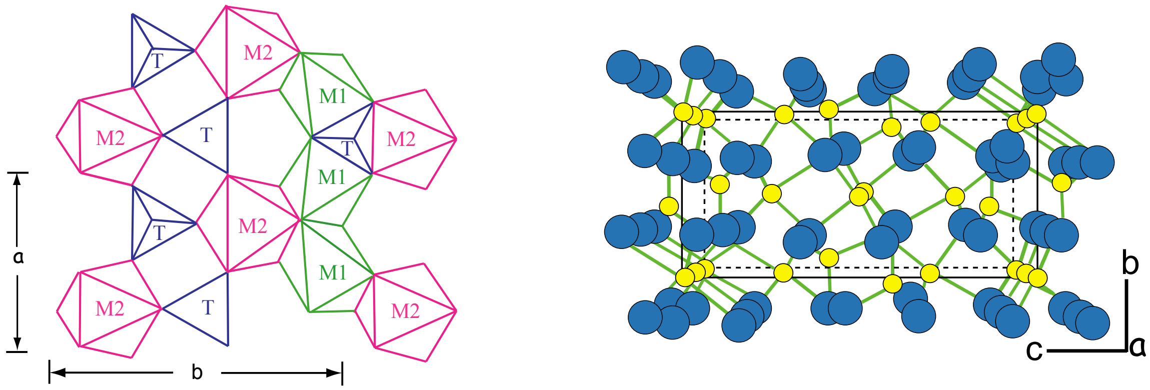

Figure 3.6: Left panel: Illustration of actual olivine crystalline structure with both octahedra and tetraheda sites from Wenk & Bulakh (2004). T indicates the tetrahedra site whereas M1 and M2 designate the octahedra sites. M1 (Mg) octahedra are exceedingly distorted compared to M2 (Fe^{2+}) ones in the olivine case. Right panel: A ball and stick model for the crystal structure of olivine $(Mg, Fe)_2SiO_4$ from Bartelmehs (1997).

$(SiO_4)^{-4}$ tetrahedra form a single tetrahedral chain in which two O^{2-} ions of each tetrahedron are shared with neighboring tetrahedra. This structure is called inosilicates structure class (Fig. 3.8, left panel). The resultant Si:O ratio in this enstatite system will be 1:3 (Werk & Bulakh 2004). Thus, pyroxene structure is originated in single SiO_3 chains that are parallel to the c-axis.

Most pyroxenes belong to the crystal systems orthorhombic (space group Pbc*a*) shown in Fig. 3.4 and monoclinic (space group $P2_1/c$) in Fig. 3.8 (right panel) (Klein & Hurlbut 1993). When pyroxenes hold cations which have significantly larger radii than Mg^{2+} (e.g. Ca^{2+}) ions, these pyroxenes are the so-called clinopyroxenes and classified into the monoclinic crystal system. Synthetic Mg-pyroxenes, which are produced via a melting process, normally belong to this kind (Jäger et al. 1998). In contrast to the orthorhombic crystal system, the monoclinic system has a pair of perpendicular vectors, and one angle β can be other than 90° (Saito et al. 2004). Natural $MgSiO_3$, which is formed by the monoclinic crystal structure, has a melting point at 1557°C (Lide 1990). Conversely, the most familiar Mg-Fe pyroxenes are regarded as orthopyroxenes and classified into the orthorhombic system. These orthopyroxenes vary their names with FeO content. If an orthorhombic pyroxene has an FeO content between 0 to 5 mass %, it will be called enstatite. Similarly, when it has the FeO content between 5 and 15 mass %, a pyroxene is known by the name of bronzite. Hypersthene is a pyroxene which FeO content must be in a range between 15 and 34 mass %. Although ferrosilite is also a well known pyroxene, it is not present as a natural mineral (Jäger et al. 1998; Rudolph 2004).

When IR radiation interacts with crystalline materials, molecular and crystal lattice vibrations are induced, and IR absorption takes place due to the TO phonon vibration (see more details in Sec. 2.6 & 2.7.1). As a result of that, the silicon-oxygen tetrahedra vibrations generate a lot of narrow bands from the mid-IR to the far-IR regions. These narrow bands in the wavelength range between 9 and 12.5 μm (800-1100 cm^{-1}) are caused by different asymmetric and symmetric stretching vibrations of the SiO_4 tetrahedra. Likewise, bending vibrations of the SiO_4 tetrahedra produce bands between 14.29 and 21.28 μm (700-470 cm^{-1}) in wavelength. Translational motions of metal cations within the oxygen cage and complex translations involving metal and Si atoms lead to complex bands beyond 21.28 μm (470 cm^{-1}) in wavelength (more details in Servoin & Piriou 1973; Dorschner & Henning 1986; Hofmeister 1997; Henning

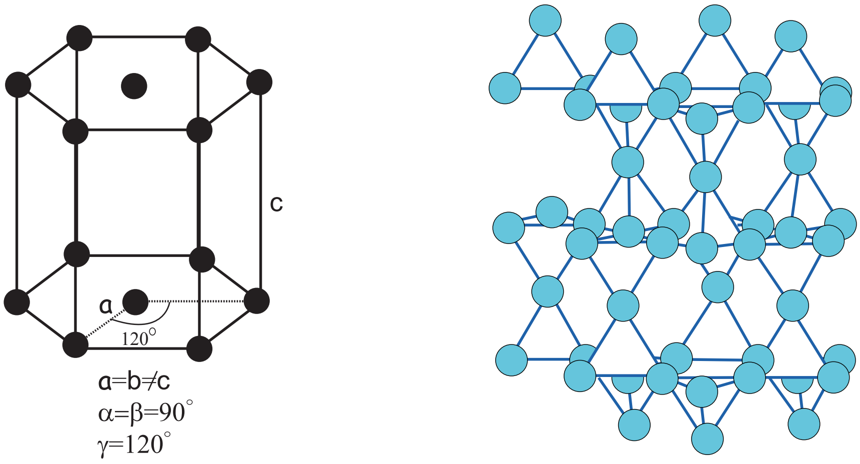

Figure 3.7: Left panel: Illustration of the hexagonal crystal system which has only one type of Bravais lattice from Saito et al. (2004). Right panel: Representation of infinite tetrahedral network SiO_2 crystal structure in polyhedral model from Wenk & Bulakh (2004).

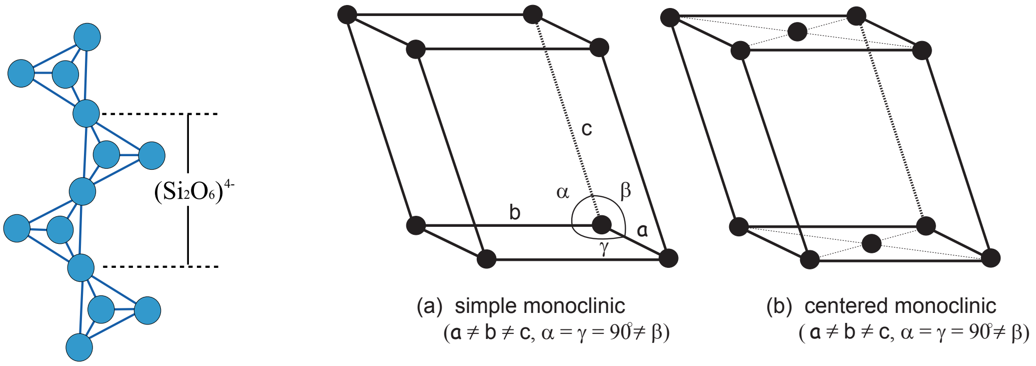

(a) simple monoclinic
($a \neq b \neq c$, $\alpha = \gamma = 90° \neq \beta$)

(b) centered monoclinic
($a \neq b \neq c$, $\alpha = \gamma = 90° \neq \beta$)

Figure 3.8: Left panel: Illustration for the arrangement of SiO_4 tetrahedra with a polyhedral model on enstatite from Klein & Hurlbut (1993). Right panel: Representation of the monoclinic crystal system which has two different kinds of Bravais lattice from Saito et al. (2004).

et al. 2005).

3.3.2 Spinel ($MgAl_2O_4$)

The origin of our solar system took place in a molecular cloud of interstellar gas and dust. Specifically, planet formation has been considered to occur when solid dust grains start to stick together in the accretion disk surrounding a protostar to form larger bodies. A complete understanding of planet formation requires a search for the highest temperature condensation material in order to find the whole temperature sequence of the condensation process.

According to the results of the condensation temperature from Sharp & Huebner (1990), ZrO_2 at temperature 1807 K is the first species to condense out from the gas followed by Al_2O_3 (1716 K), $CaTiO_3$ (1639 K), $MgAl_2O_4$ (1497 K), Mg_2SiO_4 (1411 K), $MgSiO_3$ (1336 K) at a pressure of 4.935×10^{-4} atm, which is relevant to dust grain formation in protostellar environments. Similarly, in the condensation calculations of Grossman & Larimer (1974), Al_2O_3 is the first mineral to appear at temperature 1758 K, and then $CaTiO_3$ (1647 K), $MgAl_2O_4$,

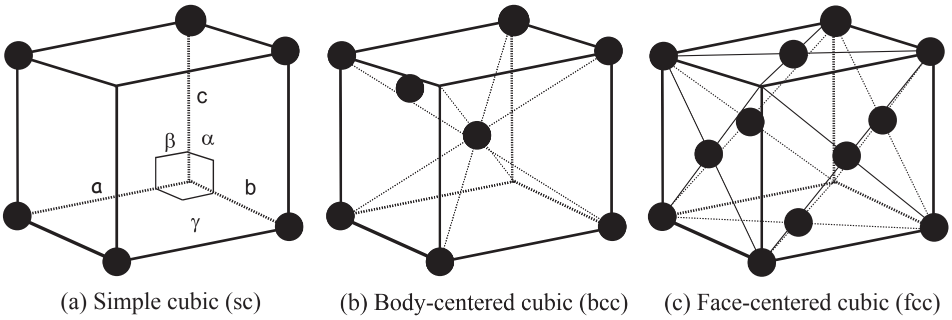

(a) Simple cubic (sc) (b) Body-centered cubic (bcc) (c) Face-centered cubic (fcc)

Figure 3.9: Illustration of the cubic crystal system which has three different sorts of Bravais lattice from Saito et al. (2004). Spinel belongs to (c) face-centered cubic.

Mg_2SiO_4 (1444 K), $MgSiO_3$ (1349 K), and TiO_2 (1125 K) with the pressure at 10^{-3} atm (see the complete lists of their calculations in Appendix A).

Spinel is considered to be a high condensation temperature material. Investigation of spinel has been performed mostly in the outflow of oxygen-rich asymptotic giant branch (AGB) stars that a large amount of dust grains can be produced with favorable temperature and pressure (see Chap. 2). In fact, the 13 μm feature in the spectra of oxygen-rich AGB stars has been investigated diligently by many scientists. It has been suggested that it might be caused by spinel (Posch et al. 1999; Fabian et al. 2001), α-Al_2O_3 (e.g. Glaccum 1995), γ-Al_2O_3 (e.g. Koike et al. 1995; Begemann et al. 1997), silica (e.g. Speck 1998; Fabian et al. 2000), and different kinds of silicates (e.g. Koike et al. 1989; Jäger et al. 1994; Dorschner et al. 1995). In addition, in the atmospheres of brown dwarfs, spinel, silicates, and corundum are thought to be highly abundant dust species (Allard et al. 2001), and a large amount of presolar spinel grains has been discovered in the Krymka unequilibrated ordinary chondrites (Nittler et al. 2005).

The orthorhombic olivine structure transforms into a cubic spinel structure which has Si in tetrahedral sites and Mg^{+2} and Fe^{2+} in octahedral sites under very high pressures (Suito 1972). In comparison with the olivine structure, the spinel structure is 12 % denser than that of the olivine (Klein & Hurlbut 1993). Hence, spinel and olivine have very similar structures. The olivine structure is a hexagonal close-packed anion arrangement whereas spinel has a cubic close-packed anion arrangement (Gregory 2001). A cubic crystal system has equal cell length (a=b=c) and makes all right angles ($\alpha=\beta=\gamma=90°$) in Fig. 3.9. Most metallic crystals take the shape of the cubic system (Saito et al. 2004).

The general formula of the spinel group can be described as XY_2O_4. X would be replaced with Mg^{2+}, Fe^{2+}, Ti^{4+}, Zn^{2+}, or Mn^{2+}. Y may be occupied by Al^{3+}, Fe^{3+}, Fe^{2+}, or Cr^{3+}. Take magnesium aluminum spinel ($MgAl_2O_4$), for example. The oxygens form a face-centered cubic close-packed array along planes in the structure. Then, Mg^{2+} ions are placed in tetrahedral interstices (1/8 occupied) whereas Al^{3+} ions sit in octahedral (1/2 occupied) sites in the lattice. 8 tetrahedral sites are occupied by Mg^{2+} ions, and 16 octahedral sites are filled by Al^{3+} ions surrounded with 32 O^{2-} ions in a unit cell of the spinel. In consequence, spinel has 56 ions per unit cell (see Fig. 3.10) (Klein & Hurlbut 1993). This structure type belongs to ”normal spinel.” The other type of spinel is call ”inverse spinel” structure in which 8 out of 16 Al^{3+} ions (Y part) are placed at the 8 tetrahedral sites. The general formula of inverse spinel will be expressed by $Y(YX)O_4$. Although X cations are generally larger in radius, this concept cannot apply in the normal spinel structure because crystal field stabilization should be a prime concern rather than the geometric aspects of the ions. As a result, the larger cations might fill in the tetrahedral sites (see more details in Klein & Hurlbut 1993).

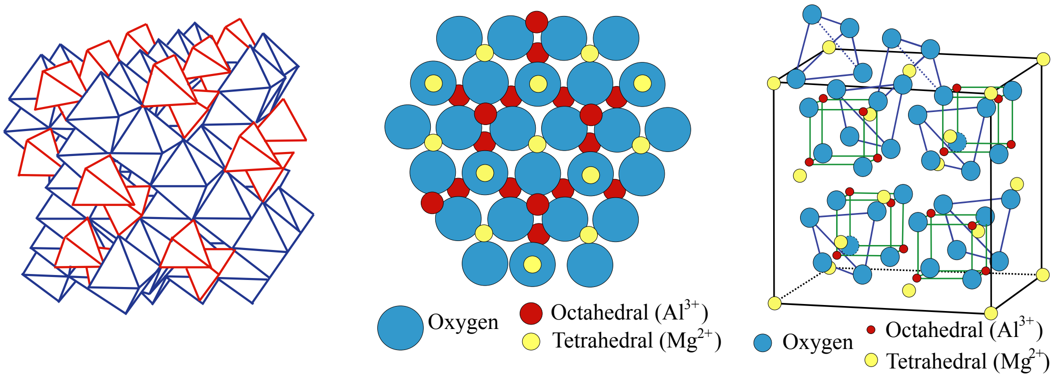

Figure 3.10: Left: Polyhedral model of spinel structure. Octahedral (Al^{3+}: blue) and tetrahedral (Mg^{2+}: magenta) polyhedra are shown in a cubic close-packed structure from Gregory (2001). Center: Representation of the cubic crystal system of $MgAl_2O_4$ in close-packing model from Wenk & Bulakh (2004). Right: The ball & stick model of the $MgAl_2O_4$ cubic unit cell together with tetrahedral and octahedral cations and oxygen anions on the left from Wenk & Bulakh (2004).

$MgAl_2O_4$ can be found as a natural mineral and can also be produced by a synthesis. Both natural and synthetic crystal structures have disordering due to heating. With respect to the optical properties of $MgAl_2O_4$, disordering in spinel crystals is due to heating (e.g. Schmocker 1972), the structural transition occurs at temperature between 750 and 800 °C. The melting point is in the range between 2378 and 2408 K. The polycrystalline spinel particles are affected mainly by scattering in the visible and near-IR region. As the wavelength increases, the scattering efficiency of bulk spinel decreases. The source of absorption in near-IR range is predominately multiphonon absorption. The fundamental (one-photon) lattice vibrations of spinel generate bands between 12.5 and 33.3 μm (800-300 cm^{-1}) (Tropf & Thomas 1991).

3.3.3 Aluminum dioxide (Al_2O_3; α- and γ-corundum)

Aluminum oxides crystallize into a form of corundum, which is the second hardest natural mineral. This hardness might be caused by the strong and short O-Al bonds which attract O^{2-} ions and Al^{3+} ions close together in order to form a tremendously hard and dense close-packed crystal structure in spite of the low atomic mass elements which lead to a weak covalent bond. Astrophysically, though it also depends on the morphological aspects and solid state structure of the grains, it has been thought that α-Al_2O_3 or/and γ-Al_2O_3 may be the carrier of the 13μm feature as well as spinel (e.g. Onaka et al. 1989; Posch et al. 1999; Fabian et al. 2001). Moreover, there is a potential for both α and γ-Al_2O_3 grains in brown dwarf atmosphere via a theoretical approach (Ferguson, private communication). Corundum has been found in the carbonaceous chondrites (Greshake et al. 1996) and the Krymka unequilibrated ordinary chondrite as well (Nittler et al. 2005).

α-Al_2O_3 belongs to the rhombohedral (or trigonal) crystal structure (Fig. 3.11, left panel) (Saito et al. 2004) and is considered to be one of the early condensation species in a cooling gas environment of solar composition (Begemann et al. 1997). The melting point is in the range between 2000 and 2030°C (Lide 1990). In the crystal structure of α-Al_2O_3, the O^{2-} ions are arranged in a hexagonal closed-packing, and the Al^{3+} ions occupy 2/3 of the octahedral interstices which is shown in Fig. 3.11 (center panel). One Al^{3+} ion is surrounded by 6 O^{2-} ions whereas one O^{2-} ion is enclosed within 4 Al^{3+} ions. Thus, the Al:O ratio will be 6:4

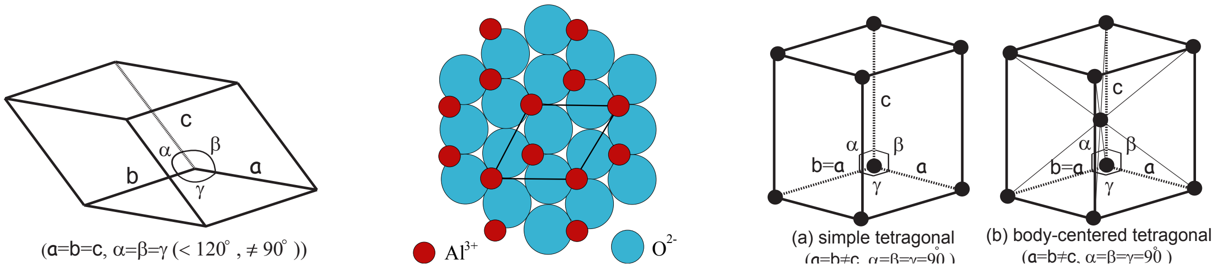

Figure 3.11: Left: Illustration of the rhombohedral crystal system from Saito et al. (2004). Center: Close-packing model of α-Al_2O_3 from Wenk & Bulakh (2004). Right: Illustration of the tetragonal crystal system which has two different sorts of Bravais lattice from Saito et al. (2004).

(Muraishi 2004).

I also take γ-Al_2O_3 into account. γ-Al_2O_3 has the tetragonal crystal structure (Fig. 3.11, right panel) (Koike et al. 1995; Saito et al. 2004). γ-Al_2O_3 is a so-called "defect-spinel" because it has basically the same structure as spinel (Gregory 2001). Since γ-Al_2O_3 does not have Mg cations, Al cations occupy the Mg sites. As a result, a stoichiometry becomes Al_3O_4. It is necessary to remove 8/3 Al^{3+} ions from the 24 available in the spinel unit cell in order to correct stoichiometry. Then, the unit cell contains 96 O^{2-} ions, 64 Al^{3+} ions, and 8 spinel cation vacancies. These vacancies are randomly distributed and have not been verified the exact locations (Streitz et al. 1999)

Al-O vibrations are induced in the mid-IR region (Begemann et al. 1997). A weak band at approximately 20 μm (500 cm^{-1}) has been confirmed. There exist the longitudinal optical mode (LO) around 19.46 μm (514 cm^{-1}) due to the extraordinary ray (the electric field polarized parallel to the c-axis) and the LO mode at 20.75 μm (482 cm^{-1}) owing to the ordinary ray (the electric field polarized perpendicular to the c-axis) (Gervais 1991). Especially for γ-Al_2O_3, there exist vibrational frequencies in the range from 12.5 to 14.29 μm (680-500 cm^{-1}) and from 14.71 to 20 μm (800-700 cm^{-1}) (Saniger 1995).

3.3.4 Titanium dioxide (TiO_2; rutile, anatase, brookite)

Titanium dioxide (titanium (IV) oxide or titania) is a highly refractory materials as well and has been discovered in meteorites such as the carbonaceous chondrites (Greshake et al. 1996) and the Krymka unequilibrated ordinary chondrite (Nittler et al. 2005). Furthermore, Jeong et al. (1999) suggested that TiO_2 would be the most promising candidate as the nucleation seed in oxygen-rich circumstellar dust shells around long-period variables. Although TiO_2 is not abundant in comparison to silicates, it is conceivable that TiO_2 plays a key role in the condensation and grain growth processes in astrophysical environments.

TiO_2 has three different crystal structures. Rutile belongs to the tetragonal crystal system (Fig. 3.12(a)) and is the most stable form of titanium dioxide. It is formed at the highest temperatures (melting point 1850°C) (Lide 1990). Anatase is a member of the tetragonal crystal system as well (Fig. 3.12(b)). The total density of anatase is approximately 10% less than that of rutile (Linsebigler et al. 1995). It can be transformed into rutile at temperature above 1200K by thermal annealing (Won et al. 2001). The melting point of anatase is slightly lower than that of rutile (1835°C, Reade Advanced Materials 1997). In crystal structure, rutile and anatase consist of basic structural unit of TiO_6 octahedron. Each Ti^{4+} ion occupies the center of the oxygen octahedra, so that it takes the shape of surrounding by 6 O^{2-} ions. Conversely,

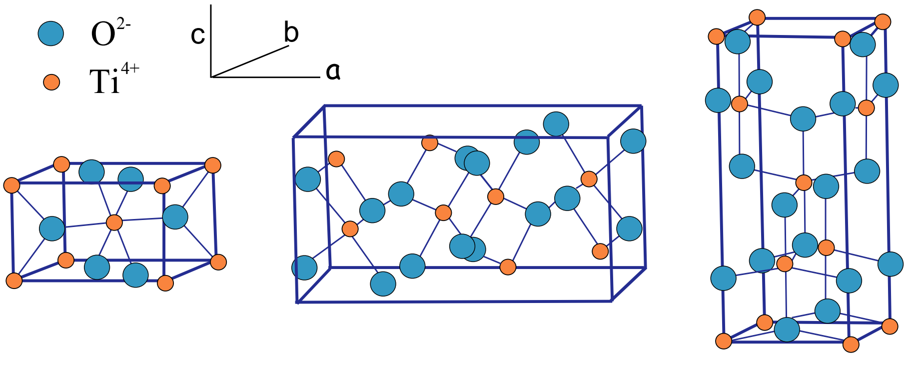

(a) Rutile (b) Anatase (c) Brookite

Figure 3.12: Illustrations of three different titanium dioxide crystal structures in ball and stick model from Mo et al. (1995). (a) Rutile (b) Anatase (c) Brookite

since each O^{2-} ion is enclosed by 3 Ti^{4+} ions, the Ti:O ratio will be 3:6 (see in Fig. 3.12(a) and (b)). In both cases, TiO_2 octahedra are distorted and anatase has more distortions than rutile. Brookite, on the other hand, is associated with the orthorhombic crystal system and has a more complicated structure compared with rutile and anatase. Brookite has 6 different Ti-O bonds and 12 different O-Ti-O bond angles whereas rutile and anatase have 2 sorts of Ti-O bond and O-Ti-O bond angles (Fig. 3.12(c)). Brookite has the lowest melting point (1825°C, Lide 1990) (see more details in Mo et al. 1995, Klein & Hurlbut 1993, Muraishi 2004). I focus only on rutile in my experiment because of the highly probable relevance.

The TO vibration of the Ti-O bonds induce a broad peak in the wavelength range between 16.7 μm (600 cm^{-1}) and 25 μm (400 cm^{-1}). Likewise, the LO vibrational mode is relevant to the region between 13.3 μm (750 cm^{-1}) and 14.3 μm (700 cm^{-1}) in wavelengths. Two absorption bands can be seen at approximately 11.8 μm (850 cm^{-1}) and 12 μm (830 cm^{-1}) (Busani & Devine 2005).

Chapter 4

Experiment

4.1 Aerosol technology

So far laboratory measurements on real particle ensembles have not been able to provide exact band profiles for a direct comparison due to the use of an embedding medium (KBr) in the sample preparation, which changes the band profile substantially by the influence of its electromagnetic polarization (Fabian et al. 2001). Hence, I apply the aerosol technique (e.g. Hinds 1999) for measuring extinction spectra in the mid-IR region of both amorphous and crystalline samples while avoiding the effect of electromagnetic interaction with solid embedding media. Thereafter, I make a comparative study of the band profiles which are measured through both methods in the entire experiments.

I start with a lucid exposition of the aerosol and the KBr pellet techniques. Later, I introduce the experimental devices of the aerosol measurement with specifying the important parts and the samples used.

4.1.1 Aerosol particles

A definition of an aerosol is "a suspension of solid or liquid particles in a gas. Aerosols are usually stable for at least a few seconds and in some cases may last a year or more. The term aerosol includes both the particles and suspending gas, which is usually air. Particle size ranges from about 0.002 μm to more than 100 μm" (Hinds 1999). Consequently, the study of physical principles, behavior, and properties of aerosols in order to apply these knowledges to the subject of one's research with a microscopic viewpoint is the so-called "aerosol technology."

Aerosols are fundamentally two-component systems, which consist of a suspending medium (air or gas) and the suspended particles. For understanding the properties of individual particles, the microscopic approach is necessary so as to analyze:

- How a particle moves in the suspending gas
- How a particle interacts with the suspending gas
- How the forces are exerted on a particle
- How a particle behaves with electromagnetic radiation
- How particles attract each other

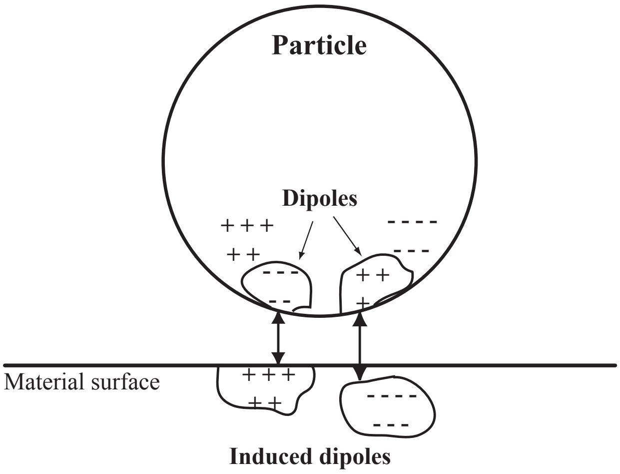

Figure 4.1: Illustration of van der Waals adhesive force from Hinds (1999).

These problems strongly depend on the particle size and the concentration in the suspending medium. Particularly, the essential understanding of how aerosol properties change with particle size is the most important factor to characterize the behavior of aerosols.

Besides, if the particle size increases and comes close to the space between the gas molecules, the particle motion is tremendously resisted by the gas. In other words, variation of the particle size controlls the resistance of the gas. Aerosol particles share energy with gas molecules. As a result, Brownian motion, which is the random movement of the particles through the gas, continuously occurs (see more details in Sec. 4.1.3).

4.1.2 Adhesiveness

Once the solid particles are suspended in a gas, they undergo the adhesion to form agglomerate particles. The adhesive forces are induced by a Coulomb force, the van der Waals force, and the force from the surface tension of adsorbed liquid films. There are various crucial factors to govern these forces on the particles such as:

- Shape and size
- Surface roughness
- Surface contamination
- Moisture
- Temperature
- The duration of contact
- The initial collision velocity

Especially, the van der Waals force is the most important force for the adhesion of the aerosol particles. It is an intermolecular attractive force that molecules draw each other at adequate distances (e.g. Atkins 1994). Fundamentally, a material is electrically neutral; however, because electrons are moving randomly in the material, polarization occurs instantaneously in

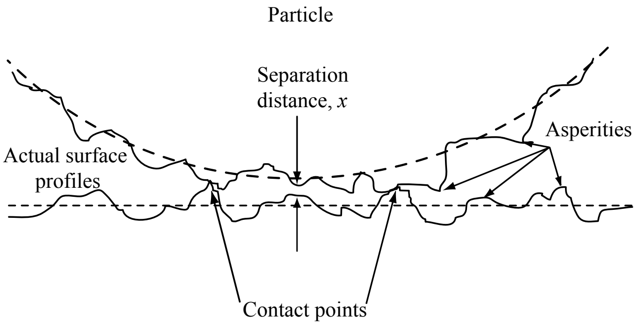

Figure 4.2: Microscopic view of a contact between a particle surface and a rough material surface from Hinds (1999).

random directions. It signifies that these electrons generate dipoles which are temporary areas of concentrated charge as shown in Fig. 4.1. These temporary dipoles induce corresponding dipoles in the nearby material, which causes the van der Waals attractive forces. As the distance between a particle surface and a surface of neighboring material increases, the van der Waals forces decrease quickly. Thus, the forces are effectively functioning only within a few molecular diameters. In reality, most surfaces are not smooth and more like uneven asperities as shown in Fig. 4.2. Only a few peaks of the asperities can keep practically in contact with a particle surface; therefore, in most cases, there is an average distance x for the separation between the particle and material surfaces which are conditional on the degree of surface roughness. The distance x for smooth surfaces is generally considered to be 0.4 nm. The asperities undergo the deformation slowly due to the influences of both the van der Waals and the Coulomb forces. Then, the separation distance between a particle and a material surfaces is reduced, and at the same time, the contact area increases until staying balanced between these attractive forces and the forces against the deformation. The strength of the adhesive forces is controlled by the hardness of the materials. For instance, in case of soft materials, flattening could increase the adhesive force by up to 15-fold, similarly to 100-fold in a case of plastics (Tsai et al. 1991).

A second attractive force is the Coulomb force. Particles, which are larger than 0.1 μm in diameter, carry some small net charge q. This net charge induces an equal amount of opposite charge in the surface that causes the attractive electrostatic force. It is possible to achieve a condition that the minimum charge of an aerosol particle can be zero. There are essentially two processes of the charge transformation in this system. One is that if aerosol particles are initially neutral, they will obtain charge via collision with air (or gas) ions because of their random thermal motion. Another is that if aerosol particles are initially charged, they will lose their charge gradually since these charged particles attract oppositely charged ions. So, these two processes lead to an equilibrium charge state which is described by the Boltzmann equilibrium charge distribution. Under this circumstance, the equilibrium charge of particles larger than 0.1 μm is approximately proportional to $\sqrt{\mathrm{d}}$ where d is the particle diameter; therefore, the electrostatic adhesion force is proportional to the first power of particle diameter.

Moisture on the molecules under normal condition must be taken into account in aerosol mechanics. Nearly all materials contain adsorbed liquid molecules on their surfaces. The third attractive force is produced by the surface tension of the liquid which pulls the particle surface at the point of contact as shown in Fig. 4.3. If the real surfaces have lower relative humidities (< 90 %) (Hinds 1999), the curvature of asperities at the points of contact has a

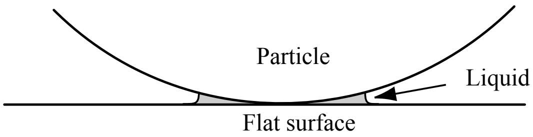

Figure 4.3: Illustration of adhesive force caused by a liquid film from Hinds (1999).

strong influence on the surface tension attractive force rather than the particle diameter. This curvature significantly changes from particle to particle and leads to a distribution of adhesive forces for the same particle size.

In general, the van der Waals and the surface tension forces are greater than the electrostatic forces except for highly charged particles. Although adhesive forces are proportional to d, removable forces are proportional to d^2 for air current force, and d^3 for gravitational, vibrational, and centrifugal forces. These relationships indicate a relevance to the detachment and the size of particles. As the particle size decreases, it is getting more difficult to remove particles from the surfaces. Particle size less than 10 μm are greatly affected by the adhesive force on a particle more than any other forces. If particles adhere very tightly to form a larger agglomerate, they can be easily swept away or shaken from the surface.

When a solid particle has low approach velocity (less than few m/s) to contact a surface, it loses its kinetic energy by both deforming itself and the surface. At high velocities, though a part of the kinetic energy is vanished into the deformation, another part is elastically converted to kinetic energy of rebound. If the rebound energy exceeds the adhesive energy, a particle will bounce away from the surface. When a solid particle has high approach velocity to contact a surface, it has the greater deformation, and maximum rebound velocities happen at in-between (medium) approach velocities. The three conditions (the particle material is harder, the particle size is larger, and its high approach velocity) cause the bounce readily even though surface roughness plays an important role. Furthermore, in order to increase the adhesion energy, the deformation, and the dissipative energy, it is very effective to coat the surfaces with oil or grease. Then, the problem of bounce will be exceedingly reduced.

4.1.3 Agglomeration

As the aerosol particles collide with each other due to their relative motion, they begin to adhere and form larger particles. This process is called coagulation in general and agglomeration in the case of solid particles. In addition, the solid particle clusters, which are formed via the process, are called agglomerates. There are mainly two coagulation processes for aerosols. One is the thermal coagulation, which is governed by the relative motion between the particles through Brownian motion, is always present and occurs spontaneously. Another is the kinematic coagulation, where the relative motion is caused by external forces such as gravitational, electrical, or aerodynamic forces. These processes decrease the aerosol concentration in proportion to increase the number of the large agglomerates.

Let's start considering with the simplest thermal coagulation of monodisperse spherical particles (d_p)>0.1 μm. According to the calculations through Smoluchowski coagulation[1] and the Fick's first law of diffusion equations, several physical facts on the behavior of the aerosol

---

[1] Smoluchowski coagulation equation is assumed that particles stick with every collision and the particle size varies gradually.

particles could be stated (mathematical details in Hinds 1999). The concentration of the particles in aerosol lowers as the particle size is increased by coagulation. Although very fast coagulation occurs at high aerosol concentrations, the coagulation significantly slows down at low concentration. When the aerosol concentration is less than 10^6 cm^{-3}, the coagulation has an insignificant effect on particle size within a measuring time interval of 5 minutes. The coagulation is negligible in laboratory experiments if the aerosol concentration is less than 10^6 cm^{-3}. Consequently, it is possible to create less coagulation environments by diluting the aerosol to avoid collisions of the particles.

The coagulation of non-spherical particles increases in comparison to spherical particles with the same volume because the non-spherical particles have a larger surface area which is feasible to induce more collisions by Brownian motion. As the particle shape irregularity becomes much more complicated, the coagulation effect will be more significant. According to a theoretical calculation by Zebel (1966), ellipsoidal particles (axial ratio 10:1) have a 35 % higher coagulation coefficient than spherical ones with the same volume.

The thermal coagulation increases if attractive electrical forces between particles act strongly. Aerosol particles, which have opposite charged signs, increase the frequency of collisions. The particles having same charged signs, on the contrary, reduce the frequency of collisions. The overall result does not change remarkably in the coagulation for aerosols with a Boltzmann equilibrium charge distribution. On the other hand, the net coagulation result outstandingly increases with a strong bipolar charge distribution. Charged particles form chainlike agglomerates unlike uncharged particles. If the aerosol particles have a unipolar charge distribution, they repel each other and slow down the coagulation. The mutual repulsion produces electrostatic dispersion or the spreading of the aerosol cloud with deposition on walls. As a result of that, the number of concentration will reduce which accompanies the decrease in the rate of the coagulation.

In polydisperse coagulation, one has to take a range of particle size into consideration. A first polydisperse condition is that only two different sizes of the particles are contained in aerosol (d_1 and $d_2 > 0.1$ μm). Coagulation occurs faster with a combination of different size particles compared to same size ones. Large particles have a wide surface area with slow diffusion whereas small particles have a small absorbing surface area with rapid diffusion. As the ratio of the two particle sizes increases, the effect of the coagulation increases as well. For instance, when 0.01 μm and 1.0 μm particles in diameter coagulate in aerosol, the coagulation takes place 500 times faster than the coagulation with only 1.0 μm particles and 180 times faster than the coagulation with only 0.01 μm particles. Moreover, if a particle collides with a different size particle in aerosol, a new particle size will be formed. For example, let's suppose that a 1.0 μm size particle collides with a 0.1 μm size particle. Thereupon, a new particle, which has a mass 0.1 % larger than the original 1.0 μm particle, is formed. And, the diameter of the new particle becomes 0.03 % larger than the 1.0 μm particle for non-fractal particles. Though the size of the new particle is basically the same as the original 1.0 μm particle, the small size particle (0.1 μm) disappears during the coagulation process because the large particles assimilate the smaller ones.

A complicated polydisperse condition is that every other size of the particles exists in aerosol. It is then necessary to consider the variation of the size distribution and the proportion of particles of a particular size with time. If there is a wide range of size distribution at the initial point, the distribution will become narrower as time goes on. The small particles coagulate with the larger ones vigorously. This occurrence causes a reduction of smaller particle numbers and a gain of larger particle numbers moderately. In consequence, an increase of the average mass diameter and a narrowing of the size distribution take place through this process.

The coagulation of monodisperse aerosols also acts like the polydisperse ones as time goes on. Some particles undergo the coagulation to form larger ones which assimilate the smaller particles. In both the coagulation of monodisperse and polydisperse cases, the aerosols reach a self-preserving size distribution (or a stable size distribution) after some transient period.

The coagulation process can be induced kinematically by other factors than Brownian motion. I refer to four factors which influence the relative motion between the particles here. First, the gravity leads to collisions and coagulation in aerosols since it generates the relative motion of larger and smaller particles. The capture efficiency [2] explains the effect of fluid streamlines that bend around the larger particles pushing the smaller ones out of the way. The capture efficiency decreases to zero if both small and larger particles have the same size since their relative velocity becomes zero.

Second, centrifugal or electrical fields create relative motion between the particles as well. The effects of these situations are much more effective because the relative velocities between the particles are much greater.

Next, airflow brings about gradient or shear coagulation because of flow velocity gradients. If the aerosol particles are flowing in a velocity gradient, they move with different velocities since they position on different streamlines. Even if the particles have exactly the same size, they have different velocities in the velocity gradient. As a result, the particles on a faster streamline catch up the ones on nearby slower streamlines and the collision happens. According to a calculation through the ratio of gradient to thermal coagulation rate at any points, gradient coagulation would exceed thermal coagulation if the particles are larger than 2.5 μm in a flow of 0.06 m^3/hr through a tube 10 mm in diameter. Then turbulent flow creates swirl that induces the relative motion. In this case, the velocity gradient is highly related to a relative motion to give rise to collisions similar to the case of the airflow. After calculation through the ratio of kinematic coagulation to thermal coagulation with a typical velocity of 10 m/s in a ventilation duct having a diameter of 0.2 m, the coagulation via turbulent flow is more important than the thermal coagulation especially for particles larger than 1 μm in diameter. In general, turbulent coagulation can be neglected for small particles (d$\approx$0.1 μm), but is very important for particles larger than 10 μm in diameter (This section is based on Hinds 1999).

4.2 KBr pellet technique

The KBr pellet technique is the classical technique in which a solid sample (e.g. silicate) is mixed with potassium bromide powder (KBr), which has exceedingly high transmission throughout the mid-infrared range (2.5-25 μm), and the mixture is pressed to make a 0.55 mm thick and 13 mm in diameter pellet for use of spectroscopic analysis.

In my experiment, the ratio of a sample and the KBr powder is 1 to 500 in weight. First of all, I measure the weight about 0.0005 g of a sample, afterwards add 0.25 g of KBr powder. The sample mixture is placed in an agate mortar and ground with a pestle thoroughly in order to segregate the particles as minuscule as possible. If I do not mix them rigorously, the measured spectra are not steadied and indicate the different band profiles as shown in Fig. 4.4 where the normalized extinction efficiencies versus the wavelength are plotted for crystalline spinel ($\mathrm{MgAl_2O_4}$) with grinding times of 10 minutes and 1 hour. Though I use

---

[2] The capture efficiency is the ratio of the actual frequency of collisions to the possible frequency of collisions under a condition that if the small size particles are fixed and not thrust aside by the flow around the large size particle.

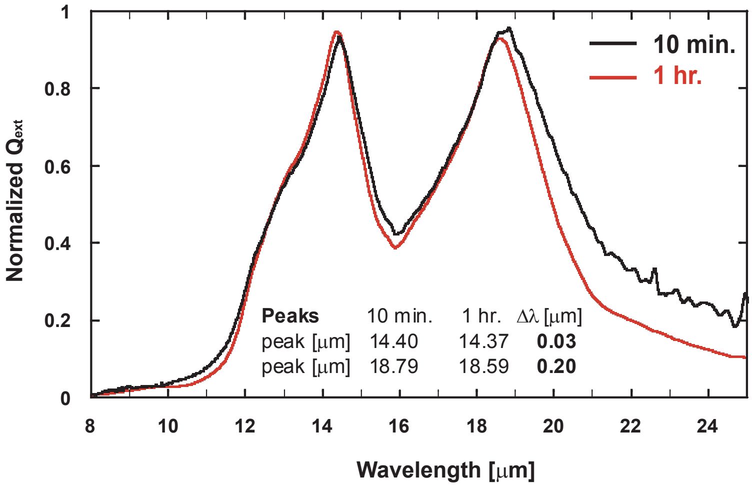

Figure 4.4: Normalized extinction efficiency Q_{ext} vs. wavelength of *crystalline spinel* with two different grinding times.

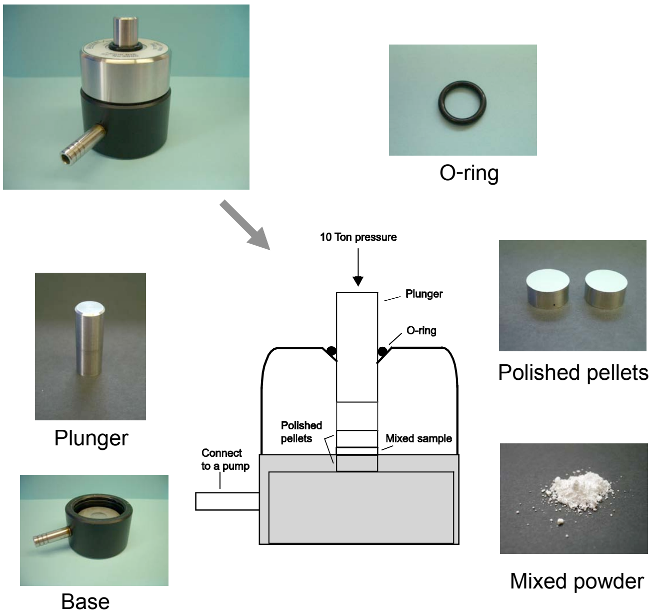

Figure 4.5: The pictures and a diagram of the evacuatable pellet die.

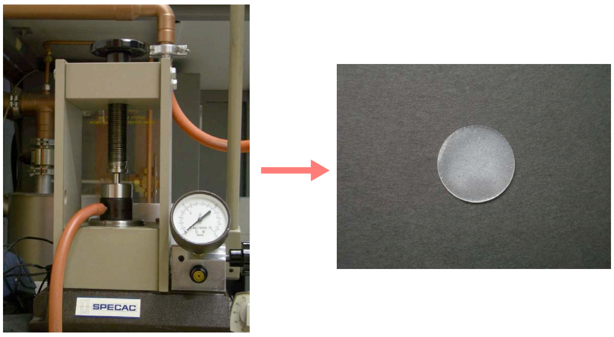

Figure 4.6: The pictures of the laboratory hydraulic press on the left and the finished KBr pellet on the right.

exactly the same sample, the peak positions and the bandwidths are influenced by the time variations. After 1 hour of grinding time, the spectra do not undergo enormous alternations more. However, I also have to be careful about the time because if I take too much time for the grinding, there is a possibility to absorb humidity (water) from air, and a crystalline phase of materials may be damaged by grinding which of course affect the spectra. Consequently, it is necessary to triturate at least 1 hour for producing sufficiently segregated particles in KBr matrix without any damages. Note that I consider that the KBr powder acts as a buffer to avoid the destruction of a sample structure (Koike and Mutschke, private communication).

Second, 0.2 g of the mixture sample is weighed and placed in an evacuatable pellet die (production of Specac) which includes a base with a vacuum attachment, a main body, optically polished stainless steel pellets, a stainless plunger, and an O-ring as shown in Fig. 4.5. At the beginning, I place the small pellet with polished face up in the columnar hole of the main body. After the mixed sample is put into the columnar hole, I tap the die lightly on a flat floor for distributing the mixture uniformly. Again, the other pellet with polished face down is inserted in the hole and using the plunger to press the pellet to the end. The O-ring seal must be placed around the tap of the plunger for making more desirable vacuum condition in the die.

Next, the complete evacuatable pellet die is placed on a laboratory hydraulic press (production of Specac) in Fig. 4.6 (left). I connect a tube from a pump to the die so as to evacuate all air slowly, then apply 10 Ton load to the die for 10 minutes. Thereupon, as shown in Fig. 4.6 (right), the preparation of the KBr pellet is accomplished after it is safely removed from the die and stored in a desiccator in order to avoid absorbing the humidity.

Advantages of the KBr pellet technique are low costs, low sample consumption, and possible to keep the pellets for long time in a desiccator. Conversely, disadvantages are that particles may transform during the grinding procedure; a configuration of particles can hardly be visible whether particles are thoroughly isolated in the KBr matrix or not; there is a risk to cause the powdered sample structure deformation in relation to the high pressurization required for the KBr pellet technique as well.

4.3 Experimental setup for aerosol measurements

Regarding the aerosol measurements, I use a White-type long-path infrared cell (MARS-8L/20V, Gemini Scientific Instr.) of 18 m path length, attached to a Fourier Transformation Infrared Spectrometer (FTIR, Bruker 113v), to measure the extinction of the infrared radiation by the dust particles suspended in an aerosol cloud filling the cell. Multiple reflection of the infrared radiation between two gold mirrors at both ends of the cell enhances the sensitivity of the detection sufficiently to achieve optical depths around unity in the mid-IR bands. An available dust flow generator (Palas RBG 1000), which utilizes a rotating brush to disperse a pressed powder from a dust storage hole into a gas stream, produces the dense aerosol which is led through stainless steel tubes toward the cell. In order to concentrate small-sized particles in the aerosol, I place a two-stage impactor between the dust flow generator and the cell. The first stage retains clusters of particles above a certain size limit whereas the second stage densifies the aerosol up to a concentration of 10^6 particles per cubic centimeter. After filling the cell with the aerosol, I measure the extinction spectra of the suspended particles in the cell. During the spectroscopic analysis, nitrogen (N_2) gas flows continuously from both ends of the cell so as to settle large size particles because a main purpose of this experiment is to measure preferentially the smaller size particles. I extract the particles from the impactor on

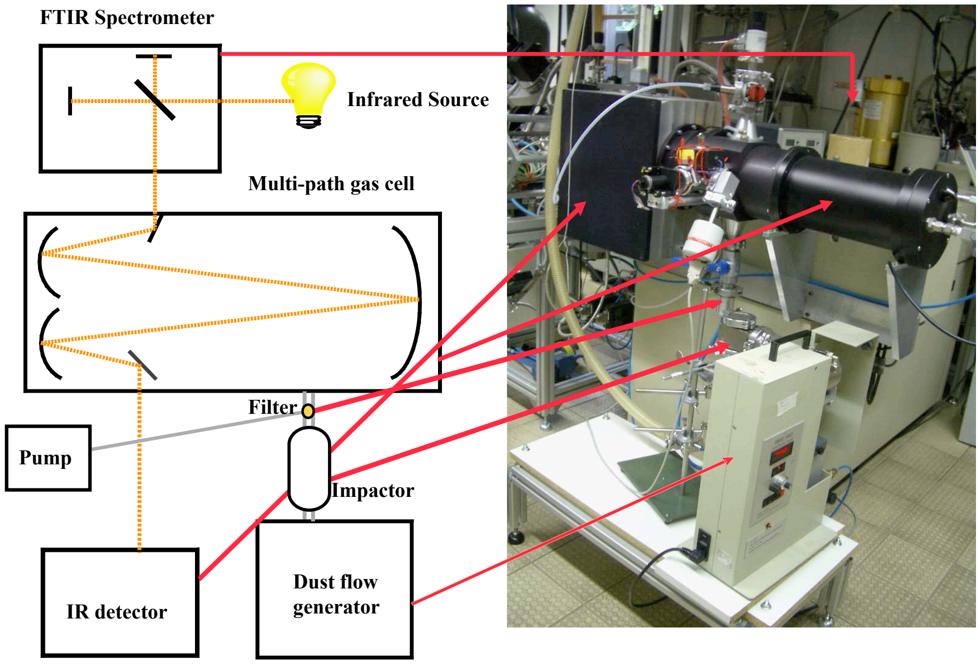

Figure 4.7: A schematic diagram (left) and a photo (right) of an extinction measurement apparatus.

a polyester-membrane filter, which is installed between the outlet of the impactor and the cell externally in order to take photos of the sample by the use of a scanning electron microscope (SEM) for inspection of the particle morphology.

Fig. 4.7 shows the setup of all the apparatuses for the aerosol measurement. The FTIR spectrometer, the dust flow generator, the impactor, and the filtration are major parts of this experiment. In the next subsections, I refer to the functions of these devices in details.

4.3.1 What is the FTIR spectroscopy?

Fourier Transformation Infrared Spectroscopy (FTIR) is an analytical technique to identify substances. As previously mentioned in Sec. 2.5, in general, a substance partly absorbs and passes through IR radiation when the radiation penetrates a substance. Then, absorption and transmission spectra can be detected and represent a fingerprint of the substance along with absorption peaks which are generated by vibrational transitions of atomic bonds. Respective substances are composed of distinctive combinations of atoms; therefore, if there are two different materials (e.g. Mg_2SiO_4 and $MgSiO_3$), it is impossible to obtain exactly same IR spectra even if they belong to a same mineralogical group (silicate). Moreover, the absorption peak sizes of the spectrum directly indicate the amount of substance. Thus, it is possible to identify the different sorts of substances.

In order to measure all of the infrared frequencies at the same time (simultaneously), a Michelson interferometer, which has been utilized widely as the heart of FTIR, is used for encoding a composite signal that contains all of the infrared frequencies present. Basically, the entire signal from a substance is analogue of a chord. The cord is modulated via a frequency-dependent interference and recorded over time. The Fourier transformation signal is similar to that the chord separates into its individual tones, which refer to the spectrum in

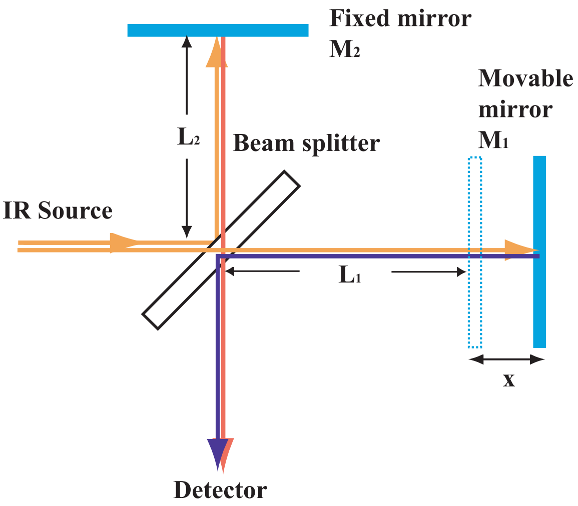

Figure 4.8: Illustration of a Michelson interferometer from Gronholz & Herres (1985).

this case.

The Michelson interferometer makes use of a beam-splitter to divide an incident beam into two beams as shown in Fig. 4.8. The beam-splitter is situated with an orientation angle of 45° relative to the two mirrors. A fixed flat mirror is located at parallel to the incident beam with a distance L_2 from the splitter. Likewise, a movable flat mirror is placed at perpendicular to the beam with a distance (L_1+x) from the splitter. Thus, one half of the beam reflects off the splitter and travels to the fixed mirror M_2; therefore, the total path length of this reflected beam will be $2L_2$. The other half of the beam passes through the beam splitter and reflects off the movable mirror M_1 which precisely moves back and forth along the direction of the incident beam within a distance x. Hence, the total path length of this transmitted beam should be 2(L_1+x). After both beams reflect off the mirrors respectively, they recombine at the beam-splitter. As a result of a phase difference between these two beams, they interfere with each other either constructively or destructively depending on the additional path difference p (p is twice the distance between the basic position of the movable mirror and after the movement of the mirror i.e. p=2x). Maximum detector signal and constructive interference occur when optical retardation of the two partial waves is a multiple of the wavelength

$$p = m * \lambda \qquad (m = 0, 1, 2, ...) \qquad \text{(constructive)} \tag{4.1}$$

Conversely, minimum detector signal and destructive interference take place if p is an odd multiple of $\lambda/2$

$$p = \frac{\lambda}{2}(2m + 1) \qquad (m = 0, 1, 2, ...) \qquad \text{(destructive)} \tag{4.2}$$

Since the path difference between the two beams p varies continuously, a detector can record the intensity I(p) of the recombined IR beams as a function of the movable mirror displacement x, the so-called *interferogram*.

If the IR radiation has the wavenumber $\tilde{\nu}$ (=1/λ), the interferogram I(p), which varies with p, can be expressed as

$$\mathrm{I}(p) = I(\tilde{\nu})(1 + \cos 2\pi\tilde{\nu}p) \tag{4.3}$$

Because an actual signal contains a large number of frequencies (wavenumbers), the total intensity is the summation of all the oscillating intensities which is described by

$$\mathrm{I}(p) = \int_0^\infty I(\tilde{\nu})(1 + \cos 2\pi\tilde{\nu}p)d\tilde{\nu} \tag{4.4}$$

I($\tilde{\nu}$) in Eq. 4.4, which is the intensity difference with regard to wavenumber, will become the spectrum of the sample. In order to obtain the I($\tilde{\nu}$), the *Fourier transformation* is necessary for decoding into individual frequencies.

$$\mathrm{I}(\tilde{\nu}) = 4\int_0^\infty \{I(p) - \frac{1}{2}I(0)\} \cos(2\pi\tilde{\nu}p)dp \tag{4.5}$$

This equation is usually solved by a computer, which is interfaced to the spectrometer after recording all values of I(p) over some numbers of scans[3].

The resolution of FTIR spectrometer can be improved with increasing optical path difference p. Thus, the achievable resolution can be determined by the maximum path length difference of the interferometer as

$$\Delta\tilde{\nu} = \frac{1}{2p_{max}} \tag{4.6}$$

A major advantage of the interferometric technique is that it is possible to measure extremely fast because all frequencies could be measured simultaneously and monitored continuously. On the other hand, the disadvantage is that if noise arises in one part of the radiation from the infrared source, it will be spread in every part of the spectrum in an FTIR system. (Atkins 1994, Gronholz & Herres 1985, see more details of mathematical Fourier transformation technique in e.g. Anderson 1971).

4.3.2 Aerosol generator

The rotating brush generator, Palas RBG-1000 is utilized for dispersing dry and non-cohesive powder. A reason why the generator has been selected for the aerosol experiment is that it is possible to generate a constant aerosol flow during the measurements. Fig. 4.9 shows the photos of the whole view and a main part of the generator as well as illustrations of a front view part (center) and a cross-sectional view of the generator (right). In the first place, before a dry powder is filled in the powder reservoir, the transportation piston must be pulled out to

---

[3] At first, the intensity spectrum (single channel) can be obtained. Absorption spectrum is obtained only after dividing by a reference spectrum.

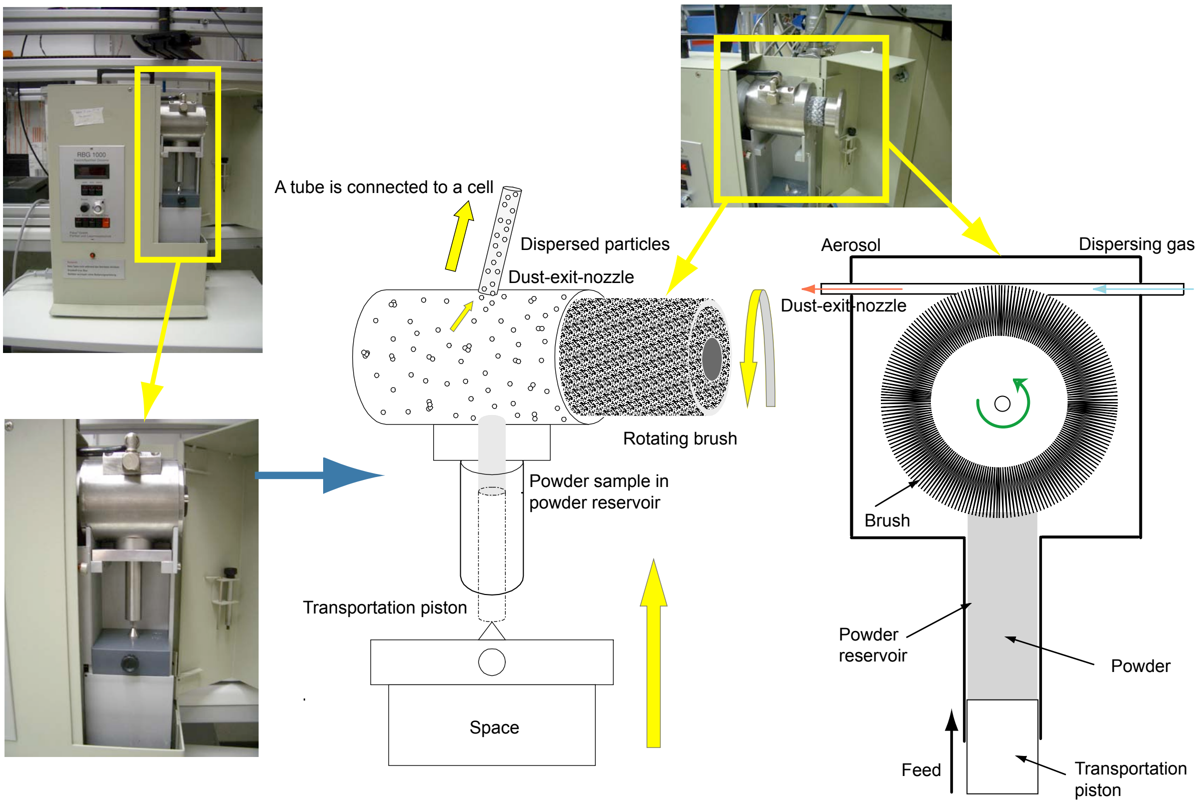

Figure 4.9: Photos of the rotating brush dust flow generator (Palas RBG-1000). Center: a diagram of a front view. Right: a diagram of a cross-sectional view.

make enough vacant space for the appropriate amount of the sample. Next, the sample is filled in the reservoir little by little with use of a scoop. When the sample is filled into the reservoir approximately 1 cm to 1.5 cm high, it needs to be compressed by a tamper. This process has to be repeated until the cylinder is filled to a height of about 2 cm. This compressing force depends on the sort of samples and the cylinder diameter as well. In order to maintain a constant feed rate while using a constant piston feed speed, the compressing process plays a key part in here. If the compressing force is too strong to make the sample extremely dense, the friction will become too strong. Conversely, if the force is too weak, the sample will be more compressed on the way going upwards. This may give rise to the stick-slip-effect which means that due to the static friction, the total feed energy is kept within the mechanism and will be released suddenly because of a hard thrust when the static friction is overcome. This unstable feeding condition causes a pulsating feeding. Finally, once the filling is completed, it is necessary to push the compressed powder sample to the upper surface of the powder reservoir by the use of the transportation piston so as to be able to adjust to the shape of the brush. This is also an opportunity to test the compressing quality while the piston is pushed up. If the piston cannot be moved by hand, the compressing force has been too strong to cause the stick-slip-effect. On the other hand, if the piston can be moved easily, the compressing is too light. In order to retain a constant feed rate and avoid the stick-slip-effect, experience is required for improving the sense of the compressing ability.

After the sample is filled in the powder reservoir properly, it will be installed under the brush. As switching on the generator, the feed speed of the transportation piston is adjusted to 50 millimeter per hour (mm/h). Once Air, Brush, and Feed switches are on, the brush

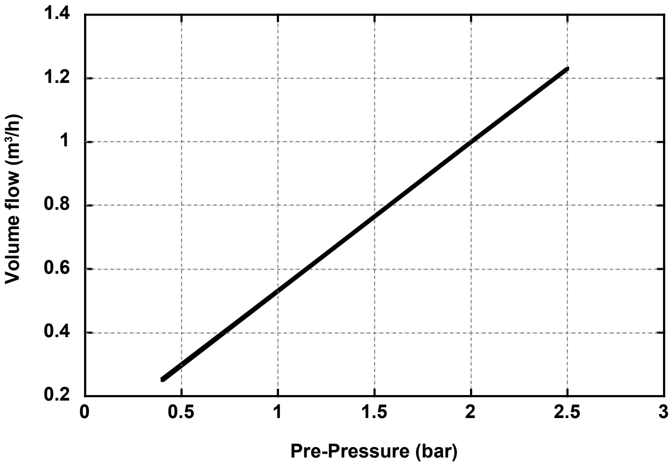

Figure 4.10: The volume flow curve for dosage feed from the operating manual of the solid particle disperser RGB-1000 (Palas).

starts rotating, the N_2 gas flows through the dispersionhead, the compressed powder is moved upward by the transportation piston. Thus, the compressed powder reaches the brushhead to be dispersed. Since there is the gas flow at the upper part of the dispersionhead, the dispersed particles are transported by a high velocity gas stream via the dust-exit-nozzle to the next stage which is an impactor. The shear forces in the gas flow lead to further deagglomeration and dispersion of the particles as they are carried away by the gas flow. Because it is necessary to maintain high gas pressure and higher gas velocity for dispersing the small particles, a volume flow of 1.0 m^3/h and an inlet gas pressure of 2.0 bar are applied for the samples that are in use (Fig. 4.10).

The feed rate with regard to the mass flow (the amount of dust per time: g/h), which is pushed out of the generator, can be determined mathematically. The mass M rate is able to be expressed by

$$\mathrm{M} = \frac{\pi}{4} \cdot \mathrm{d}^2 \cdot \mathrm{v} \cdot \mathrm{q} \tag{4.7}$$

where d is the diameter of the powder reservoir, q is the homogeneous compressed density of powder inside the reservoir, and v is the feed velocity of the piston. The mass concentration per gas volume $\mathrm{M_c}$ inside the dust-exit-nozzle can be calculated as well.

$$\mathrm{M_c} = \frac{\mathrm{M}}{\mathrm{V}} \tag{4.8}$$

where V is the dispersion gas volume flow rate.

Smaller sized particles need higher gas velocity to be dispersed because the shear force in the turbulent gas-stream disperse the powder and separate agglomerates in the aerosol. Consequently, a maximum amount of dispersion gas and low powder feed can generate the best dispersion conditions. In other words, a high velocity gas-stream is commonly used for dispersing the particles.

The particles will be electrostatically charged during the dispersion. The level of charge strongly depends on properties of the materials and conditions how they separate from each other such as powder, dispersing gas, and brush. It is possible to discharge the particles by

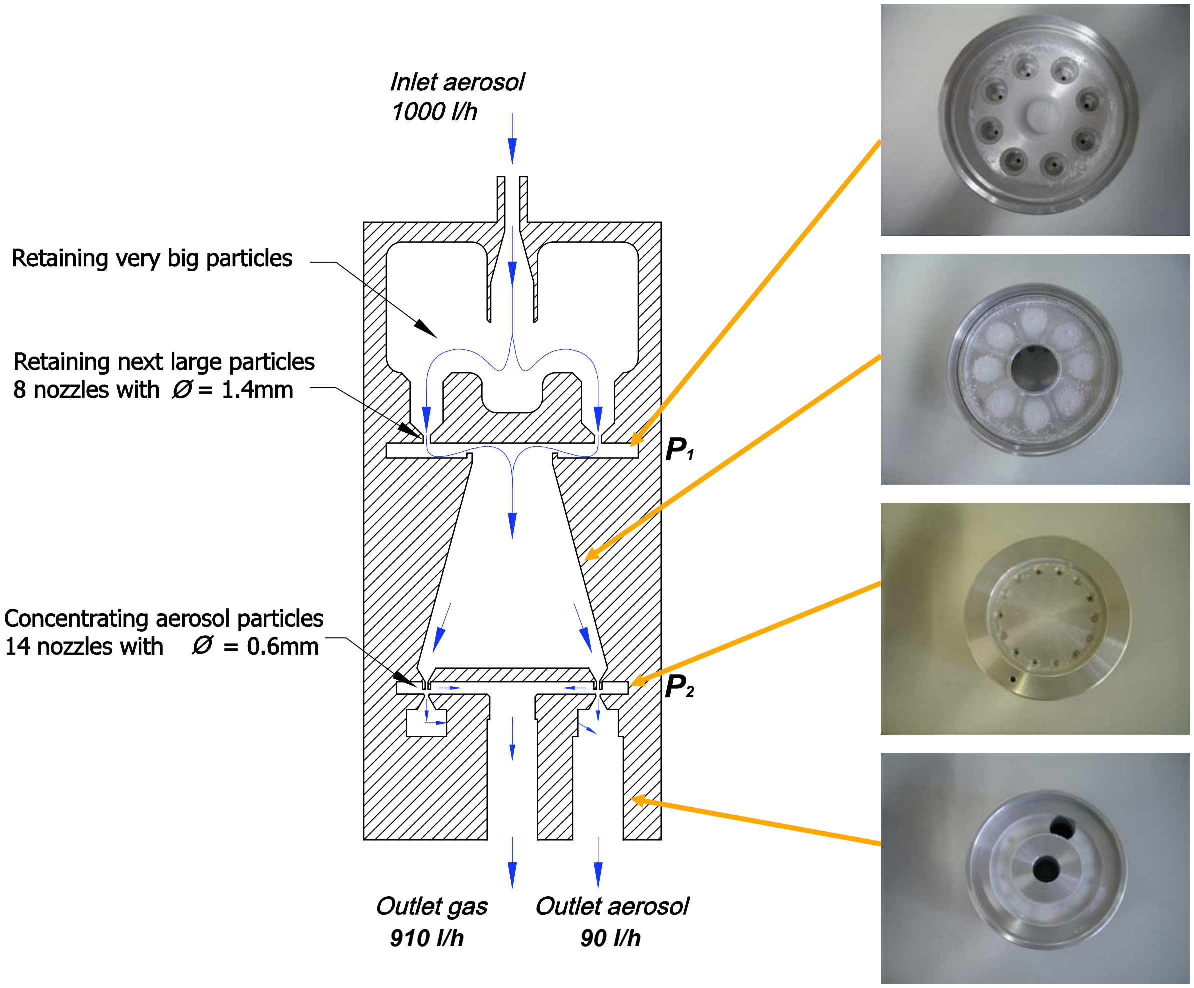

Figure 4.11: Left panel: Cross-sectional diagram of a two stage impactor. Right panel: Photos of each part of the impactor, a first impaction plate with 8 nozzles, a plate between the first and the second stages, a second impaction plate with 14 nozzles, and a last part of the impactor from the top.

mixing the aerosol with a bipolarly ionized gas, for example.

Preparation and selection of the dry powder samples are important factors to enhance the dispersibility of a powder since it is conditional on the material itself, particle size and shape, and moisture content. For instance, hydrophilic materials (e.g. quartz or limestone) are more difficult to disperse than hydrophobic materials (e.g. talc). As the particle size increases, dispersibility increases rapidly as well. Electrostatic forces between particles become stronger with low moisture content; therefore, exceedingly dry air or gas (relative humidity < 5 %) would induce strong electrostatic forces and decrease the dispersibility of the particles (This subsection is based on Palas GmbH 2002).

4.3.3 Impactor

A two stage impactor is installed between the dust flow generator and the cell so as to transport only the small size aerosol particles to the cell for spectroscopic analysis. The originally manufactured impactor has been applied for the aerosol experiment.

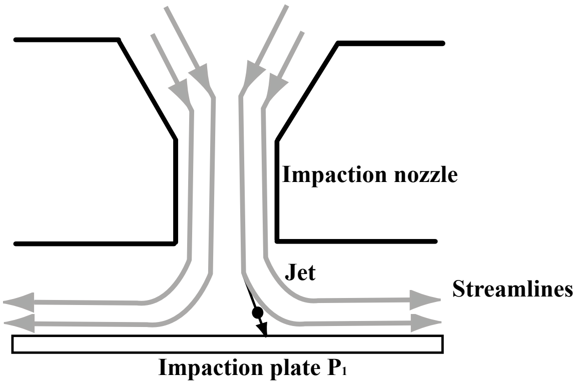

Figure 4.12: Cross-sectional diagram of the impactor with gas streamlines from Hinds (1999).

After the aerosol is produced by the dust flow generator, a large amount of particles are transported to the impactor by the gas. Once the aerosol enters the impactor, it passes through small nozzles and goes at high velocity in the direction of a first flat impaction plate P_1 in Fig. 4.11. In front of this impaction plate P_1, the streamlines make a right-angled turn as shown in Fig. 4.12. If inertia of the aerosol particles exceed a certain value, they are not able to remain in the streamline and directly hit the impaction plate P_1. The smaller aerosol particles can remain in the gas-stream and pass through the 8 nozzles with 1.4 mm in diameter at the impaction plate P_1 without striking on the plate. Hence, it is possible to separate the aerosol particles into two size ranges. The particles whose size are larger than a certain aerodynamic size are taken away from the gas-stream and remain on the impaction plate P_1. Afterwards, the particles, which successfully pass through the impaction plate P_1, reach to a second flat impaction plate P_2. Again, the particles are divided into two size ranges as they pass through the 14 nozzles with 0.6 mm in diameter at P_2; therefore, only small size particles are concentrated there. As a result of that, 91 % of aerosol is unused and goes to exterior, and only the smaller ones can be successfully transported to a next stage which is a black anodized aluminum gas cell.

4.3.4 Cell

A black anodized aluminum gas cell (Gemini Scientific Instruments) has been mounted between the impactor and the FTIR spectrometer. The cell is composed several important parts which determine high quality of optical performance. The fitting endplate is placed on the very end of the cell as shown in Fig. 4.13 (bottom). An objective tray holds a set of objective mirrors of two pieces in front of the fitting end plate. The objective mirrors determines the cell pathlength. The body of a cylindrical cell, which is mounted between the objective mirrors and the field mirror, consists of a thick heavy metal pipe in order to withstand high vacuum operation. The diameter of the cell is about 13.6 cm and the total length of the cell is approximately 55.7 cm. The aerosol through the impactor enters the cylindrical cell from the path which is located under the cell. One side of the cell, a round laser window 3.5 cm in diameter is installed, and a laser is placed in front of the window. A scattering light detector is mounted the opposite side of the window; therefore, when the laser beam strikes the aerosol particles in the cell, scattering light is emitted by these particles and detected by the scattering

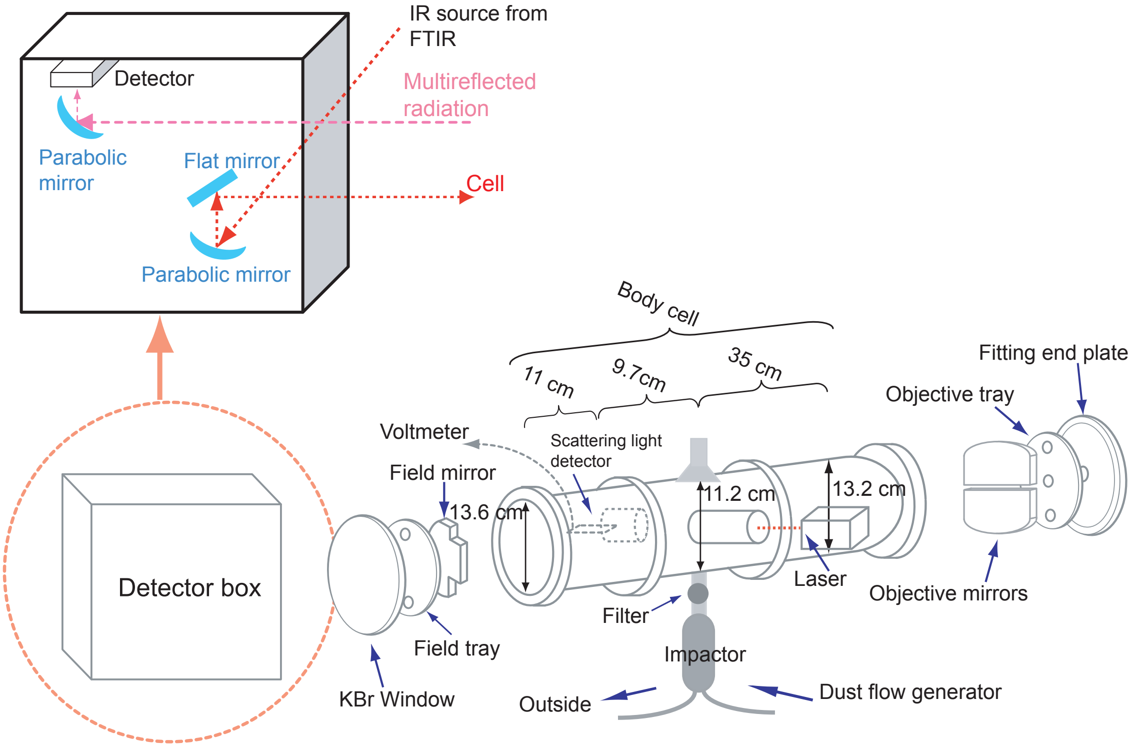

Figure 4.13: Diagrams of the detector box which contains two parabolic mirrors, a flat mirror, and a FTIR detector (upper panel) and the gas cell (bottom panel).

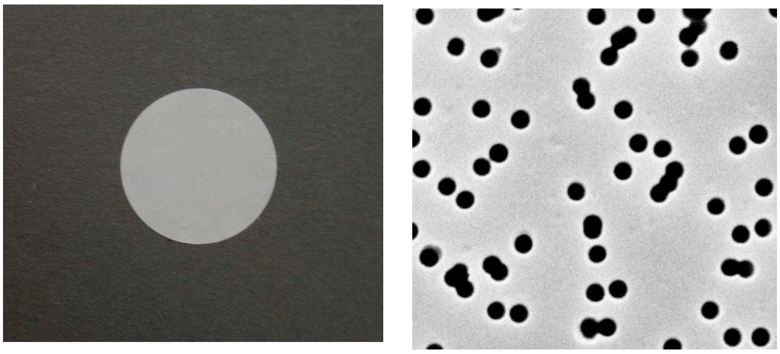

Figure 4.14: Left panel: The polyester capillary pore membrane filter with 13 mm in diameter. Right panel: A SEM picture of the polyester capillary pore membrane with a magnification power of 4000.

light detector. Since the scattering light detector is connected to a voltmeter, it is possible to perceive whether the detectable amount of aerosol is reached the cell or not. The cylindrical cell is covered with the field mirror, the field tray, and the KBr window plate that is attached to the detector box.

The incident IR radiation enters the detector box from the FTIR spectrometer in the first place as shown in Fig. 4.13 (upper panel). Then, the radiation hits a parabolic mirror. The direction of the IR radiation is varied perpendicular to the incident angle due to reflection. Thereupon, a flat mirror reflects the IR radiation, and the angle of the radiation is altered parallel to the cylindrical cell; therefore, the IR radiation can be eventually entered in the cell. Once the radiation comes into the cell, it is reflected by both the objective and the field mirrors back and forth 16 times (multiple reflection). After the multiple reflection, the light goes back in the detector box and is reflected by another parabolic mirror in order to reach the FTIR detector completely. In this experiment, the path length will become around 18 m so as to enhance the sensitivity of the detection sufficiently to achieve optical depths around unity in the 10 μm band.

4.3.5 Filtration

I use an ordinary filtration method in order to capture the aerosol particles for sampling. Polyester capillary pore membrane filters have been utilized for sample collection. This filters have uniform cylindrical holes that are distributed randomly on the filter and are approximately perpendicular to the filter surface. The used filters are 13 mm in diameter as shown in Fig. 4.14 (left). Since my experimental samples are mostly less than 1 μm in diameter, I select two filters with different pore diameters (d=0.1 and 0.4 μm) as shown in Fig. 4.14 (right). A disadvantage of this filter is that it may not be greatly efficient for the particles smaller than the pore size because the particles pass through the pores. On the other hand, an advantage is that the filters are very capable for the use of a scanning electron microscope (SEM) to analyze the physical properties of the particles due to their smooth surfaces.

4.4 Samples

16 samples of 7 compositions (SiO_2, Mg_2SiO_4, $MgSiO_3$, $Mg_{1.9}Fe_{0.1}SiO_4$, Al_2O_3, $MgAl_2O_4$, TiO_2) have been investigated. Most of the crystalline samples are commercial products; however, some of the products such as the amorphous Mg_2SiO_4 and the crystalline forsterite as well as the amorphous $MgSiO_3$ and the crystalline enstatite, I made use of original samples which were produced in the laboratory of the AIU by the sol-gel technique (Jäger et al. 2003) (see Sec. 4.4.3) and glass melting (Dorschner et al. 1995) (see Sec. 4.4.2). Table 4.1 gives a list of the samples used in the entire experiments, together with their properties. TEM images of all samples are shown in Fig. 4.15 to give an impression of individual particle shapes. The samples have been subjected to a sedimentation process (sed. in the Table) in a solvent (acetone), which allowed to obtain a size fraction less than 1.0 μm in diameter (see more details in Sec. 4.4.1).

Note that amorphous SiO_2 (d=1.0 μm) has been annealed in an oven with the temperature 1450°C for 1 hour to produce the crystalline phase.

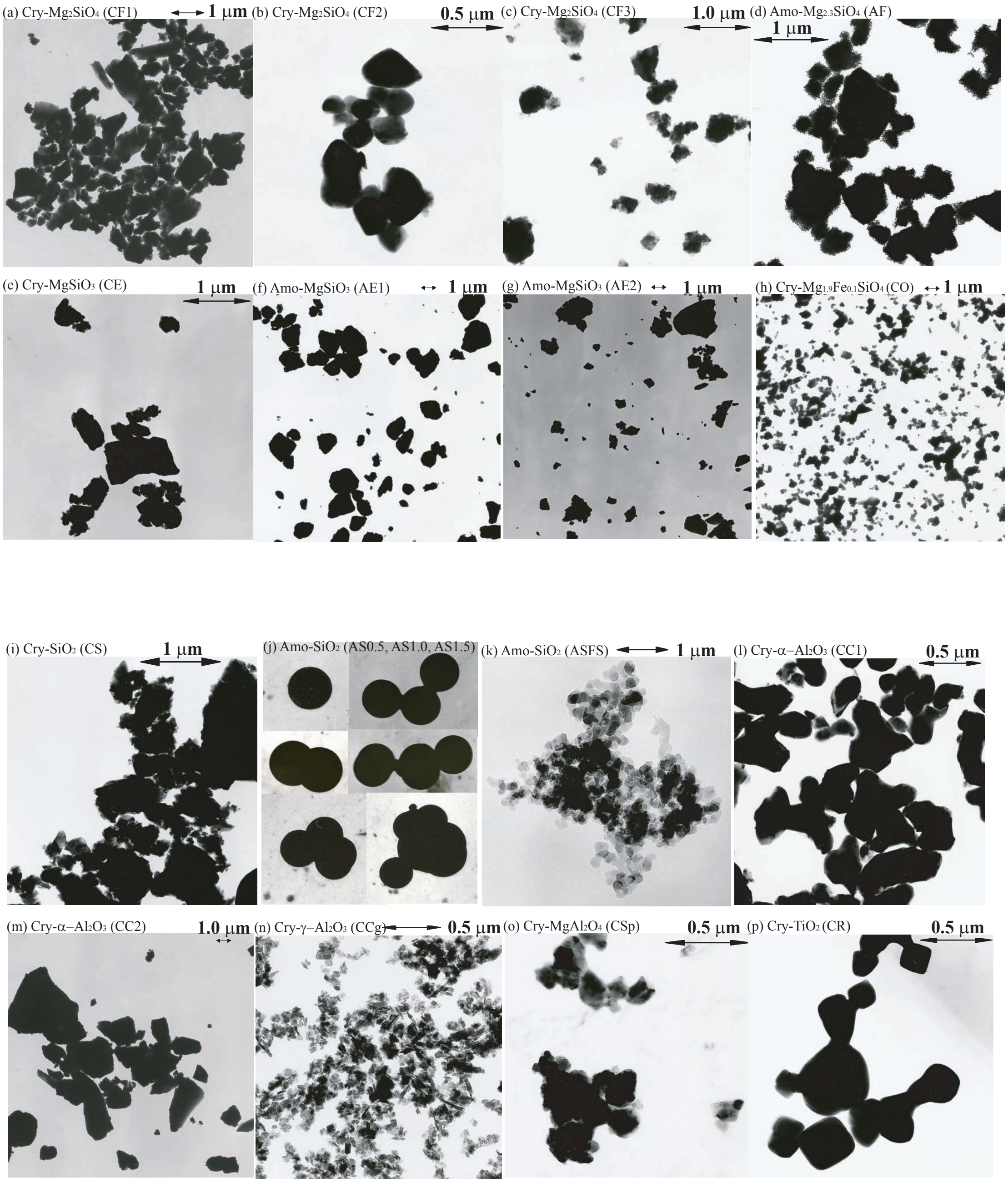

Figure 4.15: TEM images of all samples. (a) Irregular shaped crystalline forsterite (Mg_2SiO_4; CC1). (b) Ellipsoid shaped crystalline forsterite (CC2). (c) Irregular shaped crystalline forsterite (CC3). (d) Irregular shaped amorphous $Mg_{2.3}SiO_4$ (AF). (e) Irregular shaped crystalline enstatite ($MgSiO_3$; CE). (f) Irregular shaped amorphous $MgSiO_3$ (AE1). (g) Irregular shaped amorphous $MgSiO_3$ (AE2). (h) Irregular shaped crystalline olivine ($Mg_{1.9}Fe_{0.1}SiO_4$; CO). (i) Irregular shaped crystalline silica (SiO_2; CS). (j) Spherical shaped amorphous SiO_2 (AS0.5, AS1.0, AS1.5). (k) Irregular shaped amorphous SiO_2 (ASFS). (l) Irregular shaped crystalline α-corundum (Al_2O_3; CC1). (m) Irregular shaped crystalline α-corundum (Al_2O_3; CC2). (n) Irregular shaped crystalline γ-corundum (Al_2O_3; CCg). (o) Irregular shaped crystalline spinel ($MgAl_2O_4$; CSp). (p) Irregular shaped crystalline rutile (TiO_2; CR).

Table 4.1: Properties of the samples.

Classification	Chemical formula	Product Info.	Abbrev.	Preparation	Size (μm)	Shape	Density (g/cm^3)	Melting point (°C)
Crystalline	SiO_2	Micromod	CS	milling	d<1.0‡	irregular	2.635-2.66	1610
Amorphous	SiO_2	Micromod	AS0.5	original	d=0.5	sphere		
Amorphous	SiO_2	Micromod	AS1.0	original	d=1.0	sphere		
Amorphous	SiO_2	Micromod	AS1.5	original	d=1.5	sphere		
Amorphous	SiO_2	Fisher Scientific	ASFS	original	d=10-50 nm	irregular		
Crystalline	Mg_2SiO_4	Alfa Aesar Johnson	CF1	sed.	d<1.0	irregular	3.21	1910
Crystalline	Mg_2SiO_4	Marusu Yuuyaku	CF2	original	d≈0.2	ellipsoids	3.21	1910
Crystalline	Mg_2SiO_4	sol-gel process	CF3	milling & sed.	d<1.0	irregular		
Amorphous	$Mg_{2.3}SiO_4$	sol-gel process	AF	milling & sed.	d<1.0	irregular		
Crystalline	$MgSiO_3$	melting	CE	milling & sed.	d<1.0	irregular	3.192	1557
Amorphous	$MgSiO_3$	melting/quenching	AE1	milling & sed.	d<1.0	irregular		
Amorphous	$MgSiO_3$	sol-gel process	AE2	milling & sed.	d<1.0‡	irregular		
Crystalline	$Mg_{1.9}Fe_{0.1}SiO_4$	natural (San Carlos)	CO	milling	d<1.0	irregular	3.27-4.20†	1760*
Crystalline	α-Al_2O_3	Alfa Aesar Johnson	CC1	original	d=0.3-0.5	irregular	3.97	2015±15
Crystalline	α-Al_2O_3	Glasschemie Jena	CC2	original	d<1.0‡	irregular	3.97	2015±15
Crystalline	γ-Al_2O_3	Alfa Aesar Johnson	CCg	original	d≈0.1-0.3	irregular	3.5-3.9	
Crystalline	$MgAl_2O_4$	Alfa Aesar Johnson	CSp	original	d<1.0	irregular	3.21	1910
Crystalline	TiO_2	Aldrich	CR	original	d<1.0	irregular	4.26	1830-1850

† The density strongly depends on the iron content. If the the olivine has a high iron content, the density becomes higher.

‡ Samples contain large clumps (d>1.0 μm) as well.

* The melting point depends on the iron content as well. In this case, an iron content of 8 % is considered. If the olivine has high iron contesnt, the melting point drops (e.g. a melting point of 1890 °C with Mg_2SiO_4, but 1205 °C with Fe_2SiO_4.)

"sed." denotes sedimentation.

The values of density and the melting points are quoted by CRC Handbook of Chemistry and Physics 71st ed. except for the crystalline olivine (http://www.a-m.de/englisch/lexikon/olivin.htm by Rudolph S.)

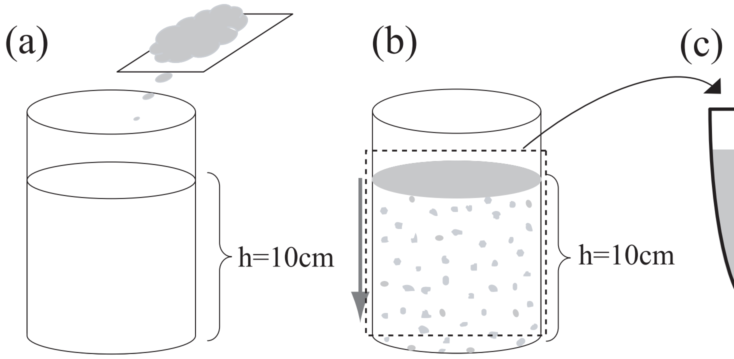

Figure 4.16: Representations of sedimentation process. (a) A solvent (acetone) is poured into a beaker with a height about 10 cm and a powdered sample which contains different size particles put onto the surface of the liquid. (b) At first, all powder fragments are floating on the surface of the acetone. As time passes, the larger fragments start to go down to the bottom of the beaker. (c) After the estimated time, the liquid containing only small particles has to be transferred into a tube for a centrifuge. (d) A centrifuge with 4500 rpm is utilized for 10 minutes in order to separate the solvent and the grains.

4.4.1 Sedimentation

Sedimentation in acetone (CH_3COCH_3), which is based on the Stoke's law, is utilized in order to concentrate small size grain fractions that are less than 1 μm. The density of the acetone (0.784 g/cm^3 at 25 °C; http://www.simetric.co.uk/si_liquids.htm) is lower than that of water and the viscosity of the acetone (0.306 mPa·s at 25 °C; Lide 1991) is lower than that of water as well. Therefore, the particles are well accelerated to settle down to the bottom of the solution container (e.g. beaker) as shown in Fig. 4.16. At that time, larger particles settle down faster than smaller ones. It is possible to calculate the settling velocity and the estimated time for which specific size particles will settle down on the bottom of the container via the Stoke's law.

$$\mathrm{V} = \frac{\mathrm{d}^2 \cdot (\mathrm{D}_1 - \mathrm{D}_2) \cdot \mathrm{g}}{18 \cdot \eta} \tag{4.9}$$

where d is the particle diameter, D_1 is the density of the particle, D_2 is the density of the solvent, g is the gravity, and η is the viscosity of the solvent. Since V=h · t, Eq. 4.9 can be rewritten as

$$\mathrm{t(s)} = \frac{18 \cdot \eta \cdot \mathrm{h}}{\mathrm{d}^2 \cdot (\mathrm{D}_1 - \mathrm{D}_2) \cdot \mathrm{g}} \tag{4.10}$$

where h is the height of the solvent in the beaker. For instance, if the crystalline forsterite particle diameter is approximately 1 μm, the solvent is the acetone at room temperature (26 °C, η=0.306 mPa·s), and the height of the solvent is 10 cm, the sedimentation time will be

$$\mathrm{t} = \frac{18 \cdot 0.00306\ \mathrm{g/cm \cdot s} \cdot 10\ \mathrm{cm}}{(0.0001\ \mathrm{cm})^2 \cdot (3.21\ \mathrm{g/cm^3} - 0.785\ \mathrm{g/cm^3}) \cdot 9.81 * 10^2\ \mathrm{cm/s^2}} \approx 6\mathrm{hrs}43\mathrm{min}. \tag{4.11}$$

Consequently, under this condition, it is necessary to wait about 7 hours to separate the particle size fractions less than 1 μm. This process has been used for the crystalline forsterite,

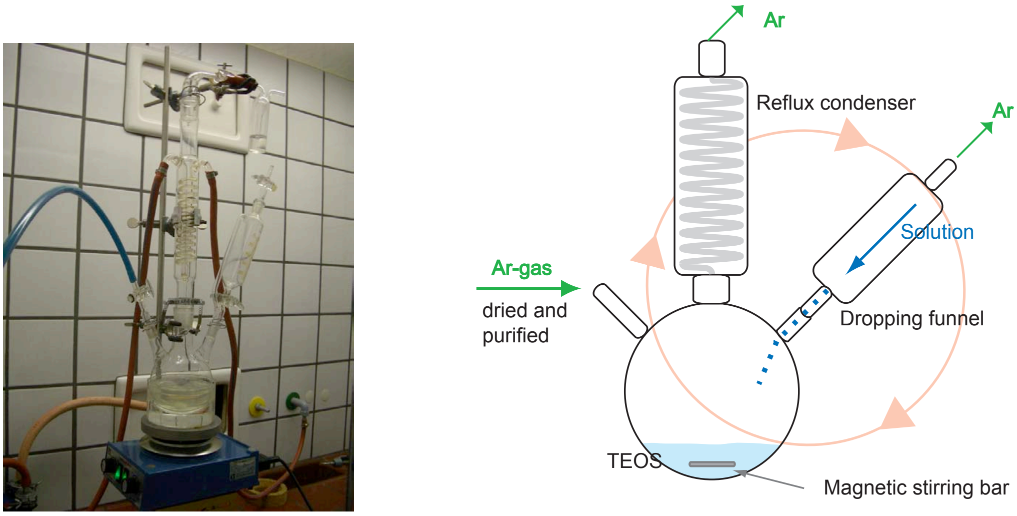

Figure 4.17: The sol-gel sample preparation for amorphous $MgSiO_3$. Left panel: A mixing process for the four solutions such as TEOS, magnesium methylate, H_2O in methanol, and H_2O_2 in methanol by making use of a diagonal coil condenser. Right panel: an illustration of the sol-gel process of the mixing method.

amorphous $Mg_{2.3}SiO_4$, crystalline enstatite, and amorphous $MgSiO_3$. After the sedimentation is completed, the small size sample in acetone is transferred into a tube for a centrifuge, and the tube is placed in the centrifuge (Labofuge A, Heraeus Sepatech GmbH) with 4500 rpm for 10 minutes for separating the solvent and the small size particles. Finally, the desired particles are placed in an oven with a temperature of 105 °C for 1 hour to evaporate all the moisture content (acetone) (Born, private communication).

4.4.2 Melting

The symbolic formula of pyroxene is $Mg_xFe_{1-x}SiO_3$. These subscripts vary with amount of mixtures to produce different types of silicate glasses via quenching melts. For producing the glass $MgSiO_3$, 40.14 % (mass %) of MgO and 59.86 % (mass %) of SiO_2 are mixed thoroughly. The mixture is transferred into a platinum crucible and slowly heated up in an oven up to a temperature 1917 K for one hour. Rapid cooling is necessary to form amorphous silicate (see more details in Sec. 3.1). The mixure is vitrified by pouring it through a rotating copper roller with cooling rate of about 10^3 Ks^{-1}. Thin glass splats with thickness around 100 μm are formed. The glassy $MgSiO_3$ sample is crushed to obtain small pieces and milled in an agate mortar, and if it is necessary to collect a particular particle size such as $d<1$ μm, the sedimentation process is applied (see more details in Dorschner et al. 1995; Jag̈er, private communication).

4.4.3 Sol-gel processing

A colloidal suspension of solid particles in a liquid is a so-called ”sol” (Note: a colloidal suspension of solid particles in a gas is called an ”aerosol”). A colloid has a dispersed phase with very small size particles (≈1-1000 nm; but larger than molecules) which neglect gravitational forces; therefore, interactions are controlled by van der Waals attraction and surface charges. Since the inertia of the dispersed phase is small enough to lead to Brownian motion, which is a random movement due to momentum, is provided by molecular collisions of the suspending medium, the particles are actively moving in a liquid. A "gel" is that in general a colloidal suspension of solid particles loses the motion, in consequence, the particles are gathered and congealed like jelly. "Sol-gel processing" is a chemical technique to obtain an oxide by the use of a metal alkoxide to give rise to a hydrolysis and a condensation reactions. As a result of these reactions, the sol loses the liquidity and becomes gel which would be heated up and produced an oxide. Generally, a sol is made up of oxide (e.g. silicate) which has been used as the precursors (starting compounds). Especially, tetraethyl orthosilicate (TEOS; $Si(OC_2H_5)_4$) is widely utilized as the precursor metal alkoxide. Metal alkoxides react easily with water which is the so-called hydrolysis reaction resulting a hydroxyl ion which is attached to the metal atom. The reaction can be written in chemical reaction formulas as follows:

$$\begin{aligned} \mathrm{Si(OR)_4 + H_2O} &\rightleftharpoons \mathrm{HO\text{-}Si(OR)_3 + ROH} \\ \mathrm{Si(OR)_4 + 4H_2O} &\rightleftharpoons \mathrm{Si(OH)_4 + 4ROH} \end{aligned}$$

where R denotes a ligand (so if R is an alkyl (e.g. $\bullet CH_3$ (methyl) or $\bullet CH_2CH_3$ (ethyl)). ROH represents an alcohol, - here indicates a chemical bond. It is possible to complete the hydrolysis reaction which depends on the amount of water and catalyst present. Then, all of the OR groups can be replaced by OH as in the second chemical equation. However, if the metal is partially hydrolyzed, $Si(OH)_4$ will be $Si(OR)_{4-n}(OH)_n$.

A condensation reaction occurs with two partially hydolysed molecules. The reactions are as follows:

$$\begin{aligned} \mathrm{(OR)_3Si\text{-}OH + HO\text{-}Si(OR)_3} &\longrightarrow \mathrm{(OR)_3Si\text{-}O\text{-}Si(OR)_3 + H_2O} \\ \mathrm{(OR)_3Si\text{-}OR + HO\text{-}Si(OR)_3} &\longrightarrow \mathrm{(OR)_3Si\text{-}O\text{-}Si(OR)_3 + ROH} \end{aligned}$$

The condensation releases small molecules such as water or alcohol by definition. Hydrolysis and condensation reactions are able to continue to form larger silicon containing polymers (see more details in Brinker and Scherer 1990).

Amorphous $MgSiO_3$ sol-gel sample will be produced by the sol-gel reaction of magnesium methylate $Mg(OCH_3)_2$ and tetraethoxysiloxane (TEOS) which can be caused by an promotion of H_2O_2 (Burlitch et al. 1991; Agladze et al. 1996; Jäger et al. 2003). The chemical reaction could be written as follows:

$$\begin{aligned} \mathrm{(C_2H_5\text{-}O)_4Si + Mg(OCH_3)_2 + H_2O_2 + H_2O} + n\mathrm{CH_3OH} &\longrightarrow \\ \mathrm{MgSiO_3 + (n{+}2)CH_3OH + 4C_2H_5OH + H_2O} & \end{aligned}$$

A first step to produce the amorphous $MgSiO_3$ sol-gel sample is that TEOS is placed in a three-necked flask as shown in Fig. 4.17. Magnesium methylate $Mg(OCH_3)_2$ solute in

Figure 4.18: The preparation of the sol-gel sample for amorphous $MgSiO_3$. (a) A set up for the distillation by using a rotary evaporation flask and a diagonal coil condenser to produce the powder sample from the sol-gel solution. (b) After approximately 3 hours of the rotational time, the sample is still in gel state. (c) It becomes the whitish powder after 6 hours of the rotational time.

methanol (CH_3OH) is added in dropwise very slowly (approximately 100 mL methylate and methanol mixture takes 3 hours). During the dropping of methylate, the whole mixture (methylate/methanol and TEOS) is stirred thoroughly. After the methylate/metanol mixture is completely added and stirred, 30 % H_2O_2 in 50 mL methanol solution is added in dropwise steadily about 3 hours. Thereafter, likewise, H_2O in 50 mL methanol (bidest water) is added in dropwise at a slow pace around 3 hours as well. During these dropping processes, the mixture in the flask is always stirred thoroughly with a help of a magnetic stirring bar in the bottom of the flask in Fig. 4.17 (right panel). After the four solutions are completely mixed, again the complete mixture is stirred with adding heat and reflux for 10 hours. Afterwards, the mixture is cooled down to a room temperature, then it transforms into a very lax gel. Up to here, a purified Ar-gas is required to utilize inside of the entire chemical devices during the whole processes mentioned above in order to avoid the precipitation of insoluble $Mg(OH)(OCH_3)$. Once the mixture transformes into the gel, it is possible to handle it in air. Since the synthesize gel contains some different kinds of solvents from original solutions such as methanol, ethanol, and water, it is necessary to remove them by the use of rotary evaporator for distillation in Fig. 4.18. During this distillation process, the gel is getting firm at first (Fig. 4.18 (b)). After 6 hours of rotation, the gel sample becomes powder completely (Fig. 4.18 (c)). Then, the powdered sample is place in an oven with an oxygen (O_2-gas) flow for annealing so as to densify the structure of the magnesium silicate and remove the residues of organic, especially, carbon. For amorphous magnesium silicates need up to a temperature of 500-600 °C (depend on a sort) whereas the annealing temperature up to 1000 °C or more is necessitated for crystalline silicates.

It is possible to determine the compositions of the completed magnesium silicate sol-gel sample by using the electron dispersive X-ray (EDX) analysis (Jäger, private communication).

Chapter 5

Extinction Efficiency of Agglomerate Dust Grains

Seven grain species with 18 different dust samples are utilized for the extinction efficiency measurements through the aerosol technique in the mid-IR region between 8 and 25 μm in wavelength while the solid state (amorphous or crystalline) and the morphological effects are taken into account. The measured profiles are compared with calculations for some cluster shapes applying three different theoretical approaches (Mie, T-matrix, and DDA).

5.1 Amorphous and Crystalline Silica (SiO_2)

The morphological effects on the 9.0 μm extinction band for amorphous SiO_2 monosphere particles which are 0.5, 1.0, and 1.5 μm in diameter (AS0.5, AS1.0, and AS1.5), and irregular shaped nano-sized amorphous particles (ASFS), together with irregular shaped crystalline silica particles (CS) have been investigated. The effects are described in three sections: environment (matrix), size and shape, and agglomeration of the particles. Furthermore, I include Sec. 5.1.4, the difference in the spectra of amorphous and crystalline silica.

5.1.1 Matrix effect in silica

The KBr pellet technique has been experimentally used in infrared spectroscopy (e.g. Koike & Hasegawa 1987; Jäger et al. 1994; Begemann et al. 1997; Chihara et al. 2002). There remains a doubt whether an environmental effect actually occurs or not once a sample is embedded in a different medium (Papoular et al. 1998; Henning & Mutschke 2000; Speck et al. 2000; Clément et al. 2003) . If this happens, how much does the medium influence the band profiles? First of all, I examine the matrix effects through the aerosol experiments and the KBr pellet technique with the three different particle sizes.

The results of the aerosol (Aero) and KBr pellet spectroscopy measurements are shown in Fig. 5.1, where the normalized extinction efficiency is plotted versus the wavelength. Since the aerosol measurements are not quantitative, I use the normalization for the comparison. The aerosol spectroscopy reveals considerably different band positions and full width at half maximum (FWHM) compared to the KBr pellet measurements. The differences between the peak positions are approximately 0.1 μm for the three particle sizes (Fig. 5.1, left). In addition, broader FWHM is obtained with the KBr pellet technique compared to the aerosol

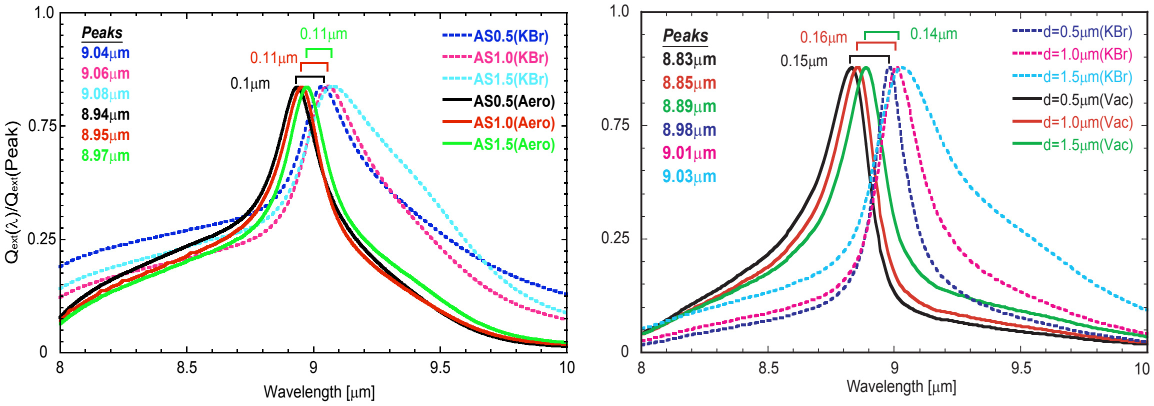

Figure 5.1: Left panel: Normalized extinction efficiency (Q_{ext}) vs. wavelength of amorphous SiO_2 particles (AS0.5, AS1.0 and AS1.5) via the aerosol (Aero) and KBr pellet (KBr) techniques. Right panel: Normalized extinction efficiency (Q_{ext}) vs. wavelength of amorphous SiO_2 particles (d=0.5, 1.0, and 1.5 μm) through the Mie calculations with two different environments: vacuum and KBr media.

experiment. I consider that the powdered SiO_2 sample in the KBr pellet remains as large aggregates, and/or this may also be just an effect of the KBr environment which produces the broader band. Fig. 5.1 (right) shows the comparison between SiO_2 in vacuum and KBr media through the Mie calculations[1]. Under these conditions (the particle diameters are 0.5, 1.0, and 1.5 μm and the wavelength range is between 8 and 10 μm), the Rayleigh limit is valid (see Sec. 2.7.2); therefore, the size effect does not arise in the calculations. The peak position shift between the vacuum and KBr media are obviously appeared through the Mie calculations which signifies that the shift is caused by the effect of KBr environment rather than the size effect.

5.1.2 Size, material, and shape effects

In comparison with the three different particle sizes in the aerosol measurements, the peak position difference of the AS0.5 and AS1.5 samples is merely 0.03 μm, a factor of three and the Rayleigh limit is not strictly valid in the particle size. As the particle size increases, the peak position shifts to longer wavelengths in general. Likewise, there are no manifest differences in the bandwidth among them because larger size particles compose smaller clusters (Sec. 4.1.2).

I also use exactly same size samples, but different manufacturers (produced by Lancaster, d=0.5 and 1.5 μm) in this experiment. The peak position shift of these different manufactured SiO_2 samples never explains the difference between the experimental and theoretical peak positions. Therefore, I have to assume that the optical constants used do not fully reflect the true optical properties of the SiO_2 materials. It is known that some of the products have a lower density of 2.0 g cm^{-3} compared to bulk SiO_2. In order to check the relevance of this fact for the peak position differences, I take a porosity of the material into account by applying the effective medium theory (EMT). In the EMT, effective optical properties of inhomogeneous particles are obtained by using a mixing rule to average dielectric functions of the inhomogeneous medium which is also called the Maxwell-Garnett theory (see Sec. 2.7.2; Bohren & Huffman 1983). I select porosities (the volume fraction of vacuum) of 10 % and 20 % for calculating effective

---

[1] Optical constants of amorphous SiO_2 from Phillip 1985.

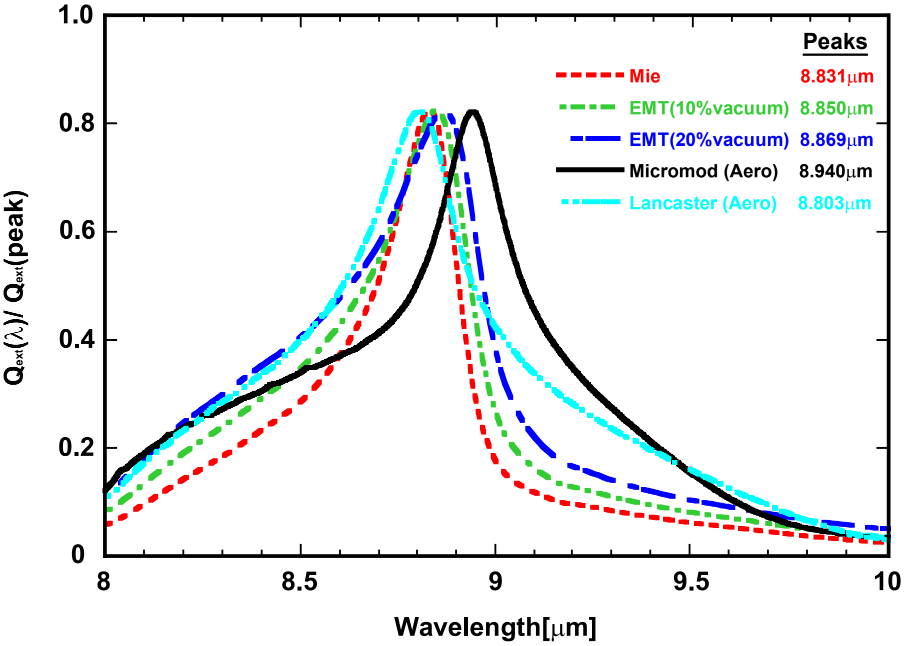

Figure 5.2: Normalized $Q_{\rm ext}$ vs. wavelength of amorphous SiO_2 via the aerosol measurements (Aero) with two different products (micromod and Lancaster; d=0.5 μm) compared to the results of the Mie and EMT calculations.

Table 5.1: Summary of the peak positions in wavelengths via the aerosol measurements, Mie, DDA, and T-matrix calculations for five different cluster shapes.

Theories\Cluster shape	Lin2 (μm)	Lin3 (μm)	Tetra4 (μm)	Clu16.1(μm)	Clu16.2(μm)
d=0.5 μm Experimental Peak WL **8.94** μm (Micromod), **8.80**μm (Lancaster)					
Mie calculation 8.83μm					
T-Matrix	8.81	8.81	8.83	8.83	8.89
DDA	8.83	8.83	8.86	8.89	8.89
d=1.0 μm Experimental Peak WL **8.95** μm (Micromod)					
Mie calculation 8.85μm					
T-Matrix	8.83	8.83	8.86	8.86	8.95
DDA	8.85	8.85	8.91	8.91	8.95
d=1.5 μm Experimental Peak WL **8.98** μm (Micromod), **9.01**μm (Lancaster)					
Mie calculation 8.89 μm					
T-Matrix	8.89	8.86	8.86	8.89	8.98
DDA	8.89	8.89	8.89	8.92	8.98

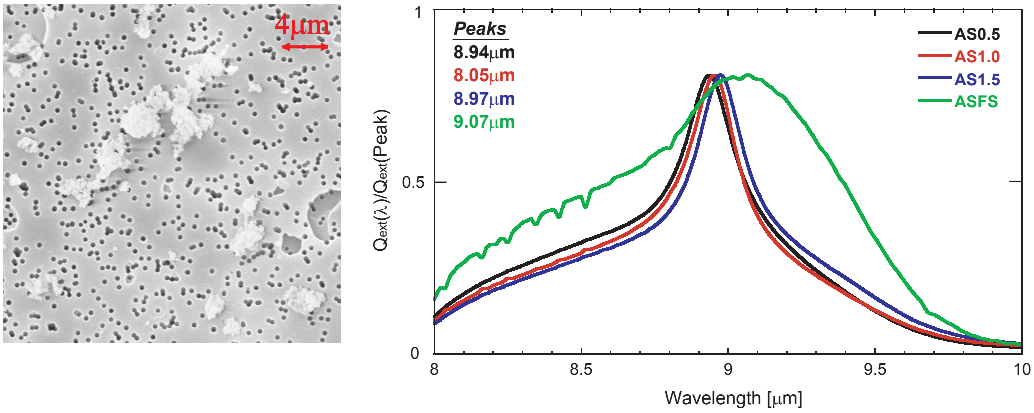

Figure 5.3: Left panel: The SEM image of the nano-sized particles, the ASFS sample. Right panel: Normalized Q_{ext} vs. wavelength of the three amorphous SiO_2 samples (AS0.5, AS1.0, and AS1.5) via the aerosol measurements compared with the nano-sized ASFS sample.

dielectric functions and applied the Mie theory afterwards. The results of this simulation are compared with the AS0.5 sample in Fig. 5.2. The Mie calculation for a compact material is shown as a standard. As the volume fraction of vacuum increases, the peaks shift merely to longer wavelengths compared to the Mie result for the compact material. Nevertheless, this shift is clearly too small. So, I conclude that the cause of these peak differences between the two samples is not only the effect of porosity, but it is also conceivable that the differences might be related to the properties of the SiO_2 materials themselves.

I consider that the large difference in the peak position between the Lancaster 0.5 and 1.5 μm samples (Table 5.1) is due to such an effect. Therefore, I prefer to use the experimental results, which are obtained from the micromod products, for hereafter comparison with astronomical spectra.

In addition, irregular shaped nano-sized particles (ASFS) has been studied in comparison with the monosphere particles (AS0.5, AS1.0, and AS1.5). As the particle size increases, the adhesiveness of the particles is weakened (see Sec.4.1.2). In other words, the nano-sized particles do easily form larger size agglomerates. As shown in Fig. 5.3 (left), most of the agglomerates are approximately $d>2$ μm in size and construct the close-packed shapes in the SEM image. Fig. 5.3 (right) shows the strong shift of the peak position and the change in the bandwidth obviously. The peak position difference between the AS0.5 (at 8.94 μm) and the ASFS (at 9.07 μm) samples is 0.13 μm to longer wavelengths and is not in the trend of the dependence on the size of constituent particles because the individual particle size of the monospheres is much larger than the ASFS one. Judging from the bandwidth of the ASFS sample, not only the size of the agglomerates influences the band profiles strongly, but also the shape of them (close-packed or elongated) according to the DDA calculations as shown in Fig. 5.4 (see more details in Sec. 5.1.3).

5.1.3 Agglomerate effect

The comparison of experimental and theoretical results is given in Fig. 5.4. No excessive differences are seen in the extinction efficiency calculations between the discrete dipole approximation (DDA) and the T-matrix methods for five different cluster shapes (Fig. 2.10; see Sec. 2.7.4 & 2.7.5). Hence, I demonstrate the DDA calculations and the experimental

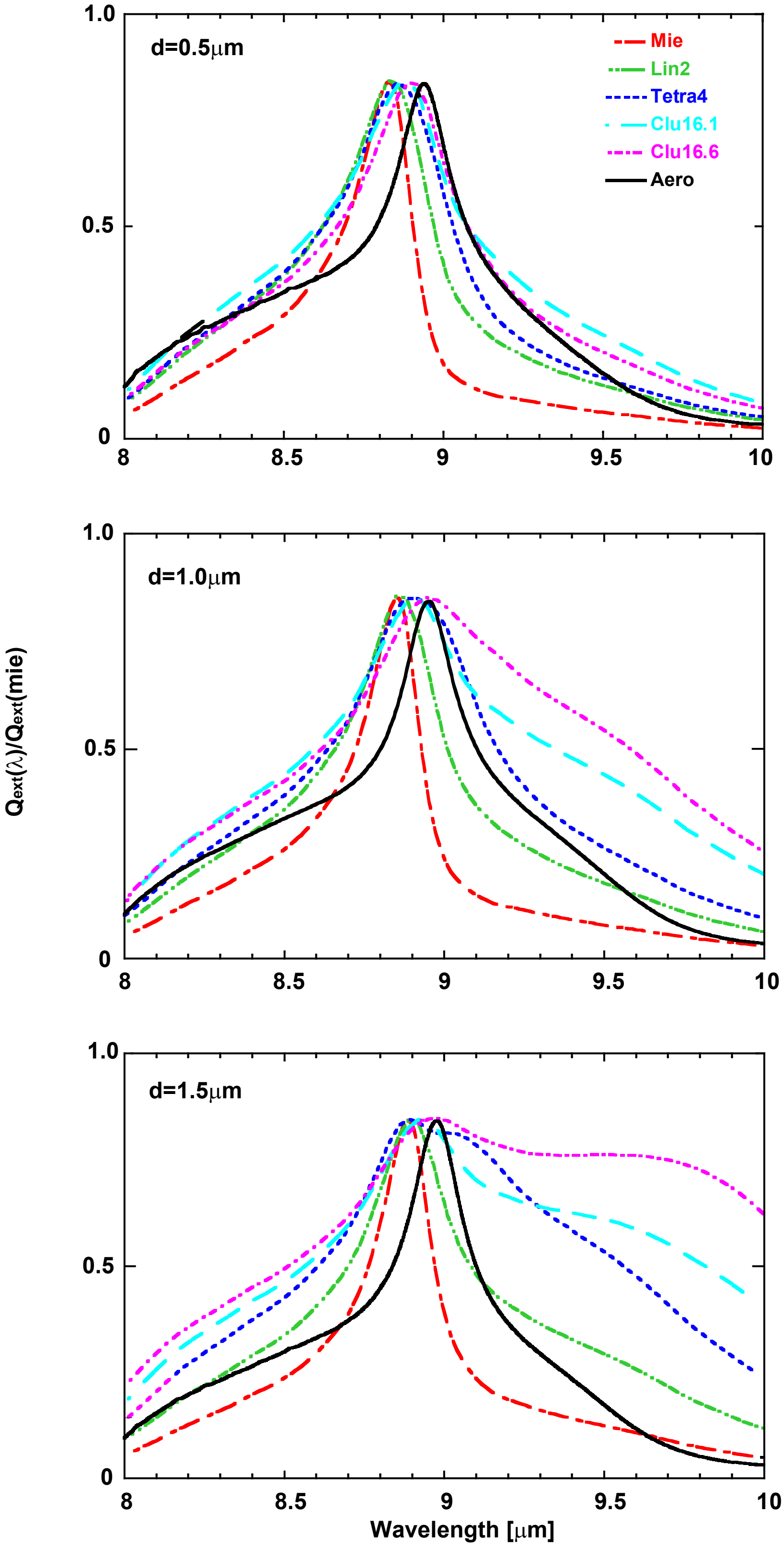

Figure 5.4: Calculated (Mie for a single particle and DDA for the five different cluster shapes) and measured (aerosol) normalized extinction efficiency Q_{ext} for the three particle sizes of amorphous SiO_2.

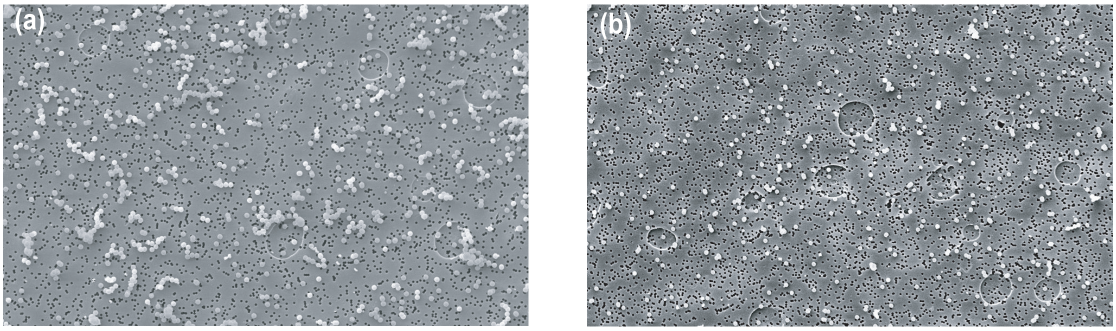

Figure 5.5: The SEM images of the two cases via the aerosol experiments. (a) Not making a use of the impactor to produce a large number of agglomerates. (b) Making a use of the impactor to produce mostly single particles. Note that the black dots in the SEM pictures are holes of the polyester filter having a diameter of 0.4 μm.

aerosol results of the monosphere samples with the three different particle sizes. Apart from a certain discrepancy between the experimental and theoretical peak positions, which I will discuss later, the main differences between calculated and measured spectra as well as among the calculated spectra are occurring at the long wavelength side of the band. The simple Mie result gives much too low extinction in this spectral range compared to the measured curve. With increasing aggregate size, extinction rises in this wavelength range, resulting in a better agreement with the experimental spectra for certain cluster sizes. This increase of the extinction is much stronger for larger constituent particles, where the calculated extinction for large clusters considerably exceeds the measured extinction. As a result of that, it might be conceivable that the suspended particles in the cell are mostly small agglomerate clusters which contain 2 to 10 particles dependence on size of constituents. In other words, there have not been enough single particles in the cell for the spectra to be compared with the Mie results.

Another result of the simulations is that the close-packed clusters (e.g. Cluster 16.2) tend to have a broader FWHM than the elongated ones (e.g. Cluster 16.1). The calculated peak positions (see Tab. 5.1) reveal a shift to longer wavelengths with increasing agglomerate size.

In order to examine the effect from the agglomeration, the proportion of the agglomerate and the single particles is modified while an impactor is detached from the setup. Fig. 5.5(a) and (b) show the SEM images of the two cases. Without the impactor, most particles constitute agglomerates which form both elongated and close-packed shapes in Fig. 5.5(a) whereas a lot of single monosphere particles are moderately distributed when the impactor is applied in Fig. 5.5(b). The estimated proportion of the particles contained in agglomerates to the single particles is six to four in the former case. Inversely, the agglomerates and the single particles are in the proportion of four to six in the latter case. In the latter case, almost all agglomerates consist of a small number of particles (2 to 3). Fig. 5.6 (left) is a plot of the normalized extinction efficiencies of the two cases. There is no noticeable change in the peak position at 8.95 μm; however, the bandwidth has been influenced by the agglomeration effect. As the number and size of the agglomerates increases, the bandwidth increases especially beyond the peak position. This effect is also seen and predictable in the theoretical calculations (see in Fig. 5.4).

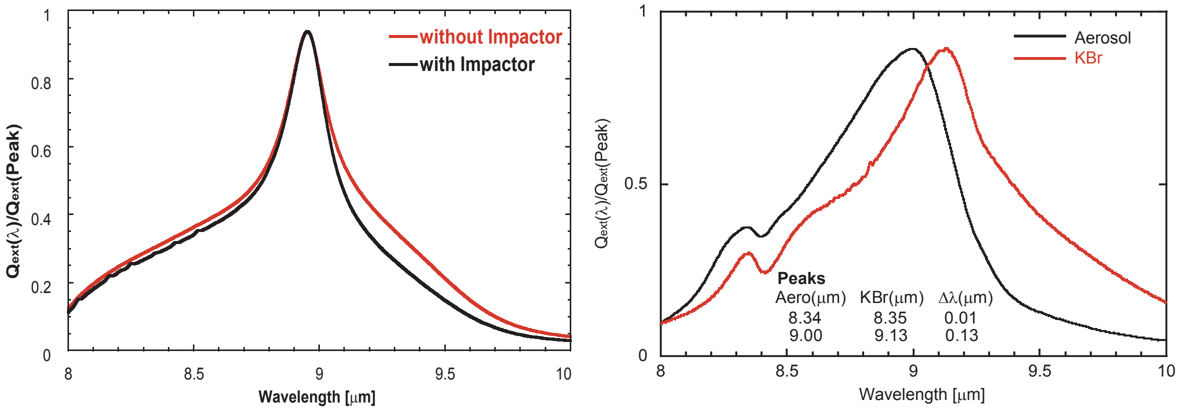

Figure 5.6: Left panel: Normalized Q_{ext} vs. wavelength of AS1.0 via the aerosol measurements compared with the two cases, which are less (with impactor) or more (without impactor) agglomerates in the cell. Right panel: Normalized Q_{ext} vs. wavelength of crystalline silica via the aerosol and KBr pellet measurements.

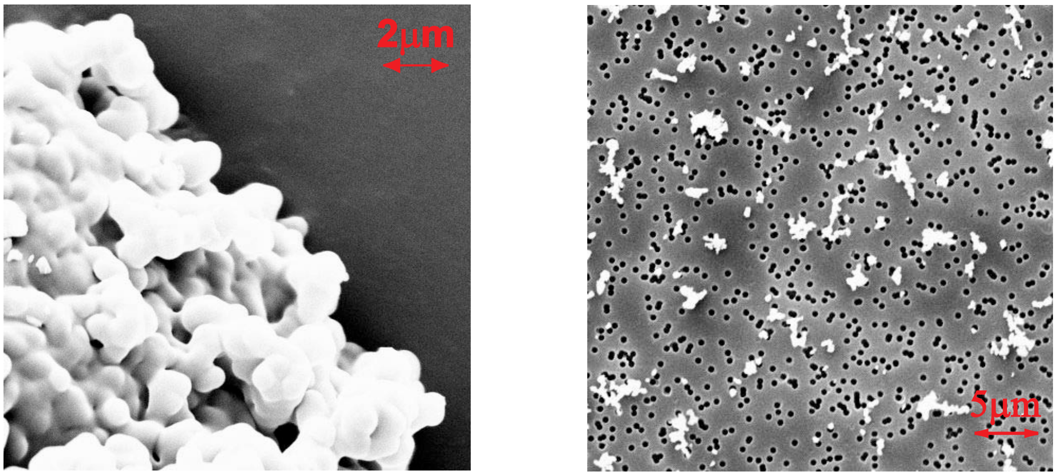

Figure 5.7: Left panel: SEM image of crystalline silica. Immediately after the annealing process is done. Right panel: Typical agglomerates of approximately 5 μm in size that have been directly sampled from the aerosol (TEM).

5.1.4 Crystalline vs. amorphous SiO_2

As mentioned in Sec. 2.7.1, vibrations of a crystal lattice cause absorption bands at long wavelengths. This is seen if the amorphous SiO_2 sample undergoes an annealing process to transform into crystalline form. For this purpose, the amorphous SiO_2 sample is placed in an oven with a temperature of 1450°C for one hour (see Fig. 5.7, left), and after the transformation is completed, the crystalline sample is milled carefully, and particles only $d<1$ μm in size are selected.

The difference between the peak position via the aerosol and KBr pellet measurements is approximately 0.1 μm which is very much alike the case of the amorphous samples as shown in Fig. 5.6 (right). Similarly, broader bandwidth is obtained with the KBr pellet technique compared to the aerosol experiment as well.

Fig. 5.7 (right) shows the SEM image of the crystalline silica particles in the cell via the aerosol experiment, which contains more elongated and close-packed agglomerates than single

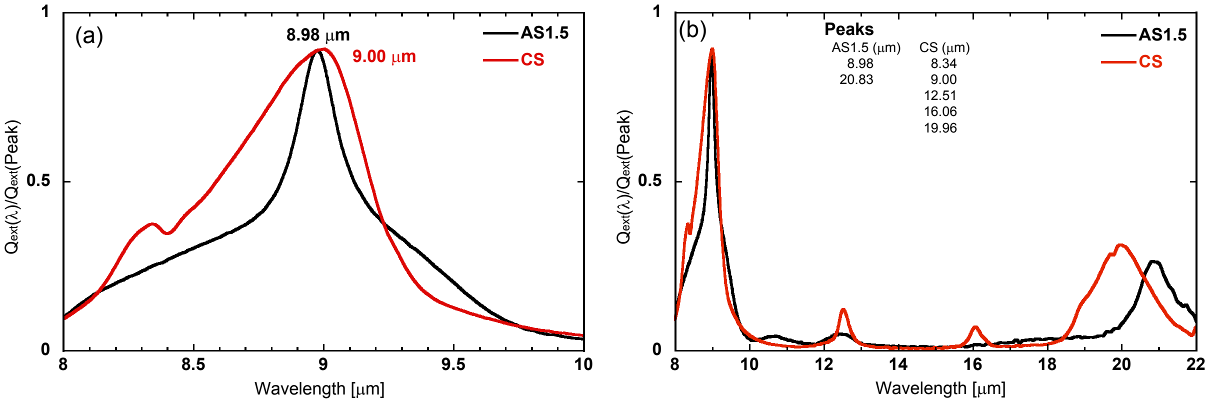

Figure 5.8: Normalized Q_{ext} vs. wavelength of the AS1.5 and CS samples via the aerosol measurements. (a) The wavelength between 8 to 10 μm. (b) The wavelength between 8 to 25 μm.

particles. Thus, that has a direct effect on the extinction spectrum at 9 μm in Fig. 5.8(a). In comparison with the AS1.5 spectrum, a distinct difference in the bandwidth can be seen rather than the peak position shift. Besides, more peak positions are detected at longer wavelengths in the case of the CS sample as shown in Fig. 5.8(b). The peak positions at 12.51, 16.06, and 19.96 μm cannot be seen in the amorphous SiO_2 spectrum (This section is based on Tamanai et al. 2006a).

5.2 Amorphous and Crystalline Silicates

Different sorts of silicates, which are amorphous and crystalline Mg_2SiO_4 (AF & CF1, CF2, CF3), amorphous and crystalline $MgSiO_3$ (AE1, AE2 & CE), and crystalline olivine ($Mg_{1.9}Fe_{0.1}SiO_4$) (CO), have been investigated in order to clear up the causes of the extinction band variations. Likewise, as in the case of silica, the description of the effects is divided into three sections: environment, size, and shape and agglomeration. Moreover, a difference between amorphous $MgSiO_3$ produced by the sol-gel processing and melting is discussed.

5.2.1 Matrix effect in silicates

As shown in Fig. 5.9, the aerosol spectroscopy reveals considerably different band positions and bandwidths as compared with the KBr measurements for the crystalline silicates. The band positions and their differences are given as inserted tables in the plots. The bands measured with the KBr pellet technique are shifted to longer wavelengths by amounts of up to 0.24 μm, especially for the strong bands of the olivine-type crystals, CF1, CF2, and CO at ~9.8 and ~11 μm. Smaller features which do not shift very much, change their appearance from isolated bands into shoulders and vice versa due to the shift of the strong bands. For the CE, the shifts are not that strong (typically 0.1 μm) but affect all the band components. For the amorphous materials, AF, AE1, and AE2, there is a clear detectable shift with the amorphous $MgSiO_3$, but a distinct shift is not seen with the amorphous Mg_2SiO_4.

The strong bands are more severely influenced than weaker ones. The strong bands are known to be due to geometrical resonances of the grains, which, for example, for spherical grains occur at ε=-2ε_m where ε and ε_m are the dielectric functions of the silicate and the embedding medium (1.0 for air; ≈ 2.3 for KBr; Lide 1990), respectively (see Sec. 2.7.1). This

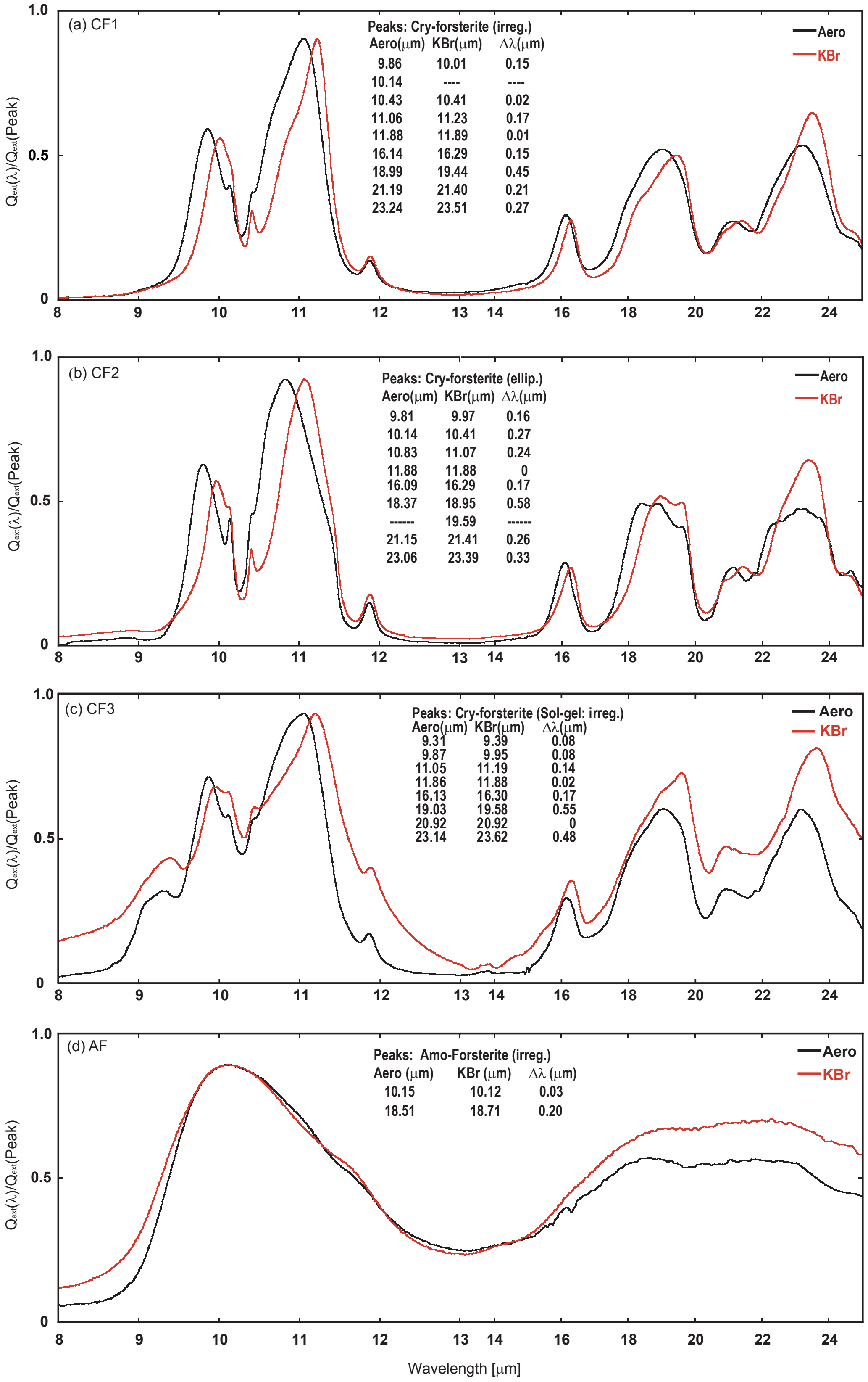

Peaks: Cry-forsterite (irreg.)

Aero(μm)	KBr(μm)	Δλ(μm)
9.86	10.01	0.15
10.14	----	----
10.43	10.41	0.02
11.06	11.23	0.17
11.88	11.89	0.01
16.14	16.29	0.15
18.99	19.44	0.45
21.19	21.40	0.21
23.24	23.51	0.27

Peaks: Cry-forsterite (ellip.)

Aero(μm)	KBr(μm)	Δλ(μm)
9.81	9.97	0.16
10.14	10.41	0.27
10.83	11.07	0.24
11.88	11.88	0
16.09	16.29	0.17
18.37	18.95	0.58
------	19.59	------
21.15	21.41	0.26
23.06	23.39	0.33

Peaks: Cry-forsterite (Sol-gel: irreg.)

Aero(μm)	KBr(μm)	Δλ(μm)
9.31	9.39	0.08
9.87	9.95	0.08
11.05	11.19	0.14
11.86	11.88	0.02
16.13	16.30	0.17
19.03	19.58	0.55
20.92	20.92	0
23.14	23.62	0.48

Peaks: Amo-Forsterite (irreg.)

Aero (μm)	KBr (μm)	Δλ (μm)
10.15	10.12	0.03
18.51	18.71	0.20

Figure 5.9: Normalized Q_{ext} vs. wavelength of the aerosol (Aero) and KBr pellet (KBr) measurements. (a) Irregular shaped crystalline forsterite (CF1); (b) Ellipsoidal shaped crystalline forsterite (CF2); (c) Irregular shaped crystalline forsterite via the sol-gel process (CF3); (d) Irregular shaped amorphous $Mg_{2.3}SiO_4$ via the sol-gel process (AF).

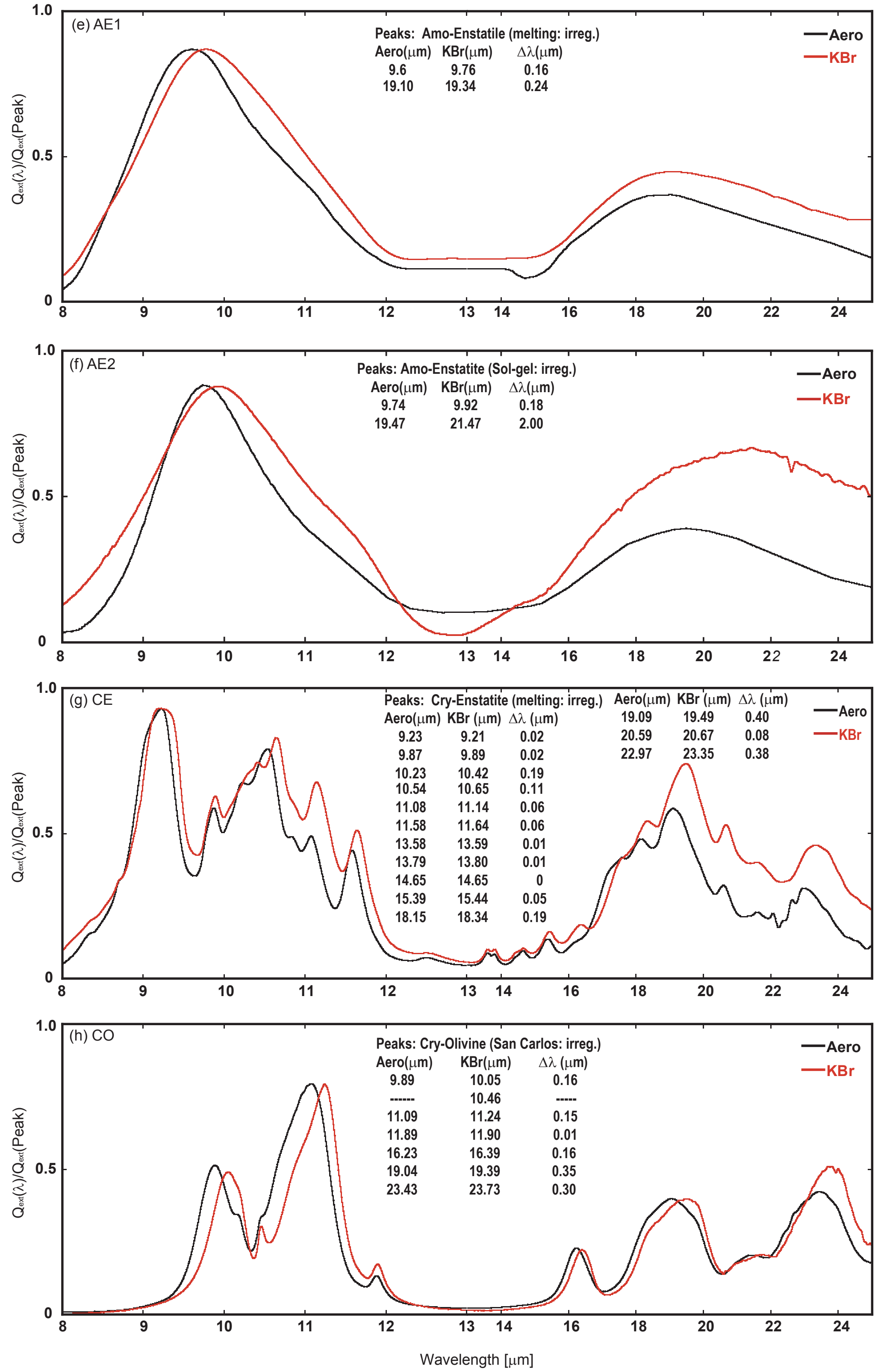

Peaks: Amo-Enstatile (melting: irreg.)

Aero(μm)	KBr(μm)	Δλ(μm)
9.6	9.76	0.16
19.10	19.34	0.24

Peaks: Amo-Enstatite (Sol-gel: irreg.)

Aero(μm)	KBr(μm)	Δλ(μm)
9.74	9.92	0.18
19.47	21.47	2.00

Peaks: Cry-Enstatite (melting: irreg.)

Aero(μm)	KBr (μm)	Δλ (μm)
9.23	9.21	0.02
9.87	9.89	0.02
10.23	10.42	0.19
10.54	10.65	0.11
11.08	11.14	0.06
11.58	11.64	0.06
13.58	13.59	0.01
13.79	13.80	0.01
14.65	14.65	0
15.39	15.44	0.05
18.15	18.34	0.19

Aero(μm)	KBr (μm)	Δλ (μm)
19.09	19.49	0.40
20.59	20.67	0.08
22.97	23.35	0.38

Peaks: Cry-Olivine (San Carlos: irreg.)

Aero(μm)	KBr(μm)	Δλ (μm)
9.89	10.05	0.16
------	10.46	-----
11.09	11.24	0.15
11.89	11.90	0.01
16.23	16.39	0.16
19.04	19.39	0.35
23.43	23.73	0.30

Figure 5.9: (*continued*) (e) Irregular shaped amorphous $MgSiO_3$ via the melting process (AE1); (f) Irregular shaped amorphous forsterite via the sol-gel process (AE2); (g) Irregular shaped crystalline enstatite via the the melting process (CE); (h) Irregular shaped crystalline olivine (CO).

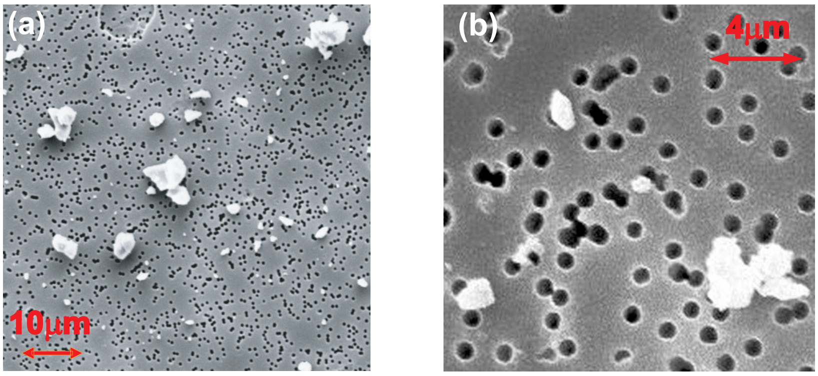

Figure 5.10: SEM images of the crystalline forsterite (CF1) with two different sizes. (a) Original size of the irregular shaped crystalline forsterite contains many large clumps approximately 7 μm in size. (b) Exactly a same material as (a), but the size of the particles are smaller via the sedimentation process ($d_{avg} \approx 3$-4 μm).

can probably explain the detected shift toward longer wavelengths, where ε decreases. On the other hand, the aggregation state of the particles in the aerosol and the KBr pellet techniques is probably different because of the different dispersion methods and the pressing of the pellets. Therefore, it may cause an additional influence on the band profiles. Unfortunately, the agglomeration state in the KBr remains unknown, consequently the strength of this effect cannot be explored.

5.2.2 Size effect in silicates

Originally, the CF1 particles are approximately 5 to 44 μm in size. Particles of size $d<1$ μm are collected through the sedimentation process (Sec. 4.4.1). Thus, these samples are fundamentally the same material but different in size. Fig. 5.10(a) and (b) show the SEM images of both the samples. Since the impactor has been utilized in the experiment, mostly the small size particles are concentrated there and carried up to the cell. This signifies for the original sample that particles of >5 μm size dominate in the aerosol (Fig. 5.10(a)) whereas the average size of the particles are approximately 3 to 4 μm for the sedimented sample (Fig. 5.10(b)). Thus, the clumps from the original sample remain in large numbers compared to the sedimentation one. Normalized extinction efficiencies of both the samples around the 11 μm extinction band are shown in Fig. 5.11. There is no excessive peak shift which is merely 0.03 μm. Nevertheless, the bandwidth is influenced effectively by the size differences. Particularly, there is a strong broadening of the band beyond the peak position for the original sample compared to the sedimentation one. This effect is also seen in the experiment with silica (Sec. 5.1.2). Hence, a disparity in size appears in the bandwidth rather than in a peak position shift.

5.2.3 Individual particle shape and agglomerate effects

The grain shapes can be examined in detail via microscopic analysis. The TEM images (Fig. 4.15) are not in direct view of the aerosol sampling; however, the images clearly show individual particle configurations refer to figures. The ellipsoidal shape of the crystalline forsterite particles are rather roundish (CF2) whereas those of the irregular shaped crystalline forsterite (CF1 and CF3) are non-uniform particles which have both sharp and rounded edges.

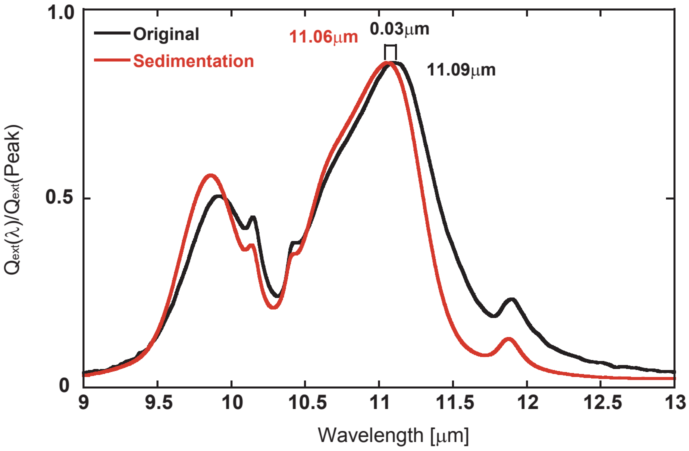

Figure 5.11: Normalized Q_{ext} vs. wavelength of crystalline forsterite with the original size and the smaller size particles by the sedimentation process.

The band profiles measured for these samples clearly differ in the sense that the peaks of the geometrical resonances are shifted by up to 0.23 μm toward shorter wavelengths for the roundish crystalline forsterite grains (CF2) in Fig. 5.12 (left) even though the size of both the agglomerates are indistinguishable from each other (d_{avg}≈3-4 μm) (Fig. 5.12(a) and (b)). Also, both the irregular shaped samples do not indicate distinctive differences at the peak positions although there is a slight difference in the bandwidths. Though it cannot be directly proven that the peak shift is a pure consequence of the grain shape, it is plausible that roundish grains have peaks at shorter wavelength because the geometrical resonances of a sphere are situated at such shorter wavelengths (see Fig. 5.12(left)). In contrast, irregular grains generally seem to produce geometrical resonances at longer wavelengths, i.e. closer to the transverse optical lattice frequencies. In addition, even if 3 to 4 μm agglomerates are dominating in the cell (this is the same for CF2 and CF3), agglomerate is not responsible for the effect.

5.2.4 Amorphous silicates

Even if the sample production process is completely different in the crystalline materials (e.g. forsterite from a commercial product (CF1) and the sol-gel process (CF3), the excessive change at 11 μm peak positions is not perceived in the aerosol experiments (see in Fig. 5.12). Nevertheless, the peak position difference arises in the amorphous materials of $MgSiO_3$. Fig. 5.13 (right) shows the peak position difference between AE1 (melting) and AE2 (sol-gel) which is 0.14 μm in wavelength. The disparity between these two materials appears not only at the peak position, but also at the short wavelength edges which indicate that these materials are in different amorphous state. In addition, since both the samples are very much identical with those of the shapes via the TEM images (see Fig. 4.15(f) & (g)), these differences appeared in the bands are independent from the shape effect. In fact, it is not simple to produce an exactly same amorphous state of sample with controlling the cooling rate (see Sec. 3.1). In this case, the disparity may be caused by the porous structure of the sol-gel material as shown in Fig. 5.13 (left).

Furthermore, although in amorphous silicate negative values of ε and therefore geometrical resonances do not occur, a small band shift is expected for particles in KBr compared to aerosol measurements in Fig. 5.9. Calculations of the peak positions in KBr and vacuum for the continuous distribution of ellipsoid (CDE) model and with Mie theory give $\Delta\lambda$=0.04

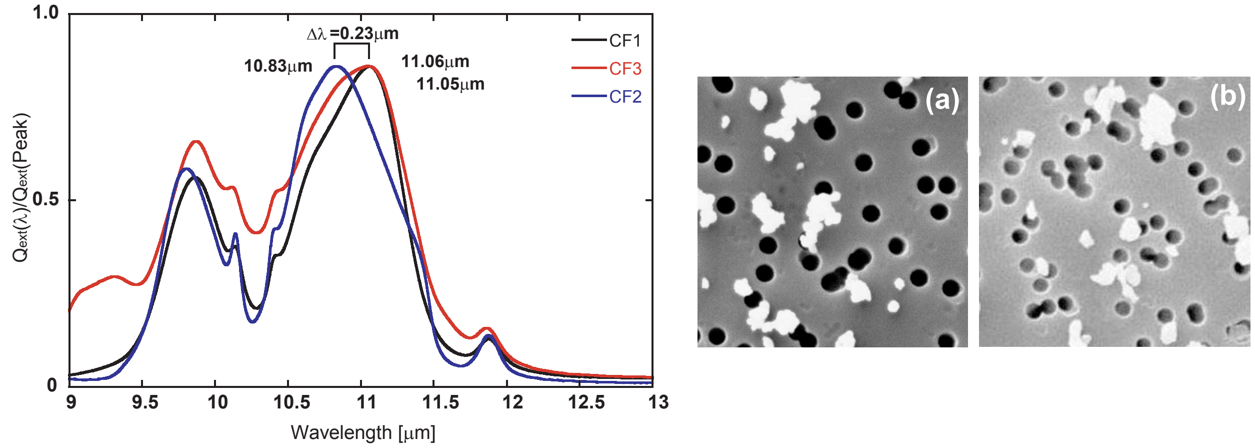

Figure 5.12: Left panel: Normalized Q_{ext} vs. wavelength of crystalline forsterite compared with the ellipsoid shape (CF2) and the irregular shapes (CF1 and CF3). Right panel: SEM images of (a) the ellipsoid particles (CF2); (b) the irregular shaped particles (CF3) deposited through the aerosol experiments. The back dots are the holes of the polyester filter having a diameter of 0.4 μm.

and 0.27 μm, respectively for the amorphous enstatite (AE1)[1], and $\Delta\lambda$=0.02 and 0.20 μm, respectively, for the amorphous forsterite (AF)[2]. Because the CDE approach produces a broader extinction efficiency curve compared to the Mie calculation, there arises the different $\Delta\lambda$ in the Mie and CDE calculations (Sec. 2.7.2 & 2.7.3). However, this shift is seen in the amorphous $MgSiO_3$, but not in the amorphous Mg_2SiO_4, which is currently not yet well understood (This section is based on Tamanai et al. 2006b).

5.3 Amorphous and Crystalline High Condensation Temperature Materials

The band profiles between 8 and 25 μm in wavelength of high condensation temperature crystalline materials, Al_2O_3(corundum), $MgAl_2O_4$(spinel), and TiO_2(rutile), have been studied by the use of the same investigation methods as the silica and silicate dust grains. The results are classified into two parts which are environment and disparity of two products in crystalline α-corundum.

5.3.1 Matrix effect in high condensation temperature materials

Fig. 5.14 represents the extinction spectra of all high condensation temperature samples. Substantially different band positions and bandwidths are obtained from the aerosol spectroscopic measurements as compared with the KBr pellet technique. The peak position differences amount to about 1.0 μm for the geometrical resonances of the crystalline α-corundum (CC1) grains (see Sec. 5.2.1) as shown in Fig. 5.14(a). In order to verify the difference in the bandwidths of the aerosol and KBr pellet measurements, the two continuous distribution of ellipsoids (CDE1 & CDE2) methods[3] are applied (Sec. 2.7.3). The CDE1 calculates the

---

[1] Optical constants (Dorschner et al. 1995; http://www.astro.uni-jena.de/Laboratory/Database/silicates.html).

[2] Optical constants (Jäger et al. 2003; http://www.astro.uni-jena.de/Laboratory/Database/silicates.html).

[3] Optical constants of α-corundum from Querry 1985.

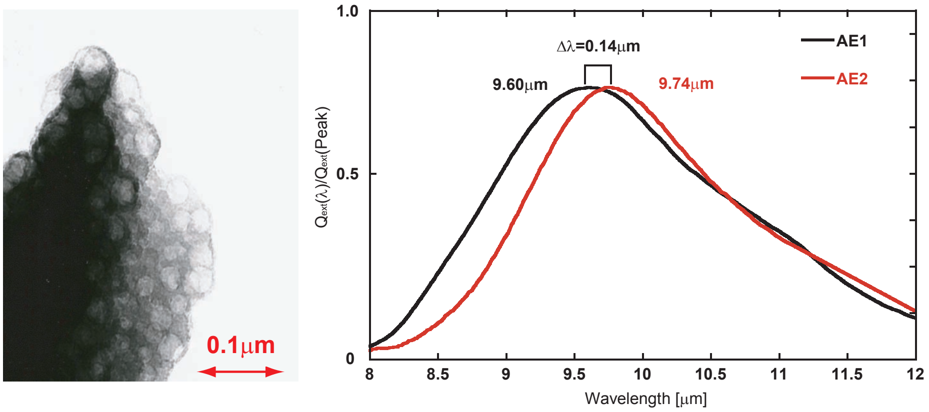

Figure 5.13: Left panel: TEM image of the amorphous $MgSiO_3$ via the sol-gel process (AE2). The porous configuration of the amorphous material is clearly visible. Right panel: Normalized Q_{ext} vs. wavelength of amorphous $MgSiO_3$ comparing the melting (AE1) and the sol-gel (AE2) materials.

extinction efficiency of most likely near-spherical particle shapes whereas the CDE2 assumes all ellipsoidal shapes with equal probability (see more details in Fabian et al. 2001b). Fig. 5.15 shows the comparison of the CDE2 calculations with the aerosol and KBr pellet measurements for CC1 sample. The CDE2 calculations predict that there occurs a bandwidth difference in vacuum and KBr media. The CDE2 calculation predicts broad bands ($\approx$ 10.5 - 18 μm) for both the KBr and aerosol measurements. In fact, the broad band in that wavelength range is seen in the aerosol measurement, but not in the KBr measurement. A possible explanation for the bandwidth difference between the both measurements is that extreme shaped agglomerates (e.g. elongated agglomerates) are formed by small size particles in the aerosol experiments. A definite cause of the difference in the bandwidths of the aerosol and KBr pellet measurements is not well understood.

It is also interesting that the extra peaks around 17 and 22.47 μm appear only in the spectrum measured with the aerosol technique, which is not in the least able to notice in the KBr measurements. A different product of the crystalline α-corundum (CC2) spectrum measured with the KBr pellet technique is shifted to longer wavelengths as well. The maximum peak position shift is less than the case of the CC1 which is the amount of up to 0.64 μm. Likewise, the crystalline γ-corundum (CCg) shows the band shift to longer wavelengths in the KBr measurement; however, the shift is exceedingly small compared to the α-corundum samples ($\Delta\lambda_{max}$=0.29 μm).

The same effect can be seen in both the crystalline spinel (CSp) and rutile (CR). The largest shift is produced by the CR in the entire samples. The maximum difference is 1.49 μm in wavelength. In every respect, all spectra of crystalline materials measured with the KBr pellet technique are shifted to longer wavelengths due to geometrical resonances of the grains (see Sec. 5.2.1).

5.3.2 The disparity of products

Two different crystalline α-corundum samples, which are CC1 and CC2, have been examined. Unlike amorphous materials, the crystalline solids have the uniform atomic order in certain geometric lattices (see Sec. 3.2). Thus, as far as the materials have the same crystalline structure, they ought not to produce extreme variations in measured spectra. However, in point

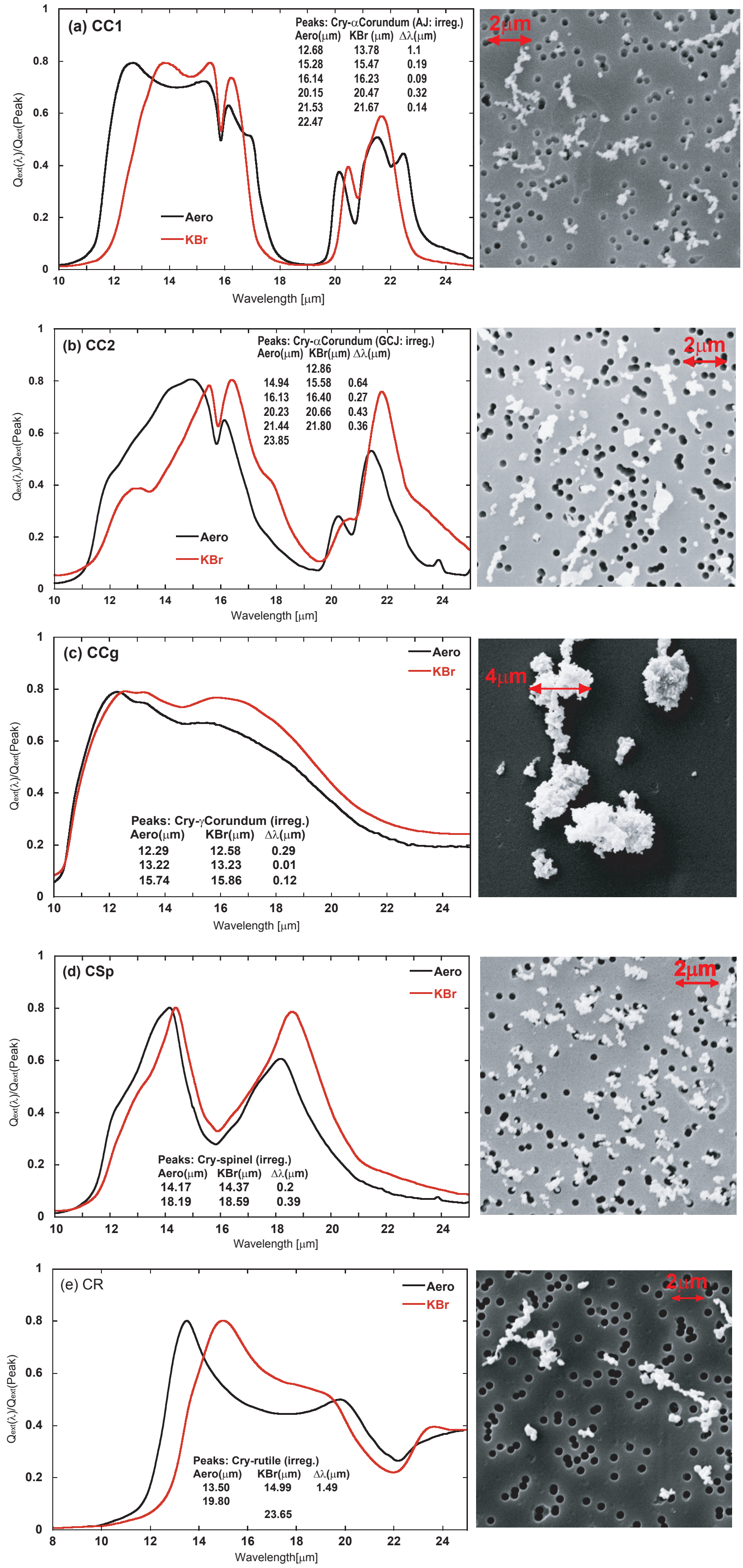

Figure 5.14: Normalized Q_{ext} vs. wavelength of (a) Irregular shaped crystalline α-corundum (CC1); (b) Irregular shaped crystalline α-corundum (CC2); (c) Irregular shaped crystalline γ-corundum (CCg); (d) Irregular shaped crystalline spinel (CSp), and (e) Irregular shaped crystalline rutile (CR).

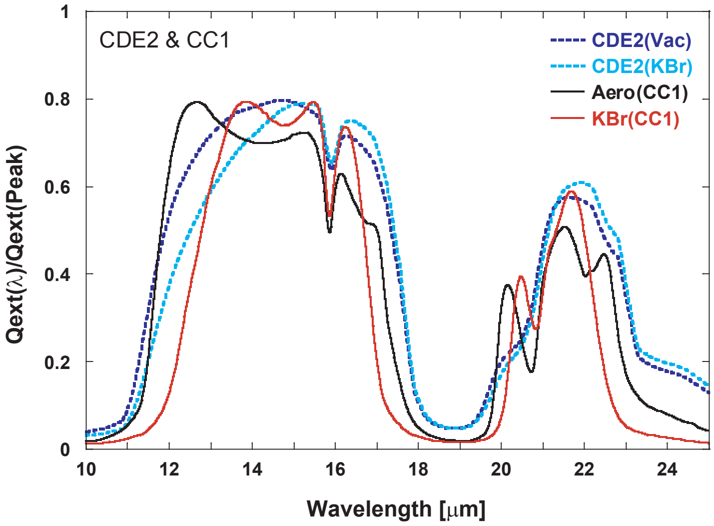

Figure 5.15: Normalized Q_{ext} vs. wavelength of crystalline α-corundum (CC1) via both the aerosol (Aero) and KBr pellet measurements compared with the CDE2 calculations in vacuum (Vac) and KBr media.

of fact, the two samples produce substantial differences in both the KBr pellet technique and aerosol measurement. In order to clarify that, the agglomerate effect is taken into account at the outset. The SEM images of both the samples reveal the clear shapes of the flying particles in the cell during the aerosol measurement (Fig. 5.14(a) and (b)). The CC1 particles form more complex and elongated agglomerates whereas the CC2 ones contain a lot of large clumps from the original powders. The TEM image in Fig. 4.15(m) indicates that the CC2 sample still includes large size clumps (d>5 μm) which probably cannot be separated in the dust disperser and impactor thoroughly. Fig. 5.16(a) and (b) show the spectra taken from the KBr and aerosol measurements for the CC1 and CC2 samples compared with the CDE1 and CDE2 calculations, respectively. The spectrum shape of the CC1 sample (Fig. 5.16(a)) is similar to trapezoid with three gradual peaks between 12 and 18 μm in wavelengths; therefore, an obvious broadening beyond the peak position cannot be seen in both the KBr and aerosol measurements in these cases. Nevertheless, the broadening appears in the CC2 sample (Fig. 5.16(b)) with both measurements. Especially, there is an excessive broadening beyond 16 μm in the aerosol measurement. This may be caused by the agglomerate effect due to a large number of the clumps.

Individual particle shapes clearly appear in the TEM images as well. The CC1 sample has rather roundish shapes whereas the CC2 one takes the form of sharp-edged particles. As discussed in Sec. 5.2.3, the peaks of the geometrical resonances shift to shorter wavelength in the case of the roundish crystalline forsterite grains. This result may also apply to these α-corundum grains. Indeed, both the experimental and theoretical spectra of the CC1 sample indicate the peak positions at short wavelengths compared to those of the CC2 sample. These calculations also demonstrate that the band profiles of the CDE1 results have some resemblance to the measured spectra of the CC1 sample (Fig. 5.16(a)) whereas the CDE2 calculated band profiles fit better with that of the CC2 sample (Fig. 5.16(b)). The peak position differences are seen as compared with the calculated and measured profiles since the CDEs calculate for particles in the Rayleigh limit (Sec. 2.7.2); therefore, the particles, which must be much smaller than that of wavelength, produce the disparity in peak positions. The CC2

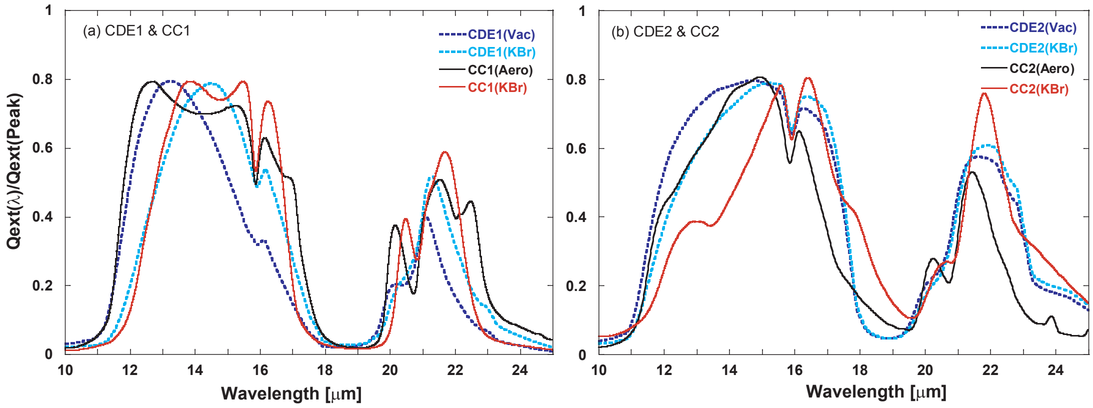

Figure 5.16: Normalized Q_{ext} vs. wavelength of crystalline α-corundum compared with the two different products which are CC1 and CC2 samples together with the two different CDE calculations. (a) Compared with CDE1 calculations in vacuum (Vac) & KBr media and the aerosol & KBr measurements with CC1 samples. (b) Compared with CDE2 calculations in vacuum (Vac) & KBr media and the aerosol & KBr measurements with CC2 samples.

sample has extra extinction at $\lambda > 18$ μm and $\lambda > 23$ μm (Fig. 5.16(b)). Probably these extra extinction is due to a size or agglomerate effects.

A major problem is how to interpret the twin peaks in the spectrum of the CC1 sample between 12 and 15 μm in wavelength. A possibility is that these twin peaks in the CC1 sample are integrated and appeared as one distinct sharp peak at 15.58 μm in the KBr pellet measurement and at 14.94 μm in the aerosol measurement for the spectrum of the CC2 sample. Contrary to the peak position, these spectrum valleys at 15.86 and 20.72 μm in the aerosol and 15.88 and 20.81 μm in KBr measurements correspond well to each sample. Other peaks from the CC2 sample, specifically beyond 15.8 μm valley, are situated at slightly longer wavelengths. By the same token, the valleys of the CDE results agree relatively well with both the aerosol and KBr measured spectra as well in Fig. 5.15 and Fig. 5.16(a) & (b). Hence, the peak around 14 μm region is strongly influenced for some reason which may be from morphological effects (especially, shape effect), moderately different bond distance in the crystal structure (Jäger, private communication), and/or purity of the sample itself. Unfortunately, a specific cause of the peak position and shape differences between the two samples is not well understood.

Chapter 6

Comparison with Astronomical Observations

I demonstrate the importance of the experimentally measured extinction spectra by directly applying them into observed spectra. In this section, five types of astronomical objects, which are young stellar objects (YSOs) including T Tauri stars (TTSs) and Herbig Ae/Be (HAEBE) stars, Vega-type stars, oxygen-rich Asymptotic Giant Branch (AGB) stars, and comet are taken into consideration.

6.1 T Tauri stars (TTSs)

In recent years, advanced observational techniques have provided new information of the star and planet formation process via YSOs. Specifically, knowledge with regard to low-mass ($M \lesssim 2$ $M_\odot$) and intermediate mass stars (2 - 10 $M_\odot$) have been considerably enhanced.

T Tauri stars (TTSs) are YSOs, which have lower mass ($M \lesssim 2$ $M_\odot$) than that of HAEBE stars (see Sec. 6.2), associated with nebulosity. These are also pre-main-sequence stars (<10 Myrs) having low temperature spectra from F to M types (equivalent in surface effective temperatures ~7000-3000 K) (Joy 1945; Herbig 1962; Bertout 1989) together with strong emission lines caused by chromospheric activity [1] and stellar winds (Illingworth 1994; Hartmann 1998).

TTSs are divided into two types depending on strength of Hα emission. When Hα emission width is broader than 10 Å, the objects are called "classical" TTSs (CTTSs) which emit exceedingly strong emission lines since they are surrounded by large-scaled disks. Conversely, if Hα emission width is narrower than 10 Å, TTSs belong to "weak-emission" pre-main-sequence stars (WTTSs) which have very thin disks or no remaining disks around.

It is conceivable that these WTTSs hold a clue to understand the early phases of stellar evolution because some of fragments (e.g. dust grains and molecules) existed in circumstellar disks might be utilized for planetesimal formation; as a result, there are no obstructions anymore from the remnants of the disks. In Taurus, approximately 40 % of the known TTSs with ages younger than 3 Myr belong to WTTS which signifies that almost half of pre-main-sequence objects do not indicate clear evidences or at least signs of the circumstellar disks in existence (e.g. detection of near-infrared emission and/or optical hot continuum emission from the disks) (Hartmann 1998). A reason why some of few million years TTSs possess the disks or not is still the unsolved issue. Enhancing an apprehension of the physical and chemical dust properties are necessitated to solve the question with reagrd to evolution of the circumstellar

---

[1] The chromospheric activity is a set of phenomena that requires rapid rotation and a deep convective outer envelope which exists in TTSs, but not in HAEBE stars.

Table 6.1: Properties of the three different stars: TTS, HAEBE, Vega-type.

Object	Class	Spectral type	T [K]	Age [Myr]	Ref.
Hen 3-600A	TTS	M4	$T_{stellar}$=3200*	10†	Schegerer et al. (2006)
HD104237	HAEBE	A4Ve	T_{eff}=10500	—	Meeus et al. (2001)
HD113766	Vega-type	F3/F5V	$T_{adopted}$=6750	10-20‡	Schütz et al. (2005)

∗ A reference from Metchev et al. (2004).
† A reference from Kessler-Silacci et al. (2005).
‡ A reference from Meyer et al. (2001).

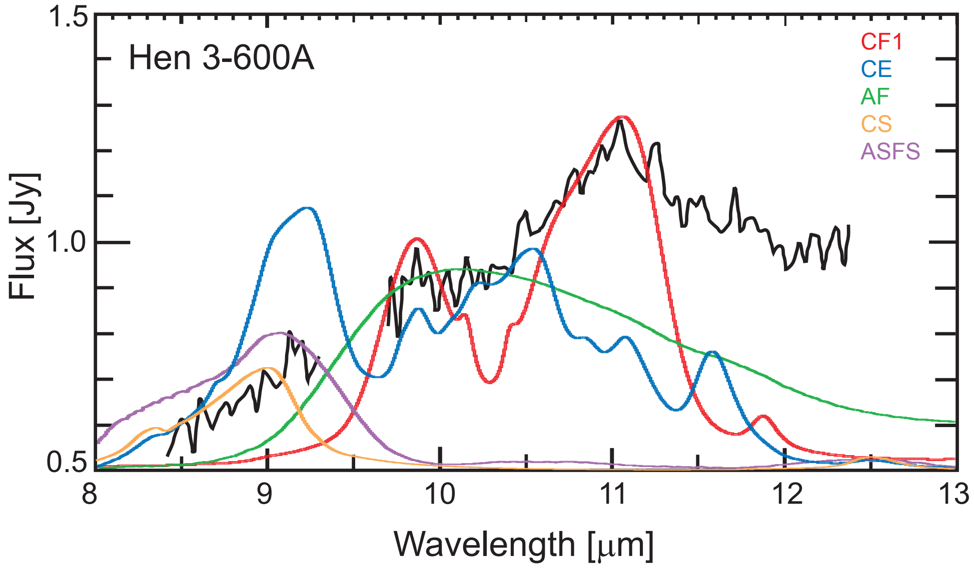

Figure 6.1: The emission spectrum of a TTS, Hen 3-600A (Schegerer et al. 2006) is compared to the spectra of CF1, CE, AF, CS, and ASFS via the aerosol measurements. Note that a small gap around 9 μm in the emission band is due to incorrectable atmospheric ozone feature.

disks in TTSs to planet formation.

A detailed information of observed emission spectra of Hen 3-600 (TTS), HD104237 (HAEBE), and HD113766 (Vega-type) stars are in Table 6.1. The spectrum of Hen 3-600A has been analyzed by Honda et al. (2003) with the use of Subaru COMICS[2] and Schegerer et al. (2006) with W.M. Keck Observatory, LWS[3]. Due to the use of their different fitting procedures (see more details in Schegerer et al. 2006), the resultant spectrum of Hen 3-600A is slightly different. The N-band emission spectrum of Hen 3-600A (Schegerer et al. 2006) is compared to five different experimental results as shown in Fig. 6.1. Interestingly, the strong peak position of the crystalline forsterite appears at nearly 11 μm that the aerosol result of CF1 reproduces fittingly as well as the peak at 9.9 μm. The peaks of CE measured spectrum via the aerosol reproduce the peak positions of the observed emission spectrum as well, especially at 9.23, 9.87, and 11.08 μm. A wavelength between 9 and 9.2 μm might be from crystalline enstatite like CE, crystalline silica like CS, irregular shaped amorphous SiO_2 like the ASFS samples, or all under the condition that the grain size must be very large. However, it is necessary to analyze the observed spectrum with a longer wavelength range in order to confirm whether it is the crystalline or amorphous SiO_2 dust grains since the typical CS feature appears beyond

---

[2] 8.2 m Subaru Telescope, Cooled Mid-Infrared Camera and Spectrometer (COMICS) with the high resolution (R=250) has been used.

[3] Long Wavelength Spectrometer (LWS) with the lower resolution (R=150) was used.

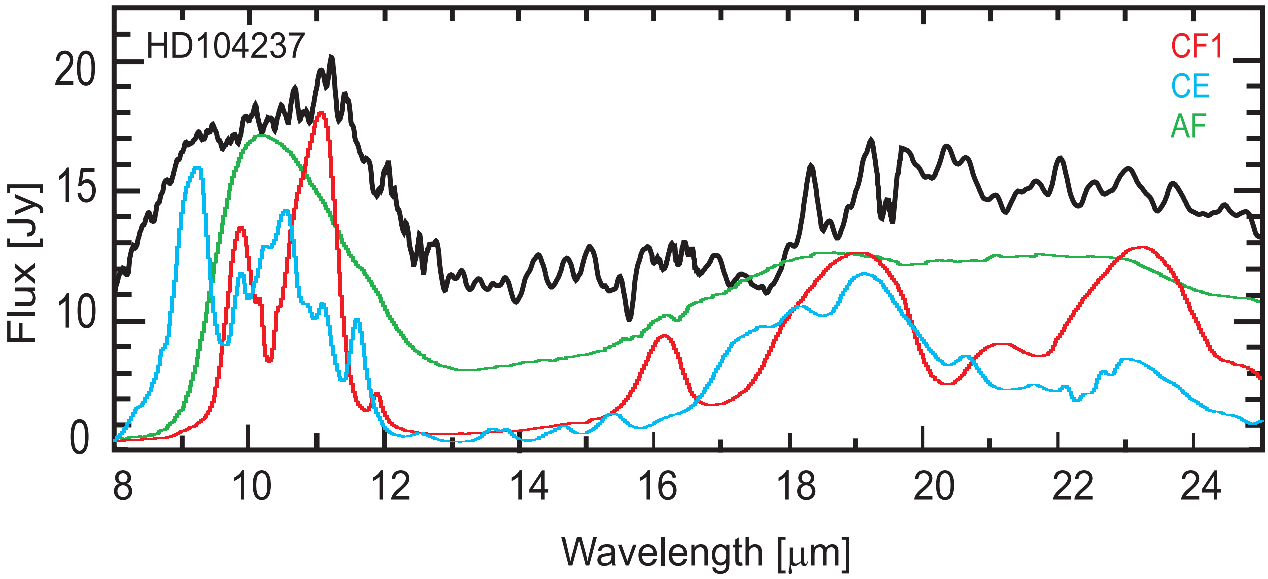

Figure 6.2: Comparison of the emission spectra for a HAEBE star, HD104237 (Meeus et al. 2001) with the extinction efficiency measured in the aerosol experiments (CF1, CE, and AF).

12.5 μm (see in Fig. 5.8, right). In addition, because the most crystalline materials show more absorption peaks beyond 16 μm, it is necessary to compare the band profiles in a wide range.

This TTS, Hen 3-600A does not only contain exceedingly crystalline-rich dust grains, but also a large amount of amorphous silicate and possibly SiO_2 are present which indicate that active ongoing annealing may take place for further condensation process because the existence of SiO_2 has a close connection with that of the crystalline forsterite to form pyroxene type of silicate such as enstatite (Bouwman et al. 2001).

6.2 Herbig Ae/Be stars (HAEBE stars)

HAEBE stars, which are very young (<10 Myr) pre-main-sequence intermediate mass stars, are embedded in the gas and dust envelopes and might be surrounded by circumstellar disks. Herbig (1960) proposed the criteria of HAEBE stars taking account of that the stars are connected with a nebulosity. After new discoveries regarding HAEBE stars (a detection of some isolated HAEBE stars that were not related to nebulae or dark clouds (e.g. Walker & Wolstencroft 1988; Hu et al. 1991; Oudmaijer et al. 1992, Malfait et al. 1998)), the criteria have been modified as below:

- ⋆ Spectral types A or B together with emission lines
  (correspond to surface effective temperatures ∼ 7500 - 30000 K)

- ⋆ IR radiation excess due to circumstellar dust

- ⋆ Luminosity class III to V (III giants; IV subgiants; V main sequence)

Massive stars ($M>10\ M_\odot$) are considered to be able to form exclusively in giant molecular clouds whereas low-mass stars start to take place their formation not only in giant molecular clouds, but also in dark clouds (or dark nebulae) where interstellar gas and dust are contained dense enough to obscure partially or completely the light from stars; therefore, HAEBE stars hold a key to understand the process between massive star and low-mass star formation (Appenzeller 1994).

Furthermore, it is conceivable that HAEBE stars are ancestors of Vega-type stars (will discuss in Sec. 6.3), which are closely related with planet formation process (Waters & Waelkens 1998; Bouwman 2001). Extensive investigation of dust properties in HAEBE stars promotes a better understanding of planet formation processes.

As Meeus et al. (2001) suggested the presence of crystalline silicates and/or larger silicate grains in HD104237 as shown in Fig. 6.2, there is a high possibility to contain large size dust grains according to the broad bandwidth between 10 and 12 μm in wavelength which may originate especially from large size amorphous silicate grains. The indications of the crystalline forsterite and enstatite grains in existence are seen at around 11, 16, 19, and 23 μm and 9, 10.5, 19, and 23 μm, respectively.

So far, although the crystalline forsterite dust grains are detected in many HAEBE systems, the incontrovertible evidence for the presence of the crystalline enstatite grains has been reported in only two systems which are HD72106 (Schütz et al. 2005a) and HD179218 (Bouwman et al. 2001). It may be a possibility that there is a chemical reaction of forsterite and silica to form enstatite in a sufficient temperature and pressure (Sec. 3.3.1) (e.g. Rietmeijer et al. 1986; Bouwman et al. 2001). However, the formation process and mechanism have not been clarified yet. The spectrum of the CE via the aerosol measurement reproduces well expressly the wavelength range between 9.87 and 10.5 μm compared to the spectrum of HD104237 (Fig. 6.2); therefore, HD104237 may possibly contain the large size crystalline enstatite dust grains as well.

6.3 Vega-type stars

As discussed in a previous section 6.2, Vega-type stars may be descendant of HAEBE stars. Vega-type stars which are ordinary main-sequence stars with the intermediate mass, but have substantial infrared excess emission that suggests an existence of abundant dust grains orbiting around the central star. Considering a short lifetime of the orbiting dust grains (Burns et al. 1979) and the effect of Poynting-Robertson drag, the dust grains must be supplied by some other sources. Weissman (1984) proposed that the dust grains around Vega-type stars are replenished by larger objects: comets strew over dust grains when they pass by Vega-type stars; planetesimals collide with each other, and their fragments are sprinkled around Vega-type star regions as well as asteroids. In other words, Vega-type stars are surrounded by circumstellar debris disks. One of the most important discoveries in these Vega-type stars is that some planets, planetary companions, and planet candidates have been detected in the Vega-type system (Mayor et al. 1995; Marcy & Butler 1998; Marcy et al. 1999; Kürster et al. 2000). These discoveries may be a clear evidence of planet formation in the disks.

The study of the dust grains in the debris disks of Vega-type stars will give a hint for evolutional process of planet formation and be able to trace the stages through which HAEBE stars pass as they develop into Vega-type stars.

A Vega-type object, HD113766 is selected for a comparison. HD113766 has been confirmed by Mannings & Barlow (1998) as a Vega-type star. HD113766 is a binary system, and the excess flux comes from the primary star of the system (Meyer et al. 2001). Fig. 6.3(a) shows the emission spectrum of the crystalline silicate-rich Vega-type star HD113766 (Schütz et al. 2005), together with the band profiles of CF1, CE, and AF measured via the aerosol measurements

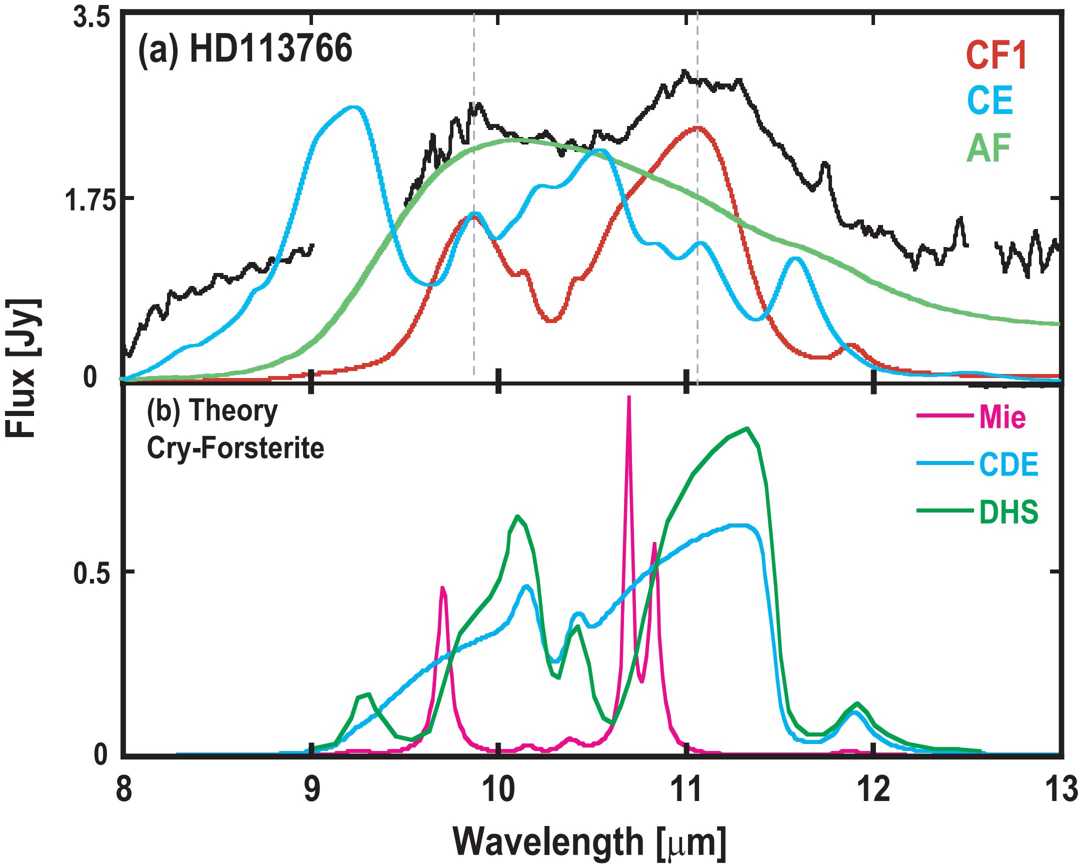

Figure 6.3: Comparison of the observed emission features for a Vega-type star, HD113766 with the experimental results and theoretical calculations. (a) HD113766 (Schütz et al. 2005) and the CF1, CE, and AF spectra obtained from the aerosol measurements. The light gray dotted lines denote the peak positions of the CF1 aerosol result. (b) Calculated band profiles for crystalline forsterite using the Mie (r=0.1 μm), CDE, and DHS models. Note that a small gap between 9.4 and 9.7 μm in the emission band of HD113766 is due to incorrectable atmospheric ozone feature (Schütz et al. 2005).

as well as calculated band profiles of crystalline forsterite[4] for the CDE model (Bohren & Huffman 1983), and for the distribution of hollow spheres (DHS) model in Fig. 6.3(b) (Min et al. 2005).

Evidently, the calculated band profiles cannot reproduce both the observed and laboratory-measured data. The CDE model leads to band profiles that are far broader than the laboratory measurements. The DHS model predicts the structure of the observed band correctly as compared with the emission spectrum of HD113766 but produces peaks at excessively long wavelengths, particularly at 10.1 μm (similar to the CDE). In contrast to this, the aerosol measurement of the CF1 sample reproduces quite well the positions of the main peaks in the observed spectrum at 9.9 and 11.0 μm. The peak at 11.3 μm, however, is not reproduced. This may indicate that the disk of HD113766 contains much larger grains (larger than 3 to 4 μm which is the average dust grain size of the aerosol measurement for the crystalline forsterite). In addition, the band profiles of CF2 fail to reproduce the observed features (see Fig. 5.9(b))

---

[4] Optical constant of crystalline forsterite from Servoin & Pirious 1973 are used.

since the peak positions are situated much shorter than the irregular ones. This may be a clue that the forsterite- or olivine-type grains in HD113766 differ in their morphological properties from the small roundish grains like the ellipsoidal particles. I should note here that the measured spectrum of the natural olivine grains provides a similar match like that of the crystalline forsterite. Therefore, this may be a possibility that HD113766 may include crystalline olivine instead of the forsterite, or both of them may be coexisting in the disk. Schütz et al. (2005) mentioned the existence of large size amorphous silicate and absence of SiO_2. Regarding to the amorphous silicate, amorphous forsterite might be a possible candidate for that in Fig. 6.3.

As discussed in Sec. 6.2, the existence of SiO_2 has a close connection with that of crystalline forsterite due to the thermal annealing system (Bouwman et al. 2001). Although SiO_2 has been found in HAEBE stars in general, it cannot be detected easily in Vega-type stars. Hence, it is conceivable that crystalline silicates are replenished by collisions of large bodies and/or come flying comets which signifies that the second generation dust plays an important role in Vega-type stars rather than dust from the annealing process.

It is difficult to determine the dust properties by the type of stars. Both HAEBE and Vega-type stars bear a close resemblance in those dust features. Consequently, further investigation is necessary to clarify.

6.4 Oxygen-rich Asymptotic Giant Branch (AGB) stars

The main dust grain source is located in the outflow of asymptotic giant branch (AGB) stars as mentioned in Sec. 2.1. The chemical and mineralogical compositions of dust grains in AGB stars are not clarified yet. The strong 13 μm band has been detected from oxygen-rich circumstellar envelopes around evolved stars has some possible candidates such as Al-silicates, SiO_2, Al_2O_3, $MgAl_2O_4$, TiO_2 (e.g. Tielens 1990; Begemann et al. 1997; Posch et al. 1999; Fabian et al. 2001a).

In fact, Posch et al. (1999) have shown that neither corundum nor rutile could not account precisely for the 13 μm emission band because the peak position of the corundum was situated slightly at shorter wavelength (12.7 μm). In contrast, the rutile was located rather in longer wavelength (13.4 μm). Only the case of spinel corresponded closely with the 13 μm emission band (12.95 μm) via their theoretical approaches. Fabian et al. (2001a) have verified the synthesized spinel by taking different Al/Mg-ratios into account. They found out that the peak position of the near-stoichiometric synthetic spinel (e.g. $Mg_{1.01}Al_{1.99}O_4$ and $Mg_{0.94}Al_{2.04}O_4$) fitted well at 13 μm in wavelength compared with the spectra of oxygen-rich circumstellar shells.

Most of the refractory materials, which are defined as chemical substances that are removed from the vapor phase at relatively high temperatures, could be condensed into grains. As the temperature drops, grains begin to condense out of the gas. A complete understanding of planet formation requires a search for the highest temperature at which condensation occurs. Then, the whole condensation sequence will be revealed. For that reason, it is important to verify the 13 μm band profile of the AGB stars. In this subsection, I attach great importance to the morphological effects to examine the 13 μm band profile for some AGB objects.

Three AGB stars are compared with the experimental results and basic properties of these objects are compiled in Table 6.2. Fig. 6.4(a), (b), and (c) show the observed emission spectra of these AGB objects together with the experimentally measured spectra of crystalline γ-corundum (CCg), crystalline spinel (CSp), and crystalline rutile (CR) in the wavelength

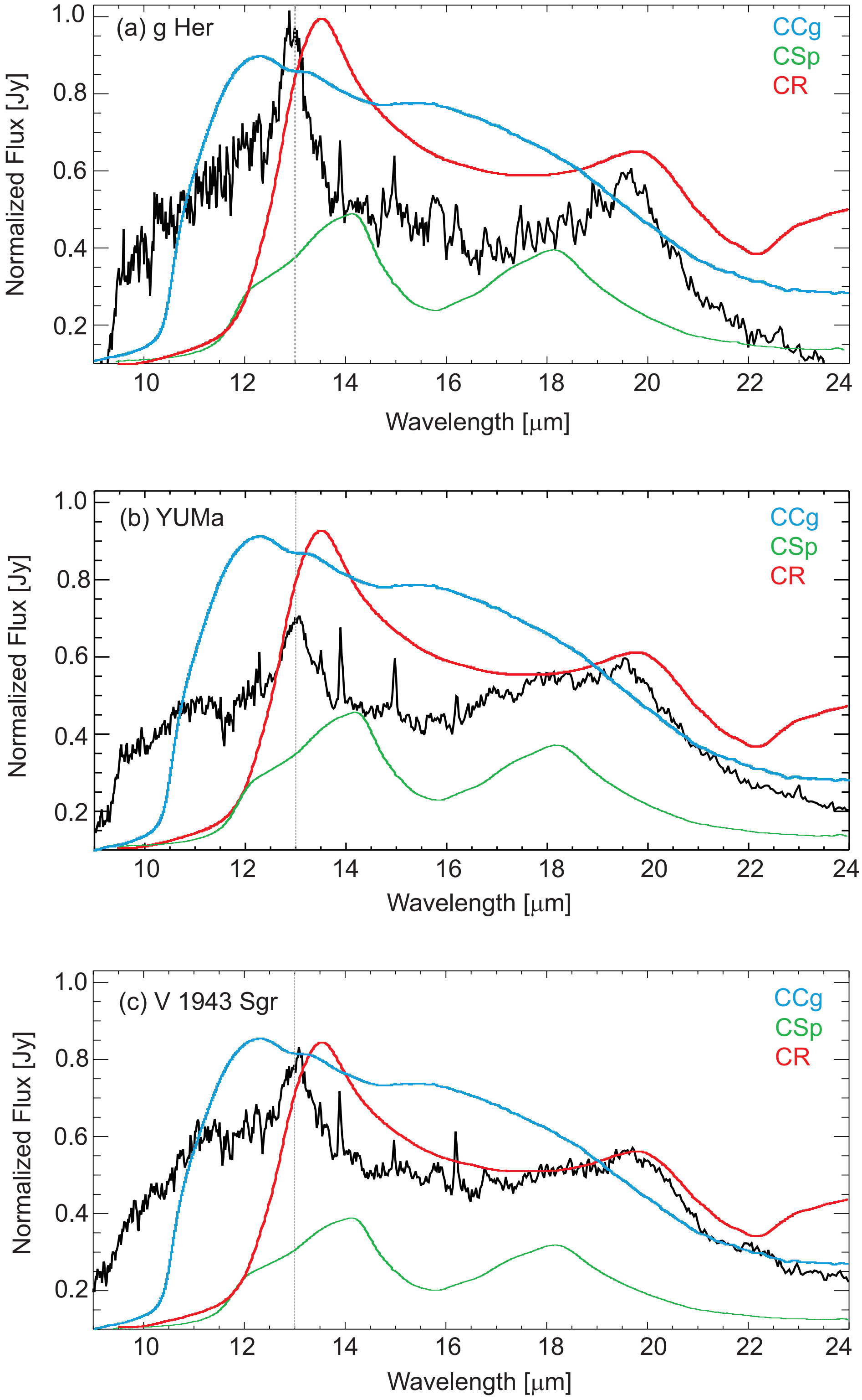

Figure 6.4: Comparison of the observed emission features for the three AGB stars with the experimental results. (a) The emission spectrum of g Her (Posch et al. 1999 & 2002); (b) YUMa (Posch et al. 1999 & 2002); (c) V 1943 Sgr (Fabian et al. 2001a & Posch et al. 2002) are compared with the aerosol measurements of CCg, CSp, and CR. The gray dot lines denote the 13 μm.

Table 6.2: Properties of the three AGB stars.

Object	Class	Spectral type	Band pos. [μm]	Ref.
g Her	SRb	M6III	12.95, 19.5	Posch et al. (1999) & (2002)
Y UMa	SRb	M7II-III	13.0, 19.5	Posch et al. (1999) & (2002)
V1943 Sgr	Lb	M8	13.0, 19.5	Fabian et al. (2001a); Posch et al. (2002)

range between 9 and 24 μm.

Another characteristic of AGB star spectra is the prominent 19.5 μm dust emission feature. Thus, it is suitable to compare the observed spectra with the experimental results in a wide range of wavelengths. A very strong 13 μm feature appears in all three objects as well at 19.5 μm. The crystalline spinel measured via the aerosol measurement cannot reproduce the peak position at both 13 and 19.5 μm. This is probably due to presence of larger grains. Nevertheless, 19.5 μm feature is reasonably reproduced by the CR via the aerosol measurements. Although the CR does not reproduce the peak at 13 μm well, the downslope between the peak positions at 13.5 and 19.8 μm correspond well with these observed emission spectra. Hence, both peaks at 13 and 19.5 μm may originate from crystalline rutile. In fact, the theoretical calculation predicts that the primary condensation species in oxygen-rich circumstellar dust shells around pulsating AGB stars is TiO_2 as a most promising candidate (Jeong et al. 1999). Although the presence of rutile dust grains in spectra of AGB stars have not been confirmed so far, it comes as no surprise that the TiO_2 will be present in the environment.

A different possibility of the 13 μm feature is that if the grain size of crystalline α-corundum (CC1) is larger (>10 μm), the peak position may shift to longer wavelengths; however, both crystalline samples (CC1 and CC2) do not reproduce any peaks at 19.5 μm (Fig. 5.14(a) & (b)). Hence, it is still a question whether the crystalline α-corundum can be the one to originate the strong 13 μm feature. Also, the measured crystalline γ-corundum (CCg) spectrum cannot reproduce at both the peak positions as shown in Fig. 6.4. As Cami (2002) analyzed the spectrum of the AGB star G Her, the way of approaching is that each peak possibly arises from different sources such as a broad 11 μm band from amorphous alumina-oxide, a 13 μm band from spinel, and a 19.5 μm feature from $Mg_{0.1}Fe_{0.9}SiO_4$. However, it is conceivable that both the peaks at 13 and 19.5 μm originate from the same source due to the consistency of the descending slope between the peaks.

The CR sample is the one which makes the largest difference between the aerosol and KBr pellet measurements ($\Delta\lambda$=1.49 μm); therefore, the sample may be delicate to take care which means that a little difference in size, shape, and agglomeration state may exert a significant influence on the band profile. This still needs additional investigation to verify. Nevertheless, I suggest that the crystalline rutile is a promising candidate for the origin of the 13 and 19.5 μm for the AGB stars.

6.5 Comets

A comet is a mass of ice and dust that travels around the Sun or other stars. In general, comets are composed of three parts such as the nucleus, coma (their atmosphere), and tail. Comets are considered to form in a remaining molecular cloud after a star or planet formation. This remaining molecular cloud gives rise to a cocoon of comets which undergoes many collisions, integrations, adsorption of surrounding molecules in order to grow up as a nucleus. Thus, the nucleus of comets has preserved the fragments of primitive materials with original forms from the beginning of the solar system. Whipple (1951) proposed the "dirty snowball" model for the cometary nucleus which is a few kilometers in size solid object consisting mainly of water ice, mixture of silicate grains and dust. Dust and molecules in the coma and tail of comets arise from the evaporation of the nucleus as a comet approaches to the Sun; therefore, these dust certainly come from the nucleus of comets. A few things have been clarified about the cometary dust through the IR observations so far.

Most of the dust in comets are few micrometer in size and considered to form porous aggregates with fractal structures which contain different chemical components (e.g. Greenberg & Hage 1990; Okamoto et al. 1994). The dust can be divided primarily into two mineralogical compositions. One is metallic materials such as iron and graphite. The other is silicates (Mukai 1982). Understanding the optical properties of the cometary dust grains traces the origin of the solar system.

Fig. 6.5 shows the emission spectrum from the dust grains of comet Hale-Bopp (C/1995 O1) in the coma which was observed by the short-wavelength spectrometer (SWS) of the ISO when the comet was located approximately 2.9 AU from the Sun on October 1996 (Crovisier et al. 1997) in the upper panel together with the CF1 and CO measured in the aerosol experiment in the bottom panel. Hale-Bopp represents strong emission features at about 10 to 12 (strongest peak at 11.3 μm), 19.5, and 23.5 μm, and a minor peak near 16 μm. On the whole, as Crovisier et al. (1997) stated, the peak positions of the Hale-Bopp spectrum correspond to these of the crystalline olivine and forsterite (Mg-rich olivine) particles. The aerosol results do not reproduce well with the observed emission feature that may be caused by the average size of the agglomerates and the individual particle sizes are too small in comparison to the dust grains in the coma of the Hale-Bopp. The bandwidths of the observed spectrum are much broader than that of the experimental ones. Specifically, the emission feature at near 10 μm does not appear as a clear sharp peak and looks like both 10 and 11.3 μm peaks continuously connected with each other. This phenomenon, that the peaks become dimmer, can be revealed in theoretical calculations (see Fig. 5.4) as the particle size increases.

As Li & Greenberg (1998) proposed that the average grain size of Hale-Bopp is approximately 7.9 to 25.3 μm and extremely porous, the dust grains in the coma may be exceedingly large and irregular in shape since small roundish dust grains have peak positions at shorter wavelengths. This is a next task to investigate how the high porous dust grains influence the band profiles.

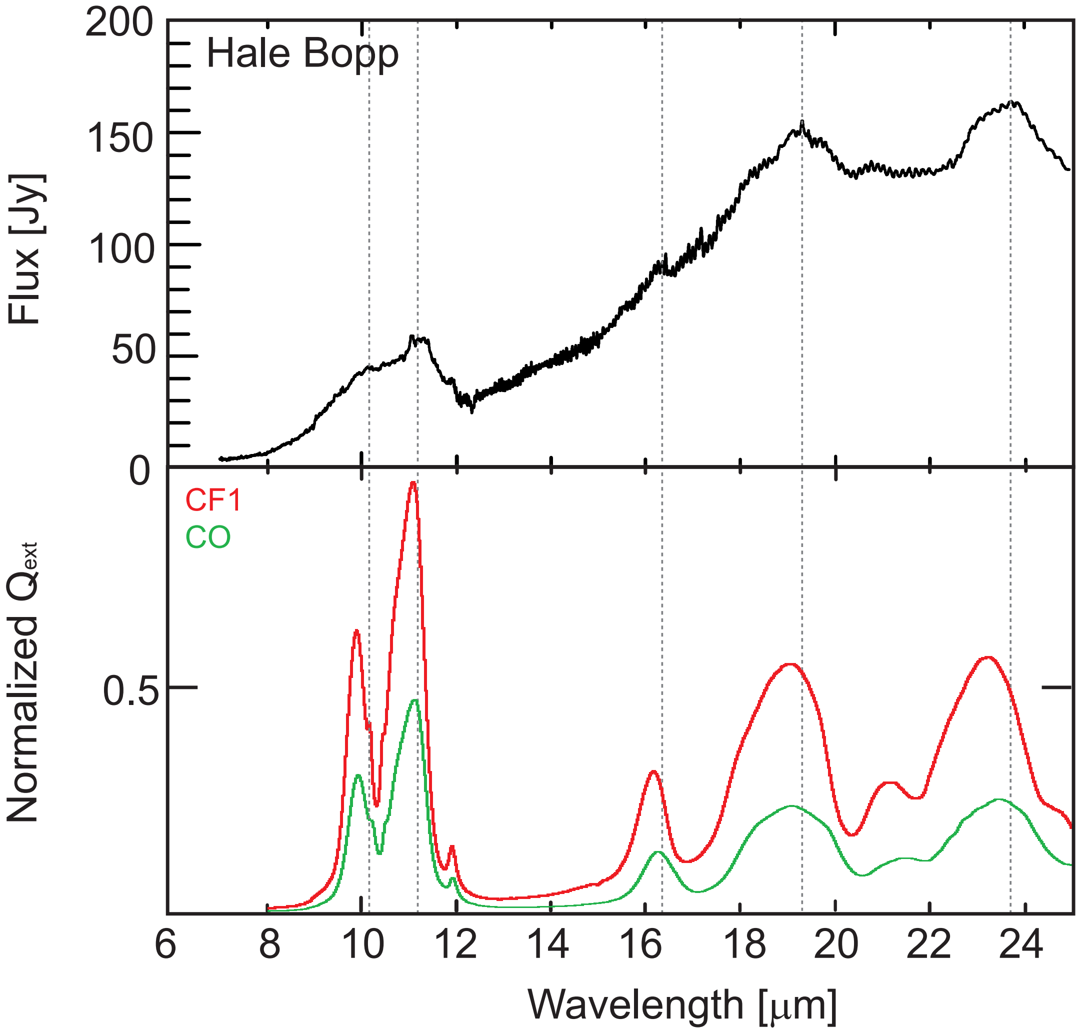

Figure 6.5: Comparison among the ISO-SWS spectrum from the comet Hale Bopp (C/1995 O1) (Crovisier et al. 1997) and the experimental spectra of CF1 and CO grains via the aerosol measurement. Note that the gray dot lines denote the peak positions of the observed spectrum.

Chapter 7

Conclusions and Outlook

The major part of this project provides the concept of corresponding to morphological influences on the experimentally measured extinction band profiles of dust grains avoiding the effect of electromagnetic interaction with solid embedding media.

Fundamental characteristic of astrophysically relevant solid materials such as silicate, silica, corundum, spinel, and rutile are summarized from the chemical and solid-state viewpoints. Extinction exceedingly depends on physical properties of the dust grains, for instance, the effects of conductivity, crystallinity, chemical composition, shape, and size.

Aerosol technology has been adopted for obtaining the extinction spectra of free-flying particles in the mid-infrared region of both amorphous and crystalline grains which are directly comparable to observed spectra. Simultaneously, the extinction has been measured via the classical KBr pellet technique as well in order to verify the influence of electromagnetic interaction with solid embedding media. The experimental setup is paid close attention to separate the dust particles as much as possible. A rotating brush dust disperser has been utilized because it is possible to maintain a constant aerosol flow. An originally manufactured impactor is applied for concentrating the smaller aerosol particles.

The experimentally measured extinction spectra are examined in order to investigate how the morphological effects exert on the band profiles together with making use of electron microscopes (TEM and SEM). The influence of electromagnetic interaction with solid embedding media is revealed via the comparison between the aerosol and KBr pellet measured spectra. Particularly, the crystalline grains show substantially different band positions and bandwidths. The aerosol measured spectra tend to shift toward shorter wavelengths due to geometrical resonances of the grains. The maximum peak position difference between the two measurements is produced by the crystalline rutile that is $\Delta\lambda$=1.49 μm.

The measured band profiles are not only influenced by the agglomerate shapes, but also by individual particle shapes. The band profiles measured for the irregular and ellipsoid shaped crystalline forsterite obviously differ from each other in a way that the peak positions of the geometrical resonances are shifted by up to 0.23 μm in the direction of shorter wavelengths for the ellipsoid grains in the aerosol experiments. Conversely, the irregular shaped grains appear to produce geometrical resonances at longer wavelengths in general, that is in the vicinity of the transverse optical lattice frequencies. Besides, close-packed agglomerates tend to result in a broader band than elongated ones as I have demonstrated by DDA calculations for differently shaped clusters of spherical SiO_2 particles.

The grain size difference has an effect on the band profiles as well. The spectrum from larger-sized crystalline forsterite grains shows a broader bandwidth; however, there is not much difference in the peak position ($\Delta\lambda$=0.03 μm).

The measured extinction spectra have been compared to the observed emission spectra of five different types of objects which are TTSs, HAEBE stars, Vega-type stars, oxygen-rich AGB stars, and a comet for the spectral analysis. Many observed emission spectra of YSOs and Vega-type stars as well as comets show a strong peak around 11 μm in wavelength which is indicating the existence of crystalline olivine-type (e.g. forsterite) dust grains. In previous work, the peak position of the crystalline forsterite has been fixed at 11.2 μm by the KBr pellet measurements. Nevertheless, the crystalline forsterite does not always have the peak position at 11.2 μm if the morphological effects are taken into consideration. Hence, even if a strong peak located $\lambda < 11$ μm is seen in the emission spectrum, the object possibly contains crystalline forsterite grains that may have roundish shapes and/or small in size.

The crystalline rutile may be a promising candidate for the source of the strong emission bands at 13 and 19.5 μm in AGB stars instead of crystalline α-corundum and spinel due to the correspondence of the observed and aerosol spectra.

Still, there is plenty of scope with regards to further improvements for this experiment. First of all, compared to the traditional KBr technique, the extinction measurement in aerosol has two disadvantages: it requires about 100 mg of material and it is, unfortunately, not quantitative. The column density of the dust grains along the spectrometer beam can hardly be estimated or measured to an accuracy higher than a factor of 2. A better accuracy could be achieved only by accompanying quantitative KBr measurements or by a determination of the material's optical constants, for example, by reflection measurements. In such a case and given that a theoretical model can be adjusted to represent correctly the morphological properties of the particulate, the aerosol spectra can be renormalized. Thus, it is necessary to find a way to modify the aerosol experiment to be quantitative.

Second, here are strong advantages of the aerosol method. Firstly, it lacks the problem of the embedding medium, which is inherent to the KBr method. A second major advantage is that the structures of the grains can be analyzed by either in situ or ex situ microscopic imaging. This allows investigation in detail of the influence of the grain morphology on the spectra and will hopefully help to calibrate theoretical approaches. More detailed information regarding the morphological aspects such as fluffy and porous grains can be explored by both the aerosol measurement and theoretical calculations.

Next, the fractal aggregate formation could be directly studied by IR spectroscopy. Although the particle densities are not high enough to give rise to grain growth so far, it is possible to observe the growth by aggregation with controlling the dust grain density in the cell.

Furthermore, the observed emission spectra comprise information of various dust grains. For that reason, heterogeneous dust grains, which are a mixture of some powdered samples, will be a next assignment to investigate. Also, the extinction of the wavelength range up to at least 60 μm will be examined. Recent development of high technological telescopes (e.g. Spitzer[1], VISIR[2], COMICS[3]) have the spectroscopic capability to deal with the mid-infrared range up to 40 μm. Since the crystalline silicates have more absorption peaks beyond 25 μm, a longer

---

[1] Spitzer Space Telescope is owned by NASA, U.S.A. It covers the mid-IR range between 5.3 and 40 μm with low resolution.

[2] The Very Large Telescope (VLT) spectrometer and imager for mid-infrared (VISIR) is owned by ESO. It covers the wavelength range between 8 and 13 μm (N-band) and 16.5 and 24.5 μm (Q-band).

[3] Subaru telescope, The Cooled Mid-Infrared Camera and Spectrometer (COMICS) is owned by National Astronomical Observatory of Japan (NAOJ). It covers the mid-IR range between 7.8 and 13.3 μ (low resolution N-band) and 16.7 μm and 20.7 μm (medium resolution Q-band).

wavelength coverage is necessary for clarifying the precise silicate properties (e.g. forsterite or olivine).

Finally, it should be possible to manipulate the dust in situ by surface condensation or irradiation, so that the influences of such effects on the IR spectra can be measured well with the aerosol technique.

List of References

Abbas, M.M., Craven, P.D., Spann, J.F., Tankosic, D., Leclair, A., and West, E.A. 2004, *Laboratory experiments on charging of individual dust grains*, in American Geophysical Union Fall Meeting, Abst. Nr. SH43B-02

Agladze, N.I., Sievers, A.J., Jones, S.A., and Burlitch, J.M. 1996, *Mm-wave absorption by two level systems in microscopic amorphous grains*, J. of Non-Crystalline Solids, 203, 37

Allard, F., Hauschildt, P.H., Alexander, D.R., Tamanai, A., and Schweitzer, A. 2001, *The limiting effects of dust in brown dwarf model atmosphere*, ApJ, 556, 357

Anderson, E.E. 1971, Modern Physics and Quantum Mechanics, (Philadelphia: W.B. Saunders Company)

Appenzeller, I. 1994, in The Nature and Evolutionary Status of Herbig Ae/Be Stars, eds. P.S. Thé, M.R. Perez, and Ed P.J. van den Heuvel, 62, 12, (ASP Conference Series)

Atkins, P. 1994, Physical chemistry, (N.Y.: W.H.Freeman and Company)

Barrado v Navascue's, D., Stauffer, J.R., Song, I., and Coillault, J.-P. 1999, *The age of beta Pictoris*, ApJ, 520, L123

Bartelmehs, K.L. 1996, http://ccp14.minerals.csiro.au /ccp /web-mirrors /xtaldraw /crystal /silicate.htm

Begemann, B., Dorschner, J., Henning, Th., and Mutschke, H. 1997, *Aluminum oxide and the opacity of oxygen-rich circumstellar dust in the 12-17 micron range*, ApJ, 476, 199

Bejan, A., Tsatsaronis, G., and Moran, M. 1996, Thermal Design & Optimization, (N.Y.: John Wiley & Sons, Inc.)

Bertout, C. 1989, *T Tauri stars: Wild as dust*, ARA&A, 27, 351

Blakemore, J.S. 1985, Solid State Physics, (N.Y.: Cambridge University Press)

Bohren, C.F., & Huffman, D.R. 1983, Absorption and Scattering of Light by Small Particles, (N.Y.: John Wiley & Sons Inc.)

Bouwman, J. 2001, PhD Thesis, University of Amsterdam, The Netherlands

Bouwman, J., Meeus, G., de Koter, A., Hony, S., Dominik, C., and Waters, L.B.F.M. 2001, *Processing of silicate dust grains in Herbig Ae/Be systems*, A&A, 375, 950

Bradley, J.P., Brownlee, D.E., and Veblen, D.R. 1983, *Pyroxene whiskers and platelets in interplanetary dust: evidence of vapour phase growth*, Nature, 301, 473

Brady, J.E., and Holum, J.R. 1988, Fundamentals of Chemistry with Quantitative Analysis, (N.Y.: John Wiley & Sons)

Brinker, C.J., and Scherer, G.W. 1990, Sol-gel Science, (London: Academic Press Inc.)

Burlitch, J.M., Beeman, M.L., Riley, B., and Kohlstedt, D.L. 1991, *Low-temperature syntheses of olivine and forsterite facilitated by hydrogen peroxide*, Chem. Mater., 3, 692

Burns, J.A., Lamy, P.L., and Soter, S. 1979, *Radiation forces on small particles in the solar system*, Icarus, 40, 1

Busani, T., and Devine, R.A.B. 2005, *Dielectric and infrared properties of TiO_2 films containing anatase and rutile*, Semicond. Sci. Technol., 20, 870

Clément, D., Mutschke, H., Klein, R., and Henning, Th. 2003, *New laboratory spectra of isolated β-SiC nanoparticles: Comparison with spectra taken by the Infrared Space Observatory*, ApJ, 594, 642

Cowley, C.R. 1995, An Introduction to Cosmochemistry, (N.Y.: Cambridge University Press)

Crovisier, J., Leech, K., Bockelée-Morvan, D., Brooke, Y., Hanner, M.S., et al. 1997, *The spectrum of Comet Hale-Bopp (C/1995 O1) observed with the Infrared Observatory at 2.9 astronomical units from the sun*, Science, 275, 1904

Debye, P. 1909, *Der Lichtdruck auf Kugeln von beliebigem Material*, Ann. Phys., 30, 57

DePew, K.D., Speck, A.K., Dijkstra, C., and Hofmeister, A.M. 2005, in American Astronomical Society Meeting 207, Buelletin of the American Astronomical Society, 37, 1466

Dominik, C., Gail, H.P., and Sedlmayr, E. 1989, *The size distribution of dust particles in a dust-driven wind*, A&A, 223, 227

Dominik, C., Sedlmayr, E., and Gail, H.P. 1993, *Dust formation in stellar winds VI. Moment equations for the formation of heterogeneous and core-mantle grains*, A&A, 277, 578

Dominik, C. 2000, Habilitationsschrift, Technische Universität Berlin, Germany

Dorschner, J., and Henning, Th. 1986, *Experimental investigations of astronomically important interstellar silicates*, ApSS, 128, 47

Dorschner, J., Begemann, B., Henning, Jäger, C., Mutschke, H. 1995, *Steps toward interstellar silicate mineralogy II. Study of Mg-Fe-silicate glasses of variable compositions*, A&A, 300, 503

Draine, B.T. 1988, *The discrete dipole approximation and its application to interstellar graphite grains*, ApJ, 333, 848

Draine, B.T., and Goodman, J. 1993, *Beyond Clausius-Mossotti: wave propagation on a polarizable point lattice and the discrete dipole approximation*, ApJ, 405, 685

Draine, B.T., and Flatau, P.J. 1994, *Discrete-dipole approximation for scattering calculations*, J. Opt. Soc. Am. A, 11, 1491

Dyson, J.E., and Williams, D.A. 1997, The physics of the interstellar medium, (Bristol: IOP Publishing Ltd.)

Fabian, D., Jäger, C., Henning, Th., Dorschner, J., and Mutschke, H. 2000, *Steps toward interstellar silicate mineralogy V. Thermal evolution of amorphous magnesium silicates and silica*, A&A, 364, 282

Fabian, D., Posch, Th., Mutschke, H., Kerschbaum, F., and Dorschner, J. 2001a, *Infrared optical properties of spinels: A study of the carrier of the 13, 17, and 32 μm emission features observed in ISO-SWS spectra of oxygen-rich AGB stars*, A&A, 373, 1125

Fabian, D., Henning, T., Jäger, C., Mutschke, H., Dorschner, J., Wehrham, O. 2001b, *Steps toward interstellar silicate mineralogy VI. Dependence of crystalline olivine IR spectra on iron content and particle shape*, A&A, 378, 228

Feder, D., Russel, K.C., Lothe, B., and Pound, G.M. 1966, *Homogeneous nucleation and growth of droplets in vapours*, Advances in Physics, 15, 111

Gail, H.P., and Sedlmayr, E. 1999, *Mineral formation in stellar winds I. Condensation sequence of silicate and iron grains in stationary oxygen rich outflows*, A&A, 347, 594

Gehrz, R.D. 1989, in Interstellar Dust, eds. L.J. Allamandola & A.G.G.M. Tielens, pp. 445-453

Gervais, F. 1991, in Handbook of Optical Constants of Solids II, ed. E.D. Palik, (Boston: Academic Press Inc.)

Gould, R.J., and Salpeter, E.E. 1963, *The interstellar abundance of the hydrogen molecule. I. Basic processes*, ApJ, 138, 393

Graps, A.L. 2006, *Characterization of Jovian plasma-embedded dust particles*, Planetary and Space Science, 54, 911

Greenberg, J.M., and Hage, J.I. 1990, *From interstellar dust to comets: A unification of observational constraints*, ApJ, 361, 260

Greshake, A., Bischoff, A., and Putnis, A. 1996, *Pure CaO, MgO(Periclase),* TiO_2*(rutile), and* Al_2O_3*(corundum) in Ca, Al-rich inclusions from carbonaceous chondrites*, Lunar & Planetary Science, 27, 463

Greshake, A., Bischoff, A., and Putnis, A. 1998, *Transmission electron microscope study of compact Type A calcium-aluminum-rich inclusions from CV3 chondrites: Clues to their origin*, Meteoritics & Planetary Science, 33, 75

Gronholz, J., and Herres, W. 1985, Understanding FT-IR Data Processing, I&C Reprint, (Karlsruhe: Dr. Alfred Huething Publishers)

Grossman, L., and Larimer, J.W., 1974, *Early chemical history of the solar system*, Rev. of Geophys.& Space Phys., 12, 71

Habing, H.J., and Olofsson, H. 2004, Asymptotic Giant Branch Stars, (N.Y.: Springer-Verlag)

Hartmann, L. 1998, Accretion Processes in Star Formation, (Cambridge: Cambridge University Press)

Hecht, E. 1990, Optics, (Massachusetts: Addison-Wesley Publishing Company)

Henning, Th., and Mutschke, H. 2000, in Thermal Emission Spectroscopy and Analysis of Dust, Disks, and Regoliths, eds. M.L. Sitko, A.L. Sprague, and D.K. Lynch, 196, 253

Henning, Th., Mutschke, H., and Jäger, C. 2005, in Astrochemistry, eds. D.C. Lis, G.A. Blake, and E. Herbst, No.231

Herbig, G.H. 1960, *The spectra of Be- and Ae-type stars associated with nebulosity*, ApJS, 4, 337

Hinds, W.C. 1999, Aerosol Technology: Properties, Behavior, and Measurement of Airbone Particles, (N.Y.: John Wiley & Sons Inc.)

Hofmeister, A.M. 1997, *Infrared reflectance spectra of fayalite, and absorption data from assorted olivines, including pressure and isotope effects*, Phys. Chem. Minerals, 24, 535

Honda, M., Kataza, H., Okamato, Y.K., Miyata, T., Yamashita, T., Sako, S., Takubo, S., Onaka, T. 2003, *Detection of crystalline silicates around the T Tauri star HEN 3-600 A"*, ApJL, 585, L59

Honda, M., Kataza, H., Okamoto, Y.K., Miyata, T., Yamashita, T., et al. 2004, *Crystalline silicate feature of the Vega-like star HD145263*, ApJL, 610, L49

Horanyi, M., and Goertz, C.K. 1990, *Coagulation of dust particles in a plasma*, ApJ, 361, 155

Hougham, G., Cassidy, P.E., Johns, K., and Davidson, T. 1999, Fluoropolymers 2, (N.Y.: Kluwer Academic/Plenum Publishers)

Hu, J.Y., Thé, P.S., and de Winter, D. 1989, *Photometric and spectroscopic study of three candidate Herbig Ae/Be stars: HD37411, HD100546 and HD104237*, A&A, 208, 213

Iati, M.A., Cecchi-Pestellini, C., Williams, D.A., Borghese, F., Denti, P., Saija, R., and Aiello, S. 2001, *Porous interstellar grains*, Mon. Not. R. Astron. Soc., 322, 749

Ibach, H., and Lüth, H. 1991, Solid-State Physics: An Introduction to Theory and Experiment, (Berlin: Springer-Verlag)

Illingworth, V. 1994, The facts on file dictionary of astronomy, (N.Y.: Facts On File, Inc.)

Jäger, C., Mutschke, H., Begemann, B., Dorschner, J., and Henning, Th. 1994, *Steps toward interstellar silicate mineralogy I. Laboratory results of a silicate glass of mean cosmic composition*, A&A, 292, 641

Jäger, C., Molster, F.J., Dorschner, J., Henning, Th., Mutschke, H., and Waters, L.B.F.M. 1998, *Steps toward interstellar silicaate mineralogy IV. The crystalline revolution*, A&A, 339, 904

Jäger, C., Dorschner, J., Mutschke, H., Posch, Th., & Henning, Th. 2003, *Steps toward interstellar silicate mineralogy VII. Spectral properties and crystallization behaviour of magnesium silicates produced by the sol-gel method*, A&A, 408, 193

Jeong, K.S., Winters, J.M., and Sedlmayr, E. 1999, in IAU symposium Asymptotic Giant Branch Stars, eds. T. LeBerte, A. Lebre, & C. Waelkens, Nr.191, 233

Joy, A.H. 1945, *T Tauri variable stars*, ApJ, 102, 168

Klein, C., and Hurlbut, C.S.Jr. 1993, Manual of Mineralogy, (N.Y.: John Wiley & Sons, Inc.)

Koike, C., and Hasegawa, H. 1987, *Mid-infrared extinction coefficients of amorphous silicates*, Ap&SS, 134, 361

Koike, C., Shibai, H., and Tsuchiyama, A. 1993, *Extinction of olivine and pyroxene in the mid- and far- infrared*, Mon. Not. R. Astron. Soc., 204, 654

Koike, C., Kaito, C., Yamamoto, T., Shibai, H., Kimura, S., and Suto, H. 1995, *Extinction spectra of corundum in the wavelengths from UV to FIR*, Icarus, 114, 203

Koike, C., Chihara, H., Tsuchiyama, A., Suto, H., Sogawa, H., and Okuda, H. 2003, *Compositional dependence of infrared absorption spectra of crystalline silicate II. Natural and synthetic olivine*, A&A, 399, 1101

Kozasa, T., Blum, J., and Mukai, T. 1992, *Optical properties of dust aggregates I. Wavelength dependence*, A&A, 263, 423

Kozasa, T., and Sogawa, H. 1997, *Formation of Al_2O_3 grains and the 13 μm feature in circumstellar envelopes of oxygen-rich AGB stars*, Ap&SS, 255, 437

Kürster, M., Endl, M., Els, S., Hatzes, A.P., Cochran, W.D., Döbereiner, S., and Dennerl, K. 2000, *An extrasolar giant planet in an Earth-like orbit: Precise radial velocities of young star ι Horologii*, A&A, 353, L33

Lewis, R.I.Sr. 1993, Condensed Chemical Dictionary, (N.Y.: Van Nostrand Reinhold Company)

Li, A., and Greenberg, J.M. 1998, *From interstellar dust to comets: Infrared emission from comet Hale-Bopp (C/1995 O1)*, ApJ, 498, L83

Lide, D.R. 1990, CRC Handbook of Chemistry and Physics, (Boston: CRC Press Inc.)

Lide, D.R. 1991, CRC Handbook of Chemistry and Physics, (Boston: CRC Press Inc.)

Linsebigler, A.L., Lu, G., and Yates, J.T.Jr. 1995, *Photocatalysis on TiO_2 surfaces: Principles, mechanisms, and selected results*, Chem. Rev., 95, 735

Mackowski, D.W., and Mishchenko, M.I. 1996, *Calculation of the T matrix and the scattering matrix for ensembles of spheres*, J. Opt. Soc. Am. A., 13, 2266

Malfait, K., Waelkens, C., Waters, L.B.F.M., Vandenbussche, B., Huygen, E., & de Graauw, M.S. 1998, *The spectrum of the young star HD100546 observed with Infrared Space Observatory*, ApJ, 332, L25

Mannings, V., and Barlow, M.J. 1998, *Candidate main-sequence stars with debris disks: A new sample of Vega-like sources*, ApJ, 497, 330

Marcy, G.W., and Butler, R.P. 1998, *Detection of extrasolar giant planets*, ARA&A., 36, 57

Marcy, G.W., Butler, R.P., Vogt, S.S., Fischer, D., and Liu, M.C. 1999, *Two New Candidate Planets in Eccentric Orbits*, A&A, 520, 239

Mathis, J.S. 1990, *Interstellar dust and extinction*, ARA&A, 28, 37

Mayor, M., and Queloz, D. 1995, *A Jupiter-mass companion to a solar-type star*, Nature, 378, 355

Meeus, G., Sterzik, M., Bouwman, J., and Natta, A. 2003, *Mid-IR spectroscopy of T Tauri stars in Chamealeon I: Evience for processed dust at the ealiest stages*, A&A, 409, L25

Meeus, G., Waters, L.B.F.M., Bouwman, J., van den Ancker, M.E., Waelkens, C., Malfait, K. 2001, *ISO spectroscopy of circumstellar dust in 14 Herbig Ae/Be systems: Towards an understanding of dust processing*, A&A, 365, 476

Meyer, M.R., Backman, D., Mamajek, E.E., et al. 2001, *The post T Tauri binary HD113766: Discovery of an inner debris disk system?*, A&AS, 199, 7608

Mie, G. 1908, *Beiträge zur Optik trüber Medien speziell kolloidaler Metallösungen*, Ann. Phys., 25, 377

Min, M., Hovenier, J.W., and de Koter, A. 2003, *Shape effects in scattering and absorption by randomly oriented particles small compared to the wavelength*, A&A, 404, 35

Min, M., Hovenier, J.W., de Koter, A., Waters, L.B.F.M., and Dominik, C. 2005, *The composition and size distribution of the dust in the coma of comet Hale-Bopp*, Icarus, 179, 158

Mishchenko, M.I. 1990, Ap&SS, 164, 1

Mo, S.-D., and Ching, W.Y. 1995, *Electronic and optical properties of three phases of titanium dioxide: Rutile, anatase, and brookite*, Phy. Rev. B, 51, 13023

Molster, F.J., Waters, L.B.F.M., Tielens, A.G.G.M., 2002, *Crystalline silicate dust around evolved stars III. A correlations study of crystalline silicate features*, A&A, 382, 241

Molster, F.J., and Waters, L.B.F.M. 2003, in Astromineralogy, ed. Th. Henning, pp.121-170, (Berlin: Springer)

Morrison, D., and Wolff, S.C. 1990, Frontiers of Astronomy, (Philadelphia: Saunders College Publishing)

Mukai, T. 1982, in Comets and Interstellar Matter, ed. S. Yabushita, 111, (Tokyo: Chijinshokan)

Muraishi, H. 2004, Basic Solid State Chemistry for Inorganic Materials (Tokyo: Sankyo Shuppan Inc.)

Nittler, L.R., Alexander, C.M.O'D., Stadermann, F.J., Zinner, E.K. 2005, in 36th Annual Lunar and Planetary Science Conference, Abst. No.2200

Ohnaka, K. 2006, in EuroSummer School "Observation and data reduction with the Very Large Telescope Interferometer", ppt. source, Goutelas, France

Okamoto, H., Mukai, T., and Kozasa, T. 1994, *The 10 μm feature of aggregates in comets*, Planet. Space Sci., 42, 643

Okamoto, Y.K., Kataza, H., Honda, M., Yamashita, T., Onaka, T., Watanabe, J., Miyata, T., Sako, S., Fujiyoshi, T., and Sakon, I. 2004, *An early extrasolar planetary system revealed by planetesimal belts in β-Pictoris*, Nature, 431, 660

Onaka, T., de Jong, T., and Willems, F.J. 1989, *A study of M Mira variables based on IRAS LRS observations. I- Dust formation in the circumstellar shell*, A&A, 218, 169

Ossenkopf, V. 1991, *Effective medium theories for cosmic dust grains*, A&A, 251, 210

Ossenkopf, V., Henning, Th., Mathis, J.S. 1992, A&A, 261, 567

Oudmaijer, R.D., van der Veen, W.E.C.J., Waters, L.B.F.M., Trams, N.R., Waelkens, C., and Engelsman, E. 1992, *SAO stars with infrared excess in the IRAS point source catalog*, Astron. Astrophys.Suppl.Ser., 96, 625

Palas GmbH 2002, Operating Manual Solid Particle Disperser, (Karlsruhe: Palas GmbH)

Papoular, R., Cauchetier, M., Begin, S., and LeCaer, G. 1998, *Silicon carbide and the 11.3 μm feature*, A&A, 329, 1035

Pellant, C. 1992, Rocks and Minerals, (N.Y.: DK Publishing Inc.)

Phillip, H.R. 1985, in Handbook of Optical Constants of Solids, ed. E.D. Palik, (Boston: Academic Press Inc.)

Posch, Th., Kerschbaum, F., Mutschke, H., Fabian, D., Dorschner, J., and Hron, J. 1999, *On the origin of the 13 μm feature: A study of ISO-SWS spectra of oxygen-rich AGB stars*, A&A, 352, 609

Posch, Th., Kerschbaum, F., Mutschke, H., Dorschner, J., and Jäger, C. 2002, *On the origin of the 19.5 μm feature: Identifying circumstellar Mg-Fe-oxides*, A&A, 393, L7

Purcell, E.M., and Pennypacker, C.R. 1973, *Scattering and absorption of light by nonspherical dielectric grains*, ApJ, 186, 705

Querry, M.R. 1985, Optical Constants, (Maryland: Chemical Research Development Center, U.S. Army Armament, Munitions & Chemical Command Aberdeen Proving)

Reade Advanced Materials 1997, http://www.reade.com/Products/Minerals_and_Ores/anatase.html

Rietmeijer, F.J.M., Nuth, J.A., and Mackinnon, I.D.R. 1986, *Analytical electron microscopy of Mg-SiO smokes - A comparison with infrared and XRD studies*, Icarus, 66, 211

Rohrer, G.S. 2001, Structure and bonding in crystalline materials, (N.Y.: Cambridge University Press)

Röseler, A. 1990, Infrared Spectroscopic Ellipsometry, (Berlin: Akademie-Berlag)

Rudolph, S. 2004, http://www.a-m.de/englisch/lexikon/olivin.htm, Büro für angewandte Mineralogie

Saito, H., Imai, K., Ooishi, M., Sawada, T., and Suzuki, K. 2004, Nyuumon Kotaibussei - Kiso kara Device made, (Tokyo: Kyoritsu Shuppan Inc.)

Saniger, J.M. 1995, *Al-O infrared vibrational frequencies of γ-alumina*, Materials Letters, 22, 109

Schmocker, U., Boesch, H.R., and Waldner, F. 1972, *A direct determination of cation disorder in $MgAl_2O_4$ spinel by ESR*, Phys. Lett., 40A, 237

Schegerer, A., Wolf, S., Voshchinnikov, N.V., Przygodda, F., and Kessler-Silacci, J.E. 2006, *Analysis of the dust evolution in the circumstellar disks of T Tauri stars*, A&A, 456, 535

Schubert, M. 2004 Infrared Elipsometry on Semiconductor Layer Structures: Phonons, Plasmons, and Polaritons, (Berlin: Springer-Verlag)

Schütz, O., Meeus, G., & Sterzik, M.F. 2005, *Mid-IR observations of circumstellar disks I. Pre-main sequence objects*, A&A, 431, 175

Sedlmayr, E. 1994, in Molecules in the Stellar Environment, ed. U.G. Jorgensen, 428, 163, (Berlin: Springer-Verlag)

Seeds, M.A. 1995, Horizons, (Belmont: Wadsworth Publishing Company)

Servoin, J.L., & Piriou, B. 1973, *Infrared reflectivity and Raman scattering of Mg_2SiO_4 single crystals*, Phys. Status Solidi B, 55, 677

Sharp, C.M., and Huebner, W.F. 1990, *Molecular equilibrium with condensation*, ApJS, 72, 417

Simpson, I.C., Simpson, S., and Williams, I.P. 1979, *Thermal coagulation of charged grains in dense clouds*, Ap&SS, 61, 65

Smith, R.C. 1995, Observational Astrophysics, (N.Y.: Combridge University Press)

Speck, A.K. 1998, PhD Thesis, University College, England

Speck, A.K., Hofmeister, A.M., and Barlow, M.J. 2000, in Thermal Emission Spectroscopy and Analysis of Dust, Disks, and Regoliths, eds. M.L. Sitko, A.L. Sprague, and D.K. Lynch, 196, 281

Spitzer, L.Jr. 1982, Searching Between the Stars, (New Haven: Yale University Press)

Streitz, F.H., and Mintmire, J.W. 1999, *Energetics of aluminum vacancies in gamma alumina*, Phy. Rev. B, 60, 773

Suito, K. 1972, *Phase transformations of pure Mg_2SiO_4 into a spinel structure under high pressures and temperatures*, J. of Physics of the Earth, 20, 225

Tamanai, A., Mutschke, H., Blum, J., Neuhäuser, R. 2006, J. Quant. Spectrosc. Radiat. Transfer, 100, 373

Tamanai, A., Mutschke, H, Blum, J., Meeus, G. 2006, ApJL, 648, L147

Tatum, J.B. 2006, Stellar Atmosphere, http:astrowww.phy.uvic.ca/∼tatum, Department of Physics & Astronomy at University of Victoria, Canada

Thomas, M.E. 1991, in Handbook of Optical Constants of Solids II, ed. E.D. Palik, (Boston: Academic Press Inc.)

Throop, H.B., Bally, J., Esposito, L.W., and McCaughrean, M. 2001, *Evidence for dust grain growth in young circumstellar disks*, Science, 292, 1686

Tielens, A.G.G.M. 1990, in From Miras to Planetary Nebulae, eds. M.E. Mennessier and A. Omont, 186, (Gif-sur-Yvette: Editions Frontiéres)

Tropf, W.J., and Thomas, M.E. 1991, in Handbook of Optical Constants of Solids II, ed. E.D. Palik, (Boston: Academic Press Inc.)

Tsai, C-J., Pui, D.Y.H., and Liu, B.Y.H. 1991, *Elastic flattening and particle adhesion*, Aerosol Sci. Tech., 15, 239

van Boekel, R., Waters, L.B.F.M., Dominik, C., Bouwman, J., de Koter, A., Dullemond, C.P., and Paresce, F. 2003, *Grain growth in the inner regions of Herbig Ae/Be star disks*, A&A, 400, L21

van Boekel, R., Min, M., Leinert, Ch., Waters, L.B.F.M., Richichi, A., et al. 2004, *The building blocks of planets within the 'terrestrial' region of protoplanetary disks*, Nature, 432, 479

van Boekel, R., Min, M., Waters, L.B.F.M., de Koter, A., Dominik, C., van den Ancker, M.E., and Bouwman, J. 2005, *A 10 μm spectroscopic survery of Herbig Ae star disks: Grain growth and crystallization*, A&A, 437, 189

van den Ancker, M.E., Thé, P.S., Tjin A Djie, H.R.E., Catata, C., de Winter, D., Blondel, P.F.C., and Waters, L.B.F.M. 1997, *HIPPARCOS data on Herbig Ae/Be stars: an evolutionary scenario*, A&A, 324, L33

van den Ancker, M.E., de Winter, D., and Tjin A Djie, H.R.E. 1998, *HIPPARCOS photometry of Herbig Ae/Be stars*, A&A, 330, 145

van den Ancker, M.E., Bouwman, J. 2005, A&A, 437, 189

Vander Vorst, A., Rosen, A., and Kotsuka, Y. 2006, RF/Microwave Interaction with Biological Tissues, (Hoboken: John Wiley & Sons)

Walker, H.J., and Wolstencroft, R.D. 1988, *Cool circumstellar matter around nearby main-sequence stars*, PASP, 100, 1509

Waterman, P.C. 1971, *Symmetry, unitarity, and geometry in electromagnetic scattering*, Phys. Rev., D3, 825

Waters, L.B.F.M., Molster, F.J., de Jong, T., Beintema, D.A., Waelkens, C., et al. 1996, *Mineralogy of oxygen-rich dust shells*, A&A, 315, L361

Waters, L.B.F.M., and Waelkens, C. 1998, *Herbig Ae/Be stars*, ARA&A, 36, 233

Weidenschilling, S.J., and Cuzzi, J.N. 1993, in Protostars and Planets III, eds. E.H. Levy & J.I. Lunine, pp.1031-1060 (University of Arizona Press)

Weissman, P.R. 1984, *The Vega Particulate Shell: Comets or Asteroids?*, Science, 224, 987

Wenk, H.-R., and Bulakh, A. 2004, Minerals: Their Constitution and Origin, (N.Y.: Cambridge University Press)

Whipple, F.L. 1950, *A comet model. I. The acceleration of comet encke*, ApJ, 111, 375

Whittet, D.C.B. 1992, Dust in Galactic Environment, (Bristol: IOP Publishing)

Won, D.-J., Wang, C.-H., Jang, H.-K, Choi, D.-J. 2001, Applied Physics A Materials Science & Processing, 73, 595

Zallen, R. 2004, The Physics of Amorphous Solids, (Weinheim: Wiley-VCH)
Zuckerman, B., and Song, I. 2004, *Disty debris disks as signposts of planets: Implications for Spitzer Space Telescope*, ApJ, 603, 738

Appendix A

Equilibrium condensates (P=10^{-3} atm) by Grossman 1974.

Phase	Chemical Formula	Condensation Temperature [K]	Disappearance Temperature [K]
Corundum	Al_2O_3	1758	1513
Perovskite	$CaTiO_3$	1647	1393
Melilite	$Ca_2Al_2SiO_7$-$Ca_2MgSi_2O_7$	1625	1450
Spinel	$MgAl_2O_4$	1513	1362
Metallic Iron	(Fe, Ni)	1473	
Diopside	$CaMgSi_2O_6$	1450	
Forsterite	Mg_2SiO_4	1444	
	Ti_3O_5	1393	1125
Anorthite	$CaAl_2Si_2O_8$	1362	
Enstatite	$MgSiO_3$	1349	
Eskolaite	Cr_2O_3	1294	
Metallic Cobalt	Co	1274	
Alabandite	MnS	1139	
Rutile	TiO_2	1125	
Alkali Feldspar	(Na, K)$AlSi_3O_8$	≈1000	
Troilite	FeS	700	
Magnetite	Fe_3O_4	405	
Ice	H_2O	≤200	

Condensation temperature (P=4.935×10^{-4} atm) by Sharp 1990.

Phase	Chemical Formula	Appearance Temperature [K]	Disappearance Temperature [K]
Zirconium Oxide	ZrO_2	1807	
Corundum	Al_2O_3	1716	1496
Perovskite	$CaTiO_3$	1639	1400
Melilite	$Ca_2Al_2SiO_7$-$Ca_2MgSi_2O_7$	1576	1407
Spinel	$MgAl_2O_4$	1497	
Iron	Fe	1421	
Forsterite	Mg_2SiO_4	1411	
Diopside	$CaMgSi_2O_6$	1411	
Vanadium oxide	VO	1404	1187
	Ti_4O_3	1401	1092
Nickel	Ni	1357	
Enstatite	$MgSiO_3$	1336	
Eskolaite	Cr_2O_3	1253	
Vanadium trioxide	V_2O_3	1187	
Albandite	MnS	1119	
	$MgTi_2O_5$	1092	

Appendix B

All the abbreviation and acronym terms used in this dissertation.

Abbreviation	Whole phrase
AGB stars	asymptotic giant branch stars
BCCA	Ballistic Cluster-Cluster Aggregates
BPCA	Ballistic Particle-Cluster Aggregates
CDE	continuous distribution of ellipsoids
C_{ext}	extinction cross-section
CTTSs	classical T-Tauri stars
DDA	discrete dipole approximation
DHS model	distribution of hollow spheres model
EDX	electron dispersive X-ray
EMT	effective medium theory
FTIR	Fourier Transformation Infrared Spectroscopy
FWHM	full width at half maximum
HAEBE stars	Herbig Ae/Be stars
HR diagram	Hertzstrung-Russell diagram
IR radation	infrared radiation
ISM	interstellar mediu
ISO	Infrared Space Observatory
KBr pellet	potassium bromide pellet

Abbreviation	Whole phrase
LA phonon	acoustic longitudinal phonon
LO phonon	optical longitudinal phonon
Q_{ext}	extinction efficiency
SAXS	small angle X-ray scattering
sed.	sedimentation
SEM	scanning electron microscope
TA phonon	acoustic transverse phonon
TEM	transmission electron microscope
TEOS	tetraethyl orthosilicate
TO phonon	optical transverse phonon
TTSs	T-Tauri stars
UV	ultraviolet
WTTSs	weak-emission pre-main-sequence stars (weak-emission T-Tauri stars)
YSOs	young stellar objects
β-Pic	β- Pictoris

Acknowledgment

I thank Prof. Dr. Ralph Neuhäuser for your perspective and supportive ideas to bring me out here in Jena and Prof. Dr. Krivov Alexander and Prof. Dr. Werner Pfau for your supports and cooperation.

I am grateful to all Astrophysics Lab. group members in Jena, Dr. Harald Mutschke, Dr. Cornelia Jäger, Frau Gabriele Born, Herr Walter Teuschel, Dr. Isable Llamas Jansa, and Dr. Johann Dorschner for your helpful advices, insightful comments, and encouragement. I deeply appreciate from the bottom of my heart. Without your help and supports, I could not come up to here. I greatly appreciate Prof. Dr. Jügen Blum for your insightful comments and ideas for our research project.

I wish to thank Prof. Dr. Thomas Henning, Prof. Dr. Erwin Sedlmayr, Prof. Dr. Hans Zinnecker, Prof. Dr. Mark J. McCaughrean, Prof. Dr. Artie P. Hatzes, Prof. Dr. Sergio Fonti, Prof. Dr. Friedrich Huisken, and Prof. Dr. Klaus Hide for giving me a lot of opportunities to explore the astrophysical world and related fields. I have been spurred on by your advising from different angles and view points.

I am thankful to Prof. Dr. David R. Alexander and Prof. Dr. Jason W. Ferguson for your advising and precious words of encouragement. I express my gratitude for Dr. Marc Hempel, Dr. Gwendolyn Meeus, Dr. Matthias Ammler, Dr. Christopher Boerg, Dr. Eike Guenther, Dr. Günther Wuchterl, Dr. Rainer Schräpler, Dr. Nathalie Boudet. I really had a great time not only in our research, but also in personal life.

I give my special thanks for Dr. Jens-Peter Kaufmann, Dr. Kyung Sook Joeng, Dr. Jan Martin Winters, Dr. Thibaut LeBertre, Dr. Thomas Posch, and Dr. Anja C. Andersen. Because you all gave me a great opportunities, I could surmount numerous obstacles. I deeply appreciate your thoughtfulness and understanding.

I wish to thank all of AIU members (current and former), Ana Bedalov, Jan Forbrich, Torsten Löhne, Bettina Posselt, Andreas Seifahrt, Helge Rehwald, Tobias Schmidt, Sebastian Krause, Manuela Wiese, Martina Queck, Gael Rouillé, Markus Mugrauer, Dr. Dimitry Semenov, Dr. Katharina Schreyer, Dr. Torsten Poppe, Dr. Oleksandr Sokhorukov, who have shared a great moment in Jena. I thank Frau Monika Müller and Herr Jürgen Weiprecht for your technical supports and assistances.

I am thankful to Prof. Dr. Chiyoe Koike for her advices, sharing a new sample for my experiment, and giving me an opportunity to introduce my project in Japan. As my first Japanese SENPAI in this astronomical field, I express my gratitude for Dr. Kengo Tachihara who has always supported me in Jena and from Japan.

I am very fortunate to have a lot of friends in a world who always cheer me up. Even if we have a long distance and cannot see each other often, I believe that we have understood each other almost as if we could read each other's minds.

Lastly, I am thankful to my family who has allowed and understood my will, action, decision, and selfishness.

My project has supported by Deutsche Forschungsgemeinschaft (DFG) under the grant MU 1164/5-3-4.

Ehrenwörtliche Erklärung

Hiermit erkläre ich, dass ich die vorliegende Dissertation selbst angefertigt habe und alle von mir verwendeten Hilfsmittel, persönlichen Mitteilungen und Quellen angegeben habe. Aber weil Deutsch nicht meine Muttersprache ist, halfen mir meine Kollegen, Dr. H. Mutschke, Dr. M. Hempel, und Dr. Ch. Boerg bei der Übersetzung aus dem Englischen ins Deutsche (Zusammenfassung, Erklärung, und Thesen).

Diese Arbeit wurde bisher weder im In- noch im Ausland in gleicher oder ähnlicher Form einer Prüfungsbehörde vorgelegt.

Jena, May 21, 2007

Curriculum Vitae

Personal Information

Name	Akemi Tamanai
Date of Birth	26. January 1968
Place of Birth	Hitachi-City, Japan
Parents	Shinichi Tamanai Kazuko Tamanai
Nationality	Japan

Educational Information

Apr. 1974 – March. 1980	Elementary school Kuji-Shougakkou in Hitachi, Japan
Apr. 1980 – March. 1983	Junior high school Kuji-Chougakkou in Hitachi, Japan
Apr. 1983 – March. 1986	High school Hitachikita-Koutougakkou in Hitachi, Japan
1987	Medical treatment
Aug. 1988 – Dec. 1989	Intensive English Language Center, Wichita State University, Kansas, USA
Jan. 1990 – May 1995	Bachelor of Science, Physics, Wichita State University, Kansas, USA
Aug. 1995 – Dec. 1998	Master of Science, Physics, Wichita State University, Kansas, USA Titel of master's thesis: *Low Temperature Opacity*
Apr. 2001 – Sep. 2003	PhD study, Astrophysics, Zentrum fr Astronomie & Astrophysik, TU Berlin
Oct. 2003 – May. 2007	PhD study, Astrophysics, Astrophysical Institute and University Observatory, Friedrich-Schiller-University Jena Titel of PhD dissertation: *Experimental Mid-Infrared Spectroscopic Measurements of Agglomerate Dust Grains in Aerosol*

Positions

1991	Receptionist at Hesket Center, Wichita State University
1993	Paper Grader at Mathematics Department, Wichita State University, Kansas, USA
1994 – 1995	Paper Grader at Physics Department, Wichita State University, Kansas, USA
1996	Graduate Assistant at Physics Department, Wichita State University, Kansas, USA
1997 – 2000	Graduate Research Assistant at Physics Department, Wichita State University, Kansas, USA (NASA grant NCC5-168)
2001 – 2003	PhD study in the group of Prof. Sedlmayr Zentrum fr Astronomie & Astrophysik, TU Berlin PhD study in the group of Prof. Zinneker & Prof. McCaughrean Astrophysikalisches Institut Potsdam (Feb.-Aug. 2003)
2003 – 2006	PhD study in the Lab. group of Dr. Mutschke (supervised by Prof. Neuhäuser) Astrophysical Institute and University Observatory, FSU Jena (DFG MU1164/5-3-4)
Jan. 2007 –	Max-Planck-Institute for Astronomy, Heidelberg in the group of Prof. Henning

Jena, May 21, 2007

Lasting regrets result from the things
we fail to do, not those we do.

人間は、行動した後悔より、
行動しなかった後悔の方が深く残る。

by Prof. Thomas Dashiff Gilovich
Psychologist, Cornell University